Feedback Models in Biological Physics

by

Alexander D. Golden

A dissertation submitted in partial fulfillment
of the requirements for the degree of
Doctor of Philosophy
(Applied Physics)
in the University of Michigan
2018

Doctoral Committee:

Associate Professor David K. Lubensky, Chair
Professor Charles Doering
Professor Daniel B. Forger
Assistant Professor Kevin Wood
Assistant Professor Qiong Yang

goldalex@umich.edu
ORCID iD: 0000-0002-0136-4223

Acknowledgements

My work here and the path that led me to it has been supported in a great many different ways and I would be remiss not to acknowledge these numerous sources. I would first like to thank my family. Both my father and his father were in some way involved in science. My grandfather worked on radar and eventually worked with NASA at the Goddard Space Flight Center. My father is a biomedical engineer working at the Naval Research Laboratory. I can fondly remember being given math and science lessons when I was still very little, either about the orderly parabolic trajectory of a projectile or the zoo of totally alien life I would find by putting water from a local pond under the microscope. The interest in nature manifested itself as an apparently encyclopedic knowledge of fish, bird and dinosaur species which I regrettably did not retain through adolescence. It was certainly through this influence that I ended up studying electrical engineering in college, eventually adding a major in mathematics and a minor in physics. I also gained a great deal through the influence of my mother, who, as a teacher herself, sent me to a Montessouri school for the majority of my early education. With the benefit of hindsight and hearing about the experiences of my peers I have come to the conclusion that this environment was very helpful for developing both practical skills as well as an intuitive, material understanding of abstract concepts in mathematics. Additionally, the time I spent in Germany visiting friends and my mother's family, and being exposed to so many new cultures and languages has done a great deal for my personal growth and development into someone capable of understanding concepts and problems from many different perspectives.

I would also like to thank the various academic mentors and other supporters I have had through my education. First Dave Adams, my history teacher in high school, from whom I learned that to study something was really to understand one's surroundings and how they were constituted. Then I would like to thank my various mentors at the University of Maryland, College Park. I took a circuitous path through the sciences, first working on very applied optics with Prof. Chris Davis, who was my first academic research mentor.

Afterwards I worked with Dr. John Rodgers who gave me excellent opportunities to work on problems of plasma physics, as well as Prof. Krishnaprasad, who gave me the opportunity to glimpse the mathematical structures involved in control systems. I am also grateful for the unorthodox treatments of classical mechanics that I recieved in the courses of Profs. Ted Jacobson and Stuart Antman. Prof. Jacobson's course on introductory classical mechanics was full of uncommon insight into how physics was different from engineering and mathematics, even though a great deal of that had to be discovered in hindsight. Similarly, when I was doing independent study work with Prof. Antman I was very pleased to be learning the finer details of the formal aspects of classical mechanics for their own sake, but I did not foresee how fundamental the ideas he was introducing about classical mechanics would be to my work in graduate school. I would also like to thank the various academic advisors I have had, especially Prof. Tom Cohen, who suggested that, as someone with an engineering background, I skip the physics GRE and instead apply to programs that didn't require it, suggesting that I would likely be able to do physics work regardless. This brings me to the Applied Physics program here at the University of Michigan. Prof. Kurdak as well as Lauren and Cyndi have been an inspiring source of support and have made my success here possible.

I began as a graduate student in the Lubensky group with a background in engineering and mathematics. This gave me an understanding of the formal properties of mathematical models and the ability to use them productively in the cases where the models were known to be valid. During my time studying theoretical biophysics I have had to learn a great deal more about the use and utility of models. This has come in part from preparing for the applied physics qualifying exam. To this day I still find myself coming across small physics problems in my daily life, and reasoning my way through them is a very valuable way of developing my own understanding. Of course, a lion's share of the credit for my development as a physicist as opposed to a mathematician or engineer goes to my advisor, Prof. David Lubensky. I can confidently say that I have gained almost all of my understanding of physics directly from my work with him. This began with me taking his class in my first year through spending the rest of my time in the group learning how to evaluate the problems I was studying and how to interpret experimental and theoretical results, both my own and those that I would compare to.

I also need to thank all of my friends, colleages, and comrades who have been there for me throughout my life. My friends have been a constant source of support and have given me the opportunity to live a larger life, whether having wonderful discussions (academic or

not) or just reminding me that the grass is not always greener on the industry side. Finally I need to thank my fiancée Angela, with whom I have shared the past 8 wonderful years and hope to share many more as we make our next move to Boston.

Table of Contents

List of Figures

List of Appendices

Abstract

Feedback models play a crucial role in biological physics. They underlie many of the phenomena that are essential for life, from regularity and homeostasis to growth and rhythms. Using these models to analyze biological systems is more involved than simply solving the equations. In order for the models to be valuable tools for a research community it is necessary to connect these formal models to experimental observations, and to use experimental observations to distinguish between different types of model. How the details of the structure of a model relate to the experimental observables it predicts for the biophysical system can sometimes be obscure, especially for numerical models. This thesis presents two studies in which the feedback structures of models for biological systems are analyzed. In each case, differences in the feedback structure are shown to predict experimentally observable consequences. In a simple post-translational protein oscillator it is possible to determine the sign of the feedback present in the biophysical system by comparing model oscillators with opposing signs for the dominant feedback. When the feedback strength is modulated, the positive and negative feedback models predict that the period of the oscillation changes in opposing directions. We show that this is a generic property of the distinct families of oscillator models by considering extensions that have been proposed for each and demonstrating that the results hold. We then compare different models of tissue growth in the *Drosophila* wing disk epithelium based on experimental observables such as precision of the final size, the uniformity of growth, and the presence of spatiotemporal patterns of apoptosis. Using an analytic framework we connect these observables to the feedback structures of different model families, defined by characteristics such as which quantities participate in the feedback and whether or not growth is allowed at all points in the tissue. We show that mechanical feedback models that disallow growth over macroscopic sections of the tissue cannot predict a unique final size.

Chapter 1

Introduction

Models in biology can serve a variety of different purposes. Some are highly synthetic, attempting to provide insight into the net effect of many different, interacting components such as entire cells or large signalling networks. Some work to provide detailed, quantitatively precise descriptions of single functional units such as molecular motors or ion channels. Others work in an intermediate regime, not necessarily aiming for quantitative precision or comprehensive enumeration but attempting to demonstrate "generic" or "simple" principles underlying qualitative phenomena. This work will focus on the last of these.

Simple, phenomenological models have a long history in the study of living systems. A classic example is *On Growth and Form* [176], notable for being an early example of quantitative modeling and in particular explaining biological phenomena with concepts from physics such as scaling arguments for how metabolism changes with size and mechanical constraints on growth. The well known Michaelis-Menten differential equation for the rate of enzymatic reactions [113] is another example from the same period. Other notable models of biological systems from that era were Schrödinger's hypothesis that genetic information is stored in an "aperiodic crystal" [163] and Turing's conjecture of reaction-diffusion processes as underlying developmental pattering [179]. These are all notable for being proposed before much was known about the fundamental constituents of biological systems, such as the central role of DNA in inheritance and protein encoding or the role of proteins in genetic regulation.

The subsequent revolution in molecular biology revealed a vast regulatory structure underpinning the fundamental processes of life, with cycles and feedback present at many levels. Thus as the physical foundations of life were elucidated, it simultaneously became clear that there was important information contained in the structure of how all of the constitutents

interacted. While this information is in principle contained in the physical structure of the constituents (in terms of binding rates, protein structures, etc), arriving at useful results from first principles is often prohibitively difficult. Because of this, simple phenomenological models have become common tools for interpreting the dynamics of biological processes, especially for feedback systems. They have been successful in explaining phenomena as diverse as bacterial chemotaxis [9], epithelial-mesenchymal transitions [104], and somatogenesis [98]. The development of models such as these is particularly valuable when general principles or families of models can be generalized to other situations, for example the identification of integral feedback control as a mechanism for the "perfect adaptation" in bacterial chemotaxis [199].

Feedback models form an important subclass of these models. Not only do they provide an intuitive framework for understanding dynamics (since they can often be represented by simple diagrams), but they play important roles in generating many types of common phenomena. Negative feedback fundamentally underlies the concept of homeostasis, dynamically reacting to changes in the environment in order to ensure that biologically necessary processes continue at appropriate rates [181, 199]. It is also necessary for the generation of oscillations. Positive feedback serves to produce dynamical bistability, which is necessary for switch-like behavior and hysteresis [181].

Although phenomenological models of this sort have been powerful tools for comprehending biological processes in cases where first principles arguments are not practical, there can be some ambiguity in their structure. It is well known in control system engineering that the precise details of a control system can have important qualitative impacts on how the system functions, for example in simple PID controllers it is possible to control a very wide range of responses including ringing, steady-state error, and response time, all by tuning three parameters. This is no less true in biology. Even when the underlying biochemistry is known, there is not a unique mapping from these building blocks to a single observed macroscopic phenotype. In order to understand the function of the regulatory or feedback structure of a biochemical system it is necessary to understand how different choices for the structure (and therefore the dynamics) influence the accessible experimental observables.

In the following two sections we will outline two biological systems where we have made experimental predictions that distinguish between qualitatively different feedback structures. First we introduce the study of biochemical oscillations and how different oscillators are classified, and describe the cyanobacterial system which we focus on. We demonstrate that by comparing models with different feedback structures it is possible to re-interpret existing

data to determine the feedback structure of the *in vitro* system. We then introduce the problem of growth control, and describe how different mechanisms of mechanical feedback could be distinguished experimentally.

1.1 Biological oscillations and rhythms

Oscillations are ubiquitous in biological systems. They were first introduced in formal models in population dynamics and neuroscience, where the Lotka-Volterra equations [190] and the Hodgkin-Huxley model [75] are both still commonly used. Since the mid-20th century there have been many more examples of oscillatory rhythms underlying key biological processes. These include metabolic processes as such glycolysis [74] and cAMP production [57], as well as various oscillations in chloroplasts and mitochondira [73]. More recently oscillations have been shown to play important roles in regulating organismal development, for example in somitogenesis [98, 121] and in *Xenopus* egg development [134, 147].

This great diversity of roles played by biological oscillators reflects a common utility for a regular signal of some kind. Often these oscillations can be understood as serving to synchronize behaviors of many individual components in time. The mechanisms by which these collective systems come together to produce oscillations play an important role in determining the net function of the oscillator and how it interacts with its environment, and these mechanisms can be classified in various different ways. The fundamental elements of these oscillators are often discovered by identifying the molecular components of the oscillator and determining how they interact, resulting in a model described in terms of constituent molecular components. This approach, although it is fundamental for understanding the oscillation, is often overly specific. Beyond identifying homologous protein systems in other organisms this method alone does not provide a meaningful way to compare the operation of any two oscillators. In fact, understanding the base constituents of a biological oscillator can leave ambiguity about whether two models of the same oscillator are somehow qualitatively different. Studying system-level characteristics of the oscillator, however, can provide criteria which allow direct comparison and classification of different oscillator models.

A vast collection of phenomenlogicial and systems level tools have been developed to understand the qualitative character of the oscillations that are found in biological systems. These range from the mathematical, such as the distinction between limit-cycle oscillations and Hamiltonian oscillations (which has implications for the relationship between the amplitude and frequency of the oscillation, among other things), to more qualitative or heuristic

tools such as identifying structures in the "circuit diagrams" that are common in analyzing biochemical regulatory systems. From these methods some sets of criteria have arisen decribing fundamental qualitative charactersitics that are necessary components of an oscillator model.

It is commonly accepted that in order for a chemical system to oscillate it requires negative feedback, a mechanism for generating a time delay, and some kind of nonlinearity [135]. Negative feedback is identified as what causes the system to return to some initial point, necessary for periodic behavior. A sufficient time delay is required to prevent the system from attracting to a simple steady state. The nonlinearity then functions to make the steady state unstable, creating the limit cycle that attracts the oscillator.

Each of these components can take a number of forms. For example, the time delay could come from a large number of intermediate states, each of which requires a certain amount of time to pass through [60,135]. Alternately, the delay could arise from positive feedback [135]. This can often be understood in terms of positive feedback introducing hysteresis to the dynamics, causing the system to "overshoot" what would otherwise be the steady state. Although each of these mechanisms in some sense provides the necessary "time delay", it is still possible to distinguish the operation of these types of feedback. For example, it has been suggested on formal grounds that strong positive feedback can make oscillations easier to achieve [51]. With this understanding in hand we can return to the biological systems with an eye for systems-level phenomena. Since biological systems can be close to optimimal for some regimes [**?**], finding clear examples of positive or negative feedback oscillators in nature indicates that these feedback structures could serve some specific function. In turn, understanding more about the implications of these feedback structures can give a greater insight into the function and operation of the great diversity of oscillations found in nature.

To understand these feedback structures in this thesis we study one of the simplest and most experimentally tractable chemical oscillators found in nature: the circadian oscillator of the cyanobacterium *S. elongatus*. Circadian oscillators are the internal clocks which organisms use to predict day/night cycles and are some of the earliest free-running biological rhythms to be identified. J. B. D. de Mairan demonstrated in 1729 that the Mimosa plant would continue opening and closing its leaves even if it were placed in a dark box without any sunlight to set the rhythm [202]. Circadian oscillators have become defined by several properties: a 24 hour period even in the absence of exposure to light (defining the day/night cycle), temperature compensation so that the 24 hour period is stable to reasonable changes in temperature, and entrainment to light from the sun (for example, allowing recovery from

jet lag) [16].

Circadian clocks have been identified in many different organisms, ranging from bacteria to plants to insects and vertebrates. In insects and vertebrates the fundamental operation of the circadian clock is thought to be as a transcription-translation oscillator, in which the rhythmic regulation of expression of various clock genes is fundamental [3]. On the other hand, the circadian clock of *S. elongatus* has at its core a purely post-translational oscillator capable of being reproduced *in vitro* [129]. This post-translational oscillator is made up of just 3 purified proteins, KaiA, KaiB, and KaiC, which undergo a phosphorylation oscillation in ATP buffer at appropriate concentrations [133]. Because of its relative simplicity this biochemical oscillator makes an ideal model system for identifying the systems-level aspects of how feedback structure affects dynamics. We examine different proposed models for this oscillator and distinguish them based on their feedback structure. We demonstrate that models with opposing feedback structures change their periods in opposite directions when the strength of a crucial interaction is reduced. We demonstrate that this could be done experimentally by introducing a protein that would bind competitively with one of the clock proteins at a particular binding site and, using existing experimental results for proteins making up the output mechanism for the clock, show that the negative feedback model predicts the correct change in period.

1.2 Growth and morphogenesis

To understand how life is organized not only in time, but in space, it is necessary to study how the various features of an organism achieve their relative sizes and identities. This is called morphogenesis is a very complex coordination process wherein mostly genetically identical cells differentiate into a tremendous variety of cell types. All of the various organs and tissues of the organism then develop from these differentiated cells. Each of these tissues must not only adopt the correct cell type but must also further proliferate to the appropriate size and shape. The fine details of how this is all coordinated are often obscure, but even through all of the biochemical complexity involved in development it is possible to analyze hypotheses about the general mechanisms at play.

One such mechanism is a family of signaling molecules known as morphogens, which take on some spatial distribution (for instance by being produced in some localized area and diffusing away) which then plays a role in determining cell fates. This concept was proposed by Wolpert in 1969 [193], and the first protein to be identified as having a concentration-

dependent effect on morphogenesis was *bicoid* in 1988 by Christiane Nüsslein-Volhard and Wolfgang Driever [42]. Many others have been discovered since, including *hedgehog* and *dpp*, both of which have homologs in humans and in fact many metazoans [72,78]. However, while these morphogens undoubtedly play a crucial role in ensuring that the various tissues that they regulate develop in the correct manner, the precise details of how this occurs are often obscure.

The study of control of growth and size is intimately related with that of morphogenesis. The key signaling proteins of morphogenesis play an important role in controlling growth and transplant experiments, for example in salamanders [180] and rats [167], show that transplanted organs retain information about the donor. These transplanted organs can continue to grow at the same rate as they would in the donor and even reach a dramatically different size from the native organs if the *in situ* size of the donor organ was larger than that normal to the recipient. In *Drosophila* is has been shown that if the wing imaginal disk, a larval tissue that becomes the wing during metamorphosis, is dissected from the larva and cultured in the abdomen of an adult it reaches the approximate size that the disk reaches during normal development [23]. It is also insensitive to perturbations in quantities such as the precursor cell number, pupariation time, local variations in growth rate as well as others [67]. This robust, organ autonomous regulation of total tissue size is a remarkable result. The *Drosophila* wing imaginal disk presents a unique platform for the study of how regulation of signaling pathways introduces feedback and control on growth, which, since the publication of *On Growth and Form*, has been intimately related with questions of mechanics.

The continuum mechanics of tissue and organ growth has been a rapidly developing field. The earliest work on growth from the perspective of continuum mechanics formulates growth as an addition of mass either in the bulk of the material or as growth from a surface (as in the case of bones and horns) [169]. The possibility of growth inducing mechanical stress was first considered analytically in [155]. This is understood as growth deforming the material in such a way that there is no longer a stress-free state compatible with normal Euclidean space. This framework has been applied with success in areas from human arteries [159] to flower development [20].

In fact, growth feeding back on itself via stresses generated by growth has been implicated as having an important role in controlling the development of the *Drosophila* wing disk. Mechanical feedback was originally introduced as a means for explaining the observed near-uniformity of the growth rate in light of the highly non-uniform distributions of morphogens [166]. Since local overgrowth can cause mechanical stresses, if stresses feed back negatively

on growth then nonuniformities in growth could be diminished, leading to the observed macroscopic uniformity of growth. There has been subsequent support for the presence of mechanical feedback in this tissue [139,162], indicating that mechanical feedback is necessary for the usual development of the disk. There have also been numerical models [1,2,76] that have shown that mechanical feedback can lead to the eventual halting of the growth of the tissue.

This, however, leaves an apparent paradox. If mechanical feedback functions primarily to generate uniform growth, which does not induce any stresses, how can a mechanical feedback model predict the halting of growth at a precise final size, as is observed? This is resolved in different ways in different models. We demonstrate that the models presented above fall into qualitatively distinct model families. The way in which each model family resolves the apparent paradox is related to whether or not they predict a unique final size for the wing disk. We show that models that do not allow growth over macroscopic sections of the disk cannot predict a unique final size. In contrast, mechanical feedback models that do predict a unique final size fall into classes determined by whether or not feedback from pressure gradients is present, and this determines the spatiotemporal patterning of apoptosis in response to sharp changes in morphogen levels.

1.3 The structure of this work

Due to the breadth of the topics spanned in this thesis it has been split into two main chapters, one on oscillator models and one on growth models. Each of these chapters will be independent of the other. More detailed background and motivation for each topic will be presented at the beginning of each chapter and a more exhaustive summary of results will be presented at the end of each chapter.

Chapter 2 discusses models of the circadian clock of *S. elongatus*. This oscillator has been modeled in a number of different ways but the sign of the feedback present in the biochemical oscillator has not yet been conclusively identified. We examine two models for the oscillator that propose opposite signs for the dominant feedback mechanism. As discussed in section 1.1, we show that the two models have very similar biochemical foundations but differ greatly in terms of their dynamics and feedback structure, and that they can be distinguished by introducing protein species that affect the feedback strength.

Chapter 3 discusses models of growth control by mechanical feedback in *Drosophila*. In particular we study models of the wing imaginal disk which has been shown to have

a robust, organ autonomous final size. We compare different models of size control by mechanical feedback by introducing an analytic framework that places different models on equal footing. This allows us to derive and compare macroscopic predictions about the growth dynamics for the different models. As discussed in 1.2 we show that models that require growth to vanish over macroscopic sections of the tissue cannot predict a unique final size.

In both of these studies is was equally necessary to demonstrate how the types of model are different and to understand how they can be compared on the same footing. In the case of the circadian oscillator models it was necessary to examine how a key protein interaction plays a very different role in models with different feedback structures. Then the models could be distinguished by observing that they predicted opposing changes in the period when this key interaction was disrupted. For the growing tissue system it was necessary to develop an analytic framework which is capable of representing macroscopic observables about patterns (such as uniformity of growth or spatial localization of apoptosis) that emerge during growth. The key differences in the families of growth control models can then be described in terms of these experimental observables, and the presence or absence of a precise final tissue size can be related to these observables by the details of the feedback present. In each case finding common regimes to compare different models led to insight into how to connect the results to phenomena that can be measured experimentally.

Chapter 2

Distinguishing Feedback Mechanisms in Clock Models

2.1 Introduction

Circadian clocks are used by many organisms and are thought to provide advantages by synchronizing biological processes with the earths day/night cycle. These time-keeping systems are biological oscillators capable of being entrained by periodic signals (like the daily cycle of light and dark) and of sustaining a robust period near 24 hours in the absence of external signals. Biological activities as diverse as metabolism [157] and gene regulation [128] have been shown to depend on circadian rhythms. The design of these oscillators can be very intricate. Studies in various model systems have led to a number of conjectures about the consequences of different feedback architectures for clock performance. For example, it has been suggested [51, 86, 99] that the prevalence of positive feedback loops in biological oscillators could make oscillations simpler to achieve, while other studies [90] have shown that additional negative feedback loops can provide advantages in robustness. Being able to identify signatures of different types of feedback structures present in simple experimental systems enables direct studies of the importance of generic design principles for forming reliable biological rhythms. Here we distinguish the signatures of two types of feedback loops found in different models of a particularly simple circadian oscillator, that belonging to the cyanobacterium Synechococcus elongatus. In particular, we aim to determine whether strong positive feedback is essential to the in vitro functioning of the Kai clock derived from S. Elongatus.

The S. Elongatus circadian clock is built around a core post-translational protein phos-

phorylation cycle that has the striking property that it can be reproduced in vitro with purified proteins [129]. It consists of the 3 proteins KaiA, KaiB, and KaiC [133], which form complexes rhythmically in the presence of ATP. Over the course of an oscillation cycle, dimeric KaiA binds to the C-terminal domain of KaiC. KaiC forms a homohexamer in the presence of ATP, promoting autophosphorylation of KaiC on a threonine and then a serine residue on each KaiC monomer [83, 132, 158, 191, 194]. Phosphorylation induces conformational changes in the KaiC hexamer which promote KaiB binding to the KaiC N-terminal domain [28, 83, 92, 143, 194]. This KaiBC complex can then bind and sequester KaiA, preventing it from inducing autophosphorylation in other KaiC. In the absence of free KaiA, hexamers dephosphorylate. The unphosphorylated hexamers unbind the KaiB, releasing the KaiA from sequestration. These KaiA are then free to phosphorylate KaiC hexamers and repeat the cycle (figure 2.1).

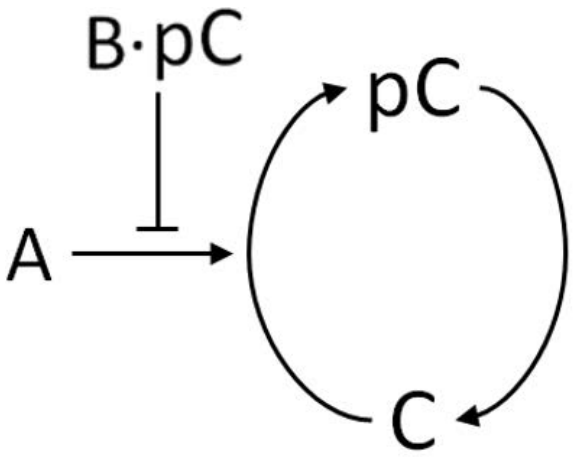

Figure 2.1: Schematic of the Kai oscillator. KaiC hexamers autophosphorylate on serine and threonine residues in the presence of KaiA. Phosphorylated KaiC can sequester KaiA in a KaiABC complex, causing KaiC to dephosphorylate.

This cycle of protein interactions has been previously modeled in different ways [21, 32, 47, 124]. Here we study two different proposed models for the Kai system that both focus on the importance of KaiA sequestration. We show that, even though they assume similar molecular interactions, their distinct mathematical properties can be experimentally distinguished. We call these models the allosteric and monomer models due to the focus of the first model on the roles of different KaiC hexamer conformations and of the second on the multiple possible phosphorylation states of KaiC monomers.

These two models of the Kai system can be understood as representing examples of two qualitatively different mechanisms for generating oscillations in biological systems. The

allosteric model, relying on negative feedback [186], is an example of a delay-based oscillator. In these oscillators a time delay and negative feedback drive the system past steady state, generating oscillations (figure 2.2). Delays can come from many different sources, from protein synthesis times to long chains of intermediate reactions [182].

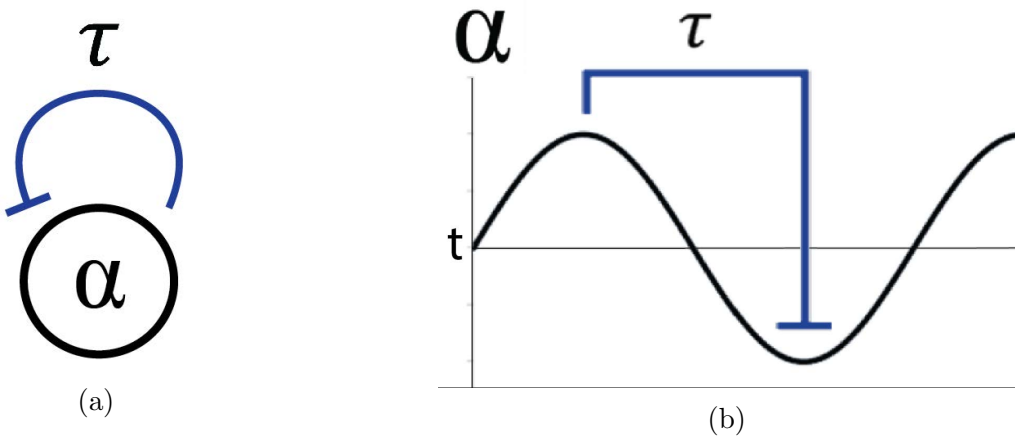

Figure 2.2: Delay oscillators operate by delaying negative feedback, indicated by flat arrows in blue. (a) Schematic delay oscillator: a protein α feeds back negatively on its own activity with time delay τ. (b) A peak in α activity leads to delayed inhibition, inducing a trough at a time τ later. This trough relieves the inhibition, allowing the signal to recover towards a peak after another delay of order τ.

The monomer model [158] is an example of a relaxation oscillator [173] that relies on strong positive feedback (figure 2.3a). The positive feedback causes the system to overshoot an unstable steady state, effectively switching between two slowly evolving states. This action can be understood in analogy to the delay oscillator: whereas the delay oscillator used a dependence on the previous state of the system to prevent the system from settling at a steady state, a relaxation oscillator achieves a similar effect with hysteresis, which keeps the system moving past the steady state. It also exhibits a strong separation of timescales: the system evolves along one of the slow states until it reaches a turning point and then, much more quickly, switches to the other slow state (figure 2.3b).

The question of whether the in vitro Kai system is best described as a delay or a relaxation oscillator has yet to be resolved experimentally, as current results appear to provide contradictory evidence. The basic issue is whether KaiA bound to the KaiC C-terminal is only active during the phosphorylation phase of the oscillation or also effectively retards dephosphorylation. Even though the in vitro Kai system appears, by the standards of biological clocks, to be quite simple, it is still difficult to measure all of the relevant rate

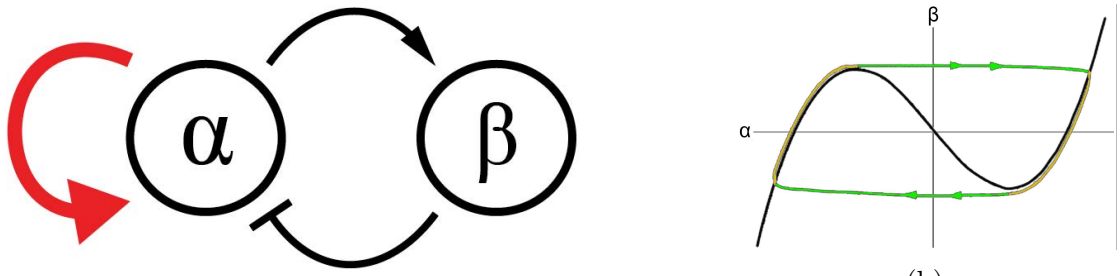

(a) (b)

Figure 2.3: A relaxation oscillator operates with a combination of positive and negative feedback. (a) The simplest kind involves two species, α and β. Positive feedback, indicated with a red arrow, on one of these (α in this case) causes the system to push past its steady state instead of settling down, producing an oscillation. This is most effective when there is a strong separation of timescales, with α evolving much faster than β. (b) The relaxation oscillator limit cycle in the α-β phase plane. Positive feedback on α gives it a bistable nullcline (black). The system evolves slowly along one branch of the nullcline until one of the extrema are reached (yellow). It then moves quickly to the other branch (green) and repeats the process.

constants directly, and different approaches to estimating their values do not agree. In particular, experiments in which phosphomimetics are used to isolate certain reactions by fixing the phosphorylation state of one of the residues [29, 132] seem to conflict with studies in which rates are instead inferred from fitting a kinetic model with multiple reactions to phophorylation time courses of the native protein [158].

Here we show how the different possibilities for the type of feedback caused by KaiA sequestration can be distinguished experimentally without direct measurement of microscopic rate constants. We first introduce the models in detail and describe the distinct assumptions they make about the form of the feedback introduced by KaiA sequestration. We show that the allosteric model and the monomer model exhibit opposite responses in both amplitude and period to changes in the efficiency of KaiA sequestration by the KaiB complex. These responses can be understood as consequences of the type of feedback each model exhibits. We then show that such changes in sequestration efficiency can be generated experimentally by a protein that competes with KaiA for binding on the KaiC N-terminal domain in the KaiBC complex. Recent research indicates that CikA is a strong candidate for this role [178]. Addition of CikA to the in vitro oscillator results in a decreased period [26], consistent with the results for the allosteric model. We finally show that the same qualitative behavior is seen in extensions of the basic allosteric and monomer models which maintain the same

fundamental feedback structure [146, 203], including recent models that aim to provide a more detailed description of the biochemistry of the Kai proteins [138]. Varying efficiency of KaiA sequestration thus provides a robust way to directly probe whether the Kai oscillator is closer to a delay oscillator or to a relaxation oscillator.

2.2 Models

In this section we describe the allosteric and monomer models and distinguish their feedback structures. In particular, we define the sequestration efficiency m as the amount of KaiA sequestered per KaiC (per KaiC hexamer for the allosteric model and per KaiC monomer for the monomer model), which will play a central role in our analysis of each of the following models. In the interest of showing that the principles valid for these comparatively simple models hold in a more realistic setting we then introduce a third model, the two-site allosteric model [138], that attempts to more faithfully capture the biochemical complexities of the full system.

2.2.1 Allosteric Model

The allosteric model, introduced in [186], (figure 2.4a) takes hexameric KaiC as its fundamental object. It combines the two phosphorylation sites on each monomer into one lumped site and assumes that each hexamer exists in one of two different allosteric states called active and inactive in analogy with the Monod-Wyman-Changeux model of conformational transitions. The transition rates between different conformations are assumed to depend on the number of phosphorylated monomers in a hexamer, with more phosphorylated hexamers preferring the inactive state and less phosphorylated hexamers preferring the active state. As the system evolves the population of active hexamers becomes sequentially more phosphorylated until the inactive conformation is preferred. Once in the inactive conformation the population then begins to dephosphorylate until it switches back to the active conformation. The large number of elementary steps in each of these processes produces the delay that is at the core of the oscillator.

In the allosteric model a KaiA monomer can bind to both active and inactive KaiC. KaiA binds to active KaiC and promotes autophosphorylation before unbinding. After a KaiC hexamer has changed conformation to the inactive state it can form a complex with two KaiB dimers which in turn binds KaiA dimers, thereby sequestering KaiA and preventing it from promoting phosphorylation. The inactive KaiC then dephosphorylates and begins to

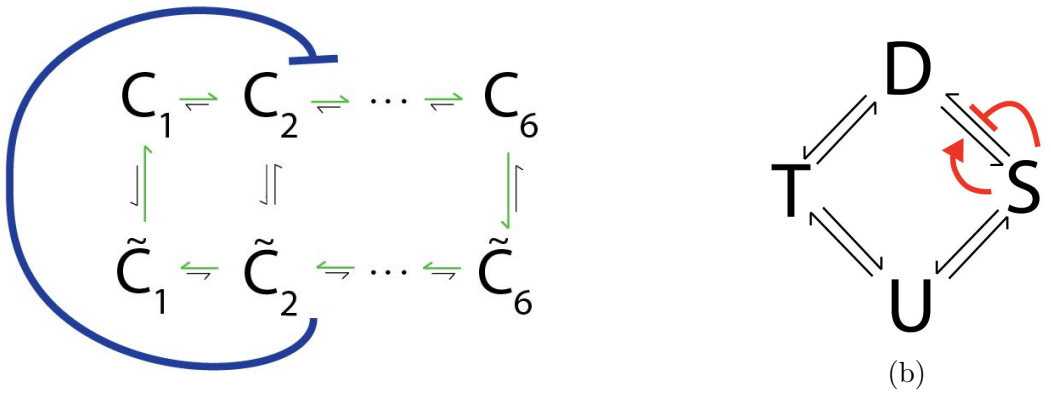

(a) (b)

Figure 2.4: The allosteric and monomer models. Effective negative feedback, blue, flat arrowhead; effective positive feedback, red. (a) In the allosteric model, the oscillation proceeds by the phosphorylation of KaiC hexamers in the active conformation, denoted C_i, followed by a conformational change and dephosphorylation of inactive hexamers ($\tilde{C}_i$). Green arrow indicates dominant direction of conformal transitions. The inactive KaiC sequesters KaiA, preventing the active KaiC from phosphorylating, introducing the negative feedback and delay shown in the blue. (b) The monomer model involves transitions between 4 different phosphorylation states on a KaiC monomer, where a serine and a threonine residue can each be either phosphorylated or unphosphorylated. Unphosphorylated KaiC (U) becomes phosphorylated on the threonine (T) and then on the serine, making it doubly phosphorylated (D). When the threonine dephosphorylates, only the serine remains phosphorylated (S). It is this state that can sequester KaiA. This sequestration has the effect of increasing rate of $D \to S$ transitions while decreasing the $S \to D$ rate. Both of these interactions amount to positive feedback of S on its own concentration and so are shown in red above.

switch to the active state, at which point it begins to release the sequestered KaiA. When enough KaiA is free it induces the active KaiC to autophosphorylate until the inactive state is preferred again, completing the cycle. Thus the net effect of KaiA sequestration by inactive KaiC in the allosteric model is a negative feedback with a delay (figure 2.2), preventing active KaiC from phosphorylating and retarding the progression of the cycle until dephosphorylation is complete. This model is described by the following chemical

reactions [186], with mass action kinetics:

$$\begin{gathered} C_i \leftrightharpoons \tilde{C}_i \\ C_i + A \leftrightharpoons AC_i \to C_{i+1} + A \\ \tilde{C}_i + 2B \leftrightharpoons B_2\tilde{C}_i, \quad B_2\tilde{C}_i + mA \leftrightharpoons A_mB_2\tilde{C}_i \\ C_i \leftrightharpoons C_{i+1}, \quad \tilde{C}_i \leftrightharpoons \tilde{C}_{i+1} \\ B_2\tilde{C}_i \leftrightharpoons B_2\tilde{C}_{i+1}, \quad A_mB_2\tilde{C}_i \leftrightharpoons A_mB_2\tilde{C}_{i+1} \end{gathered} \tag{2.1}$$

Here C_i represents a KaiC hexamer in the active state with i phosphorylated monomers (i ranging from 0 to 6) and $\tilde{C}_i$ represents a KaiC hexamer in the inactive state, and C_T represents the total concentration of KaiC hexamers. A and B stand for KaiA and KaiB, respectively, and m is the KaiA sequestration stoichiometry. (Below we will take m to be a continuously varying real number, and extend mass action kinetics to this case.) Since the Kai oscillation is most commonly understood as a phosphorylation oscillation, we will also often consider the quantity $p(t)$, the phosphorylation fraction as a function of time. This is the proportion of KaiC monomers that are phosphorylated, and is defined by

$$p(t) = \frac{1}{C_T}\left(\sum_{i=0}^{6} iC_i + \sum_{i=0}^{6} i\tilde{C}_i + \sum_{i=0}^{6} iA_mB_2\tilde{C}_i + \sum_{i=0}^{6} iB_2\tilde{C}_i + \sum_{i=0}^{6} iA_mB_2\tilde{C}_{i+1}\right) \tag{2.2}$$

Unless otherwise stated, the parameters used for simulations of the allosteric model are those found in table S2 of [186].

2.2.2 Monomer Model

The monomer model (figure 2.4b), proposed in [158], takes the individual KaiC monomer as its basic unit. It relies on ordered phosphorylation on the two residues (serine and threonine) that are known to have a key contribution to the circadian oscillation. In this model, if all KaiC monomers begin in the fully unphosphorylated state U, first the threonine residue is phosphorylated, then the serine is phosphorylated yielding a doubly phosphorylated D monomer, then the threonine is dephosphorylated and finally the serine is dephosphorylated. This leads to the following cycle describing a full oscillation: $U \to T \to D \to S \to U$.

In the monomer model the presence of free KaiA directly alters the rates of each phosphorylation reaction as shown below. High free KaiA promotes phosphorylation and low

free KaiA promotes dephosphorylation. KaiA binding is not explicit, instead, it is presumed that the concentration of free KaiA is a bound immediately by any available S KaiC until there is no remaining free KaiA. Thus as the amount of S KaiC increases it sequesters more and more KaiA, promoting dephosphorylation and turning D KaiC into S KaiC, leading a relatively small amount of S KaiC to produce more S KaiC, and to inhibit its phosphorylation into D KaiC. Therefore, in the monomer model, KaiA sequestration effectively acts to catalyze the production of S KaiC, which in turn causes more sequestration. This suggests that the monomer model is an example of a relaxation oscillator (figure 2.3), in which the cycle can progress only when enough free KaiA is sequestered to trigger the strong positive feedback which causes the sequestration of all free KaiA, at which point the KaiC monomers can fully dephosphorylate. The model is described by the following system of differential equations [158]:

$$\begin{aligned}
\frac{dT}{dt} &= k_{UT}(S)U + k_{DT}(S)D - k_{TU}(S)T - k_{TD}(S)T \\
\frac{dD}{dt} &= k_{TD}(S)T + k_{SD}(S)S - k_{DT}(S)D - k_{DS}(S)D \\
\frac{dS}{dt} &= k_{US}(S)U + k_{DS}(S)D - k_{SU}(S)S - k_{SD}(S)S
\end{aligned} \tag{2.3}$$

The U concentration is then determined by the conservation of total KaiC:

$$C_T = U(t) + S(t) + T(t) + D(t) \tag{2.4}$$

The amount of free KaiA is given by :

$$A(S) = \max\{0, A_T - mS\} \tag{2.5}$$

Here the sequestration stoichiometry $m = 2$ by default but we will treat it as a parameter to be varied in the subsequent section. The model then in effect assumes that KaiA has infinite affinity for S-KaiC. The S dependence of each of the reaction rates is given by (with α and β standing in for U, T, S, or D):

$$k_{\alpha\beta}(S) = k^0_{\alpha\beta} + \frac{k^A_{\alpha\beta}A(S)}{K_{1/2} + A(S)} \tag{2.6}$$

Again, we will often consider a phosphorylation fraction $p(t)$. It is defined here as the sum

of the concentrations of all phosphorylated forms of KaiC:

$$p(t) = T(t) + D(t) + S(t) \tag{2.7}$$

Unless otherwise noted the parameters for this model are those found in [158] in table S2 of the supporting information.

2.2.3 Two-Site Allosteric Model

Although our main focus is comparison of simple models that are relatively pure delay or relaxation oscillators, below we also investigate whether our conclusions carry over to a more complex, biochemically realistic model. In particular, we consider the two-site allosteric model, described in detail in [137, 138]. Like the allosteric model treated above, describes the Kai system at the level of individual hexamers. Contrary to the allosteric model, however, the two-site allosteric model also explicitly describes the state of individual monomers, and in particular their serine and threonine phosphorylation sites, as shown in figure 2.5. Furthermore, each monomer now has two domains called the N-terminal and C-terminal domain. KaiA can bind to the C-terminal domain, where it will enhance the phosphorylation of all the monomers in the hexamer. Each monomer in the hexamer is phosphorylated in a well defined order: First the threonine site is phosphorylated and then the serine site. Phosphorylation of the two sites has an antagonistic effect on the conformational state of the hexamer: The U and T states stabilize the active conformation and the D and S states stabilize the inactive conformation. Due to this antagonism, the relative stability of the conformations does not depend on the absolute number of monomers in a certain state, as is the case in the allosteric model, but rather on the difference between the number of phosphorylated threonine and serine sites. Roughly, when more serine sites are phosphorylated than threonine sites, the hexamer will switch conformation. After flipping to the inactive state, the hexamer binds KaiB on its N-terminal domain. In the model, KaiA is sequestered by the N-terminal domain only after 6 KaiB monomers are bound. The resulting delay allows hexamers lagging behind the main population to continue phosphorylation and reach the inactive state, which is an essential property of this model to generate robust oscillations. See Table S1 (SI) for information on the parameters used.

Since each monomer is modeled as having 4 phosphorylation states, which all play a role in determining the allosteric state of the whole hexamer, the number of states in the model is combinatorially large. Because of this, we follow the time evolution of the system using

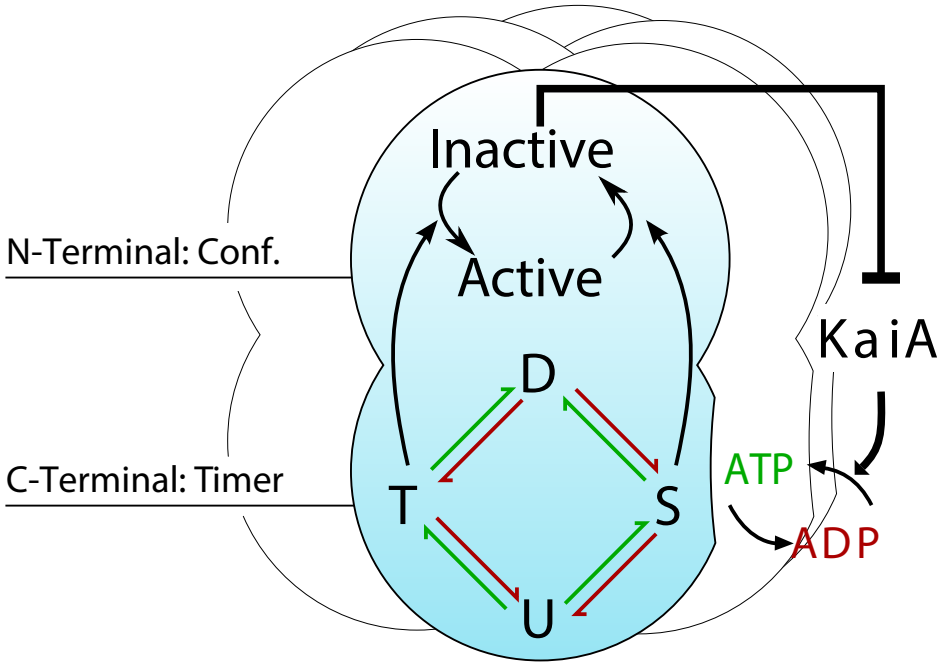

Figure 2.5: Cartoon of the two-site allosteric model, which accounts for both the hexameric nature of KaiC and the presence of 2 distinct phosphorylation sites each monomer. Each KaiC monomer consists of a N-terminal and a C-terminal domain: the N-terminal domain drives the conformational change of the hexamer between the active and inactive state and the C-terminal domain determines the timing of this switch through the ordered phosphorylation of its two phosphorylation sites. Phosphorylation of the threonine site (T-state) stabilizes the active state and phosphorylation of the serine site (S-state) stabilizes the inactive state. Phosphorylation can only occur with ATP (green arrows) and dephosphorylation only with ADP (red arrows) in the C-terminal binding pocket. (Figure adapted from [137].)

a kintetic Monte Carlo algorithm. This large number of states, as well as the way in which sequestration negatively feeds back on a different part of the cycle, it seems plausible that this model represents an oscillator primarily driven by delayed negative feedback, but it is more ambiguous than the fairly direct case of the simple allosteric model.

2.3 Results

The models presented in the previous section differ in their assumptions, in particular about the type of feedback introduced by KaiA sequestration. Since enzyme sequestration has been identified as being crucial for synchronization of individual molecular oscillators into coherent population-level rhythms in the Kai system [86], it is reasonable to expect that these differences have important consequences for the dynamics of these models.

Sequestration blocks the progression of the oscillation in each of the models described here. In the allosteric model sequestration acts to keep active KaiC hexamers from beginning to phosphorylate before enough inactive hexamers have fully dephosphorylated and released their KaiA. This effectively causes KaiA sequestration to feed back negatively, with a delay, on the phosphorylation of active KaiC. On the other hand, in the monomer model, the dynamical effect of KaiA sequestration is to cause S KaiC to induce its own production, leading to the full sequestration of all free KaiA before the cycle can advance. This results in strongly bistable behavior, with KaiA sequestration controlling the switch between two slowly-evolving states. This mechanism, blocking the progression of the oscillation until sufficient sequestration has occurred, is qualitatively different from that in the allosteric model, most notably in that the block is relieved by changing the concentration of free KaiA in the opposite direction.

To investigate how this fundamental difference affects the behavior of the oscillators we vary the KaiA sequestration stoichiometry m (defined by equations 2.1 & 2.5, for the allosteric and monomer models, respectively), understood as a continuous variable describing the average number of KaiA monomers sequestered per KaiC in each model (per KaiC hexamer in the allosteric model and per KaiC monomer in the monomer model). We find that changing m has the opposite effect on both the amplitude and the period of the oscillation in the two different types of models. Directly modifying m continuously is of course only possible in abstract mathematical models, and cannot be related directly to experiment. In order to relate to realizable systems we will then show that modifying the models to explicitly include a competitive binding protein for the KaiA sequestration site on KaiC produces the same qualitative results as directly varying the sequestration stoichiometry. We show that our results extend to common variants and extensions of the basic allosteric and monomer models in the (see Supporting Information).

2.3.1 Allosteric Model: Less efficient sequestration decreases period

We first consider the allosteric model. In figure 2.6a we see three time traces of the fraction of phosphorylated KaiC $p(t)$ (defined in eqn. 2.2). These show that increasing the sequestration stoichiometry m and thus the efficiency of sequestration increases both the amplitude of the oscillation and the period. Figure 2.6d shows that this behavior is consistently observed over a fairly broad range of values of m.

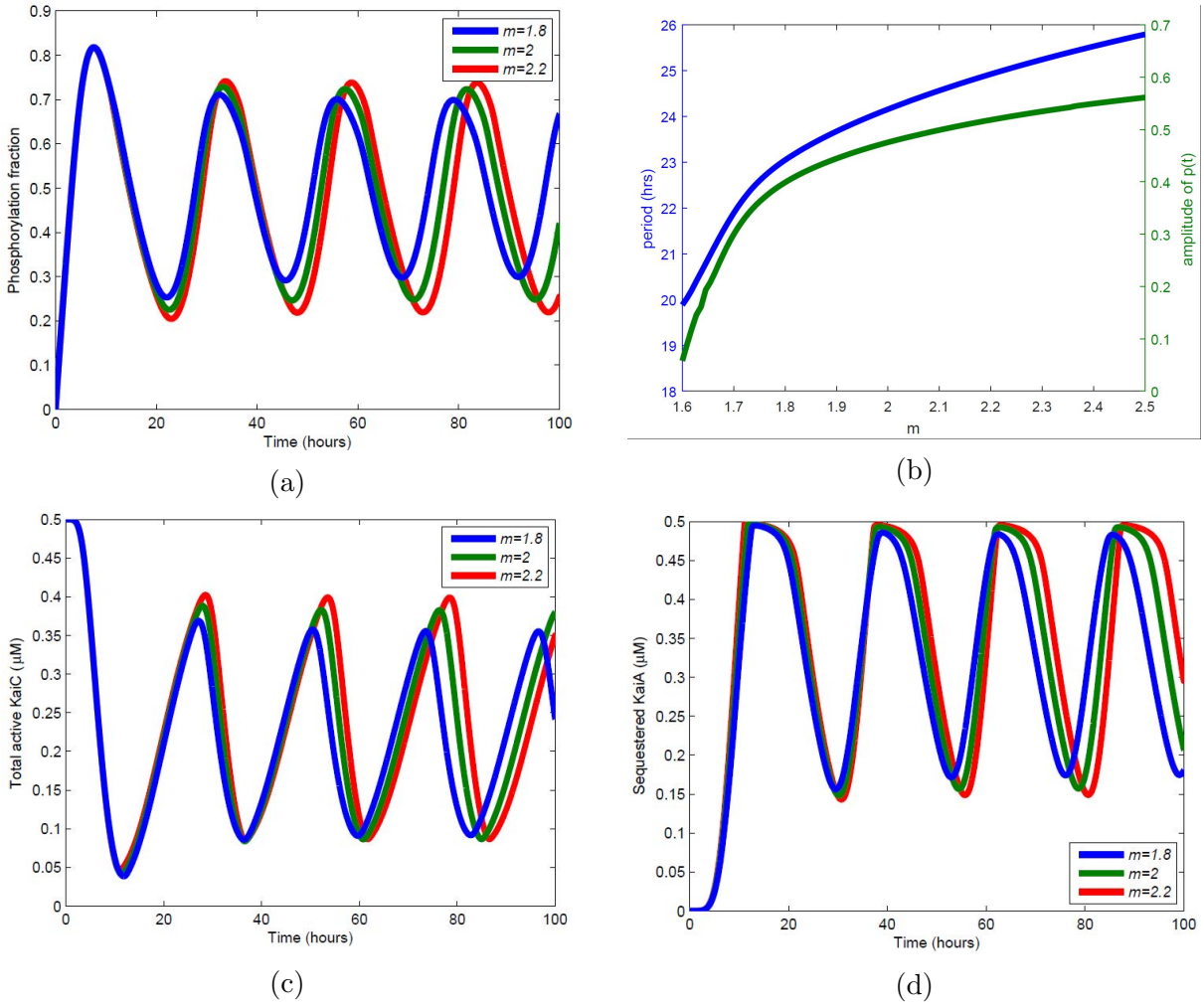

Figure 2.6: Varying the efficiency m of KaiA sequestration in the allosteric model. (a) Time traces of the phosphorylation fraction $p(t)$ for three different values of m. In this model m varies in the same direction as the amplitude and the period of the oscillation. (b) This relationship can be seen over a wide range of m. (c) The concentration of total active KaiC, $\sum_{i=0}^{6} C_i^T$, for three different values of m. The decrease of the maximum with m indicates that at higher m less KaiC has switched to the active conformation before the majority switches to the inactive conformation and begins dephosphorylating, indicating decreased synchronization. (d) The concentration of sequestered KaiA, defined as $m \sum_{i=0}^{6} \frac{A^m B_2 \tilde{C}_i^T}{\tilde{K}_i^m + A^m}$. As m decreases, the maximum amount of sequestration also declines, allowing more KaiC to phosphorylate even when most KaiC is inactive. Additionally, the minimum amount of sequestered KaiA is higher, reflecting the presence of more inactive KaiC when the majority is active.

To understand this observation mechanistically, consider the effect of decreasing m. Since m only controls the sequestration of KaiA, changing it has no direct effect on the active KaiC and therefore no direct effect on the dynamics of phosphorylating KaiC. It also does not affect the dephosphorylation rates. Decreasing m can only affect the timing of KaiA sequestration. If m decreases, the same amount of KaiC sequesters less KaiA. Thus there is relatively more free KaiA, including during the phosphorylation portion of the cycle (figure 2.6d). This has two consequences: first, more active KaiC can begin phosphorylating while a substantial amount is still in the inactive state, and the oscillations of individual KaiC hexamers are less synchronized (figure 2.6c). Therefore there is more unphosphorylated KaiC when $p(t)$ reaches its maximum and less when it reaches its minimum, explaining the decrease in the amplitude of the oscillation. Second, the phosphorylation phase can begin sooner, since when an inactive hexamer releases its sequestered KaiA and becomes an active hexamer, the inactive hexamers that remain are less able to sequester the newly released KaiA. This causes more KaiA to be freed sooner, accelerating the phosphorylation phase.

2.3.2 Monomer model: Less efficient sequestration increases period

The situation is reversed in the monomer model, as can be seen in figure 2.7, which shows that both the amplitude and the period decrease with increasing m. As in the allosteric model, this behavior can be understood mechanistically. A fundamental difference between this model and the allosteric model is that in the monomer model dephosphorylation can only begin once a certain threshold amount of KaiA has been sequestered, since the balance between phosphorylation and dephosphorylation is directly dependent on the concentration of free KaiA. This, combined with positive feedback whereby sequestration favors the $D \rightarrow S$ transition, which in turn favors more sequestration, causes the model to produce switch-like behavior. In addition, this model also shows a strong separation of timescales. Once a certain amount of KaiA is sequestered dephosphorylation occurs relatively quickly (figure 2.7a) compared to the time it takes to recover from dephosphorylation. Effectively, decreasing m increases the amount of S-KaiC necessary to reset the switch controlling the balance between phosphorylation and dephosphorylation. This means that the duration between most KaiC becoming fully phosphorylated and the switch resetting must increase, since S-KaiC builds up very slowly until the strong positive feedback kicks in and rapidly causes the remaining KaiA to be sequestered. The duration where all KaiA is sequestered (figure 2.7d) does not seem to change significantly with m; increasing m instead decreases the amount of S needed

to fully sequester all of the KaiA. This can be usefully contrasted with figure 2.6d which shows that the allosteric model does not even need to sequester all of the KaiA in order to function as an oscillator.

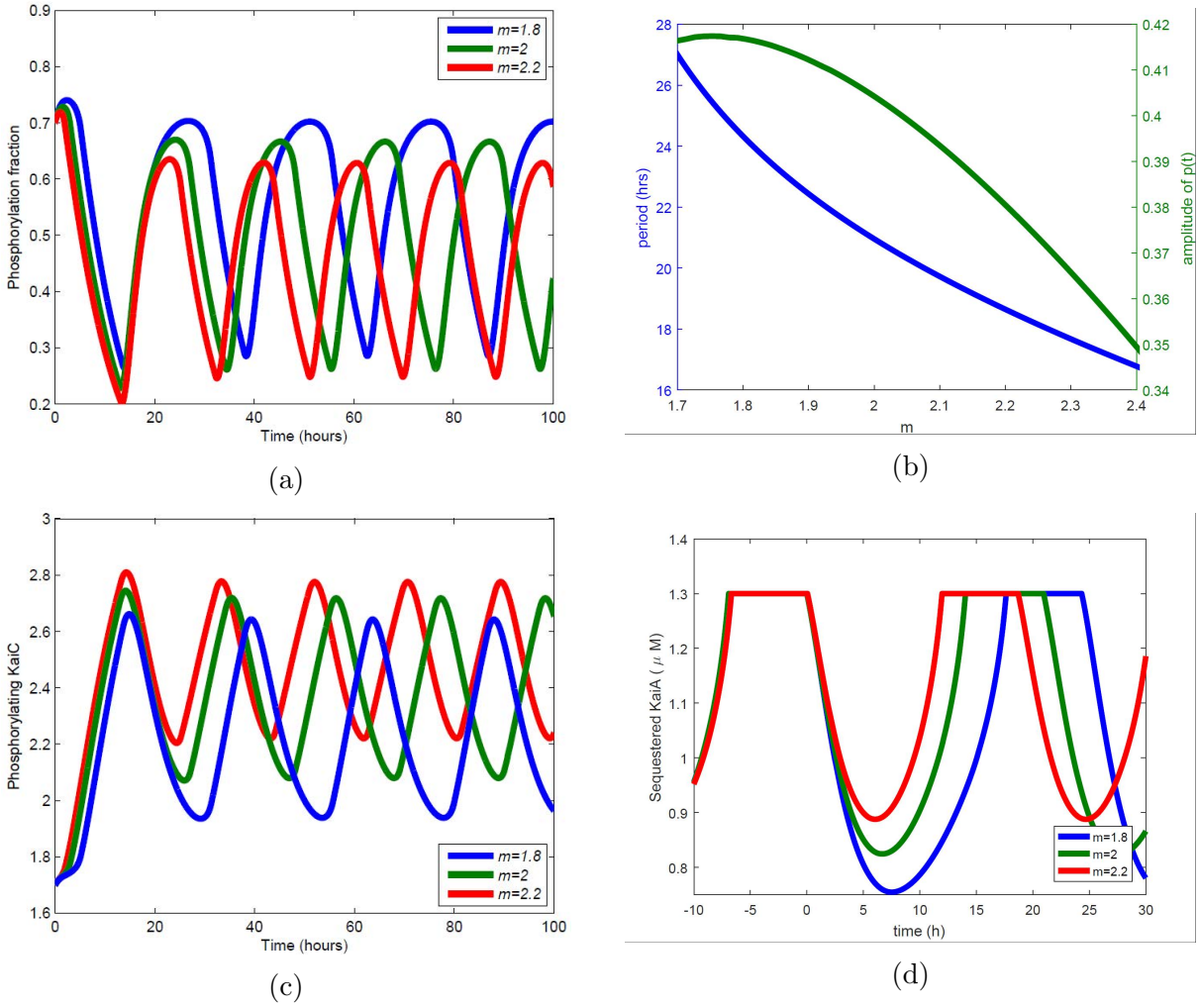

Figure 2.7: Varying the sequestration efficiency m in the monomer model. (a) Time traces of the phosphorylation fraction $p(t)$ for three different values of m. In this model m varies inversely with the amplitude and the period of the oscillation. (b) This relationship can be seen over a wide range of m. (c) The concentration of U and T KaiC, the closest analog to the active KaiC in the allosteric model, since these are the KaiC species that are competent to phosphorylate. Compared with Fig. 6c it can be seen that this model does not exhibit the same desynchronization as m is decreased. (d) The concentration of sequestered KaiA. Traces for different values of m are aligned so that dephosphorylation ends at $t = 0$. Compared to the allosteric model, this model sequesters all of the KaiA for part of the cycle, almost regardless of m. It can be seen that m does not affect the duration of dephosphorylation does not vary strongly with m, and that the majority of the variation in period comes from the approach to full sequestration. Once the necessary threshold of sequestered KaiA is crossed, positive feedback on S KaiC causes all of the KaiA to become sequestered.

2.3.3 Analytic perspective on changing m in the monomer model

Because the monomer model is low dimensional it is possible to understand these numerical results analytically. In order to make a more direct analysis we reduced the model from a 3 dimensional system to a 2 dimensional system by assuming that the phosphorylation and dephosphorylation of the threonine residue happen fast compared to that of the serine residue. This is a reasonable assumption since one of the observations of the original model is that the S phosphorylation is much slower than T phosphorylation [158]. In this limit $U \leftrightharpoons T$ is in steady state. Even though $S \leftrightharpoons D$ is fast, it is bistable so it cannot be set to steady state. With this in mind we change to a new set of variables $X = S - D$ and $Y = S + D$, with dynamics described by equation eq:MonoModelNewVars. We then have one fast variable, X, which describes the resetting of the switch, and one slow variable, Y, which describes the of dynamics of the serine phosphorylation state. Figure 2.8d shows the nullclines of the resulting 2 dimensional system in terms of $X$and Y. They can be seen to form the characteristic shape of a relaxation oscillator, describing slow evolution near the red nullcline and fast evolution between the two different branches of the nullcline. It is also possible to use this reduced system to provide an analytical explanation for the direction of the period dependence on m (See appendix A).

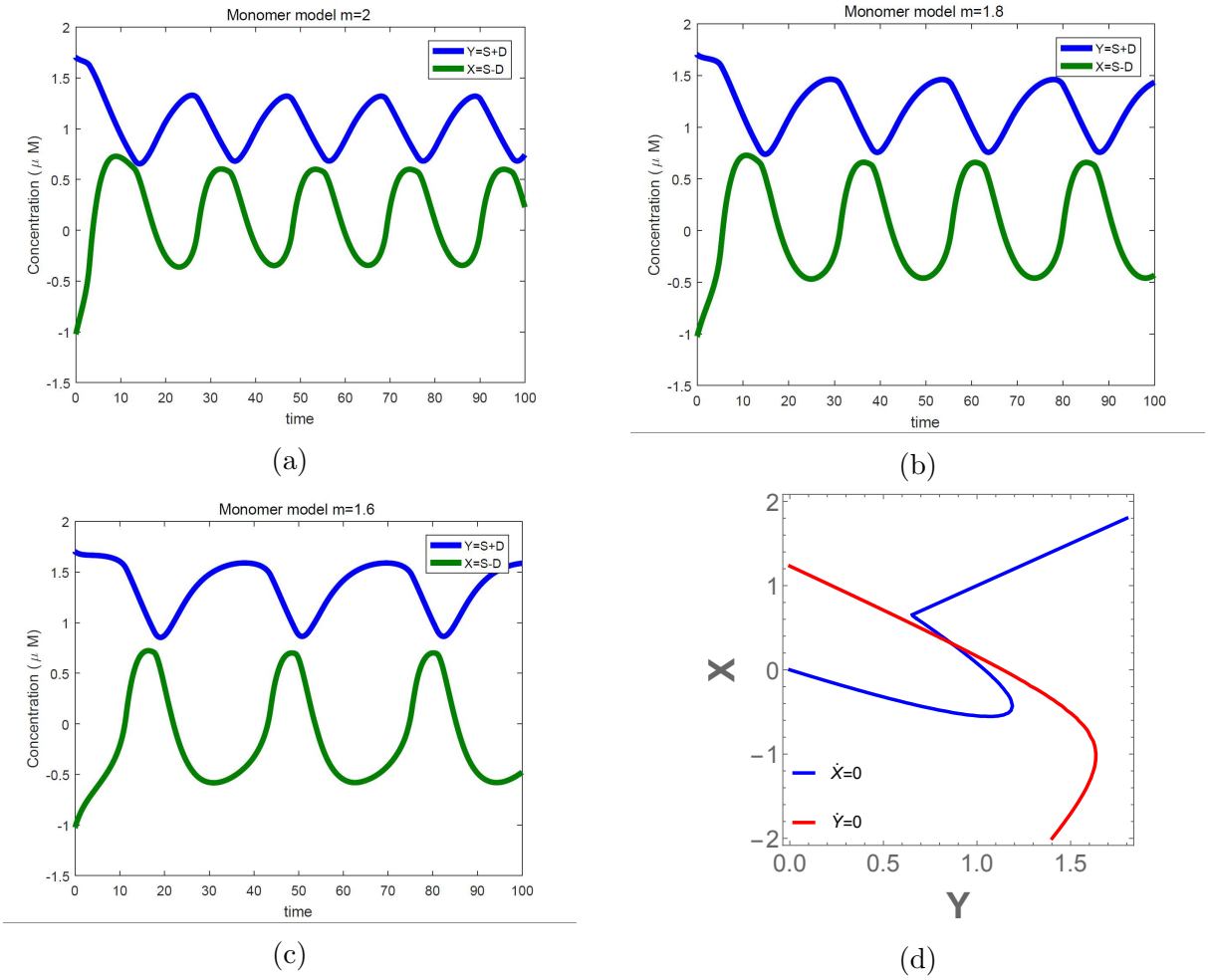

Figure 2.8: Dynamics inferred from the reduced model are apparent in time traces from the full monomer model, for $m = 2$ (a), $m = 1.8$ (b), and $m = 1.6$ (c). Changes in the sign of $X = S - D$are correlated with changes in the sign of the derivative of$Y = S + D$, indicating a switch along a fast degree of freedom. (d): A phase plane plot of the nullclines for a reduced monomer mode. The red nullcline corresponds to $X = S - D$ and the blue to $Y = S + D$. The X nullcline has 3 main branches, and the middle branch is intersected by the Y nullcline, a motif indicative of a relaxation oscillator.

We can use the intuition gained from this asymptotic analysis to look for traces of this behavior in the full model. For example, we can predict that if the oscillator takes longer to reach its threshold, X will still only be active very briefly, since it describes the switching and is controlled by the dephosphorylation dynamics, which do not depend on m. Additionally, jumps in X should be roughly coincident with changes in the sign of the derivative of Y, since the jumps between the two branches of the nullcline (indicating a large change in X) are the indicators that the slow dynamics of the system (indicated by Y) have reversed their direction. In figure 2.8 we can observe the full system in terms of the variables $X$and Yexhibiting these characteristic behaviors. These behaviors appear to be crucial to the functioning of the oscillator since they are present even when the sequestration becomes very inefficient, up until the oscillation ceases. Additionally it is possible to see that the majority of the effect on the period is an increase in the amount of time with little S, consistent with the finding for the reduced model that the amount of time spent unsequestered does not depend on m.

2.3.4 Competitive binding effectively modulates m

It is not possible to vary the parameter m directly in an experiment. A direct way to emulate changing the sequestration efficiency is instead to introduce a protein that can bind competitively with KaiA in the KaiB-KaiC sequestration complex but does not promote KaiC autophosphorylation (figure 2.9). This could be a truncated form of KaiA or a different protein that binds competitively with KaiA to the KaiC-KaiB complex (such as possibly CikA [178]). We will call this decoy KaiA or dKaiA, and unless otherwise stated it binds to the KaiB-KaiC sequestration complex with equal affinity to KaiA. Both models considered can be modified to include this interaction, and we will show that this modification produces the same result as varying m directly: although the maximum possible number of KaiA dimers sequestered does not change, the effective number of sites available is smaller due to some being occupied by dKaiA (figure 2.9).

Allosteric model

Here we introduce to the standard allosteric model the following interactions:

$$\begin{aligned} B_2\tilde{C}_i + mdA &\leftrightharpoons dA_mB_2\tilde{C}_i \\ dA_mB_2\tilde{C}_i &\leftrightharpoons dA_mB_2\tilde{C}_{i+1} \end{aligned} \tag{2.8}$$

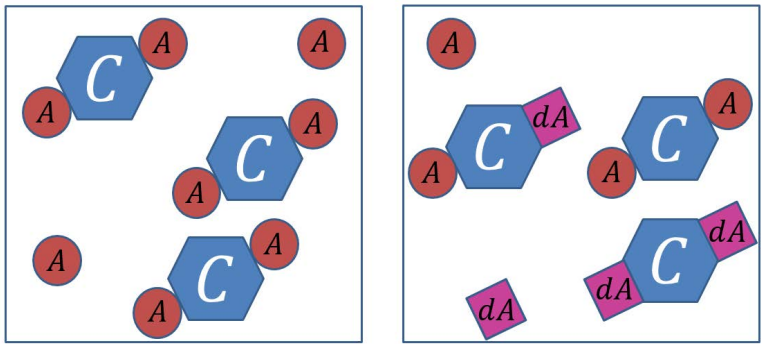

Figure 2.9: A schematic of a method for varying the KaiA sequestration efficiency m. By introducing a species (here shown as dA for decoy KaiA) that binds competitively with KaiA for the site at which KaiA is sequestered it is possible to experimentally vary the average amount of KaiA sequestered per KaiC.

We see in figure 2.10a that the addition of dKaiA to the allosteric model, whole holding m at a constant value of 2, shows the same behavior as changing $m$directly. This indicates that dKaiA competing for sequestration with KaiA causes KaiA to become unsequestered faster. Increasing the amount of free KaiA allows those KaiC that transition from the inactive conformation to the active conformation early to begin phosphorylating sooner. This essentially decreases the effect of the delay in the system, and since this model is primarily a negative feedback-delay oscillator this also corresponds to a decrease in amplitude.

Monomer model

As described, the monomer model foes not explicitly model formation of full KaiABC complex but instead assumes KaiA has infinite affinity for S-KaiC. If the decoy KaiA binds with equal strength to the KaiC-KaiB complex this amounts to a direct modification of m, where m is modulated by $1/\left(1 + dA^T/A^T\right)$. Figure 2.10 shows the amplitude and the period of the oscillation as a function of dKaiA concentration. For differing binding rates it is not as simple but Fig 17b,c (appendix A) shows that this behavior is not contingent on having equal binding rates. This suggests that the relaxation oscillator type of positive feedback present in the original monomer model is still operating in the same qualitative way. The same amount of KaiA must be sequesered to trigger the positive feedback on the S phosphorylation and is simply sequestered more slowly in the presence of dKaiA, causing the period to increase. This shows that these two models with opposing feedback properties can be distinguished by the introduction of a competitor for the KaiA sequestration site.

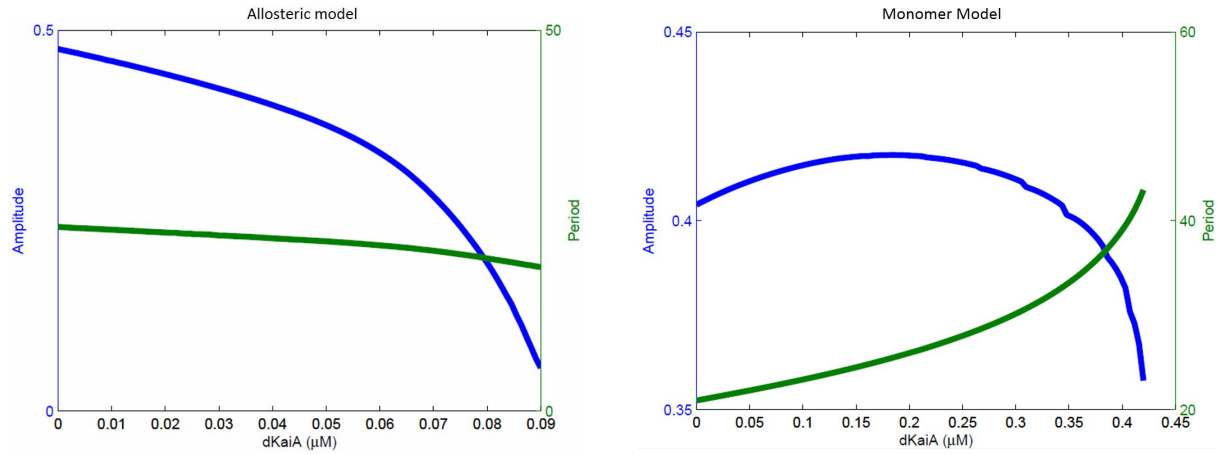

(a) (b)

Figure 2.10: a) The period and amplitude of the allosteric model with the KaiA sequestration stoichiometry set to 2, but including some concentration of a decoy KaiA (dKaiA) which is sequestered competitively with KaiA but does not bind to KaiC otherwise (for example to promote KaiC autophosphorylation). This has qualitatively the same effect on the amplitude and period as changing m directly does. Since increasing m and increasing the concentration of the decoy should have opposite effects on the amount of KaiA bound, this figure shows the same qualitative behavior as Fig. 8B. b) Amplitude and period for the original monomer model with dKaiA. Since the decoy KaiA is sequestered with the same affinity as KaiA,m is simply modulated from its default value of 2 by a factor of $1/\left(1+\frac{dKaiA_T}{KaiA_T}\right)$, and is formally equivalent to changing m directly.

Additionally, the effect of such a competitor can be arrived at by modulating the effective KaiA sequestration stoichiometry m. We will now observe the effects of doing so on a more complex model, the previously introduced two-domain allosteric model.

2.3.5 Two-site allosteric model reproduces result of allosteric model

While the allosteric and monomer models are useful for analyzing the system by the virtue of their dynamics being transparent, it is valuable to understand how the results manifest in the more biologically realistic two-site allosteric model.

To simulate the effect of a competitor species, which competes with KaiA for free binding sites on the N-terminal domain of KaiC, we explicitly introduce a new protein in the two-site allosteric model which we assume to be dKaiA. Because the model tracks a discrete number of proteins, we cannot continuously decrease the sequestration capacity m of a hexamer to simulate the effect of dKaiA, as is done in the other two models. In this model, the N-

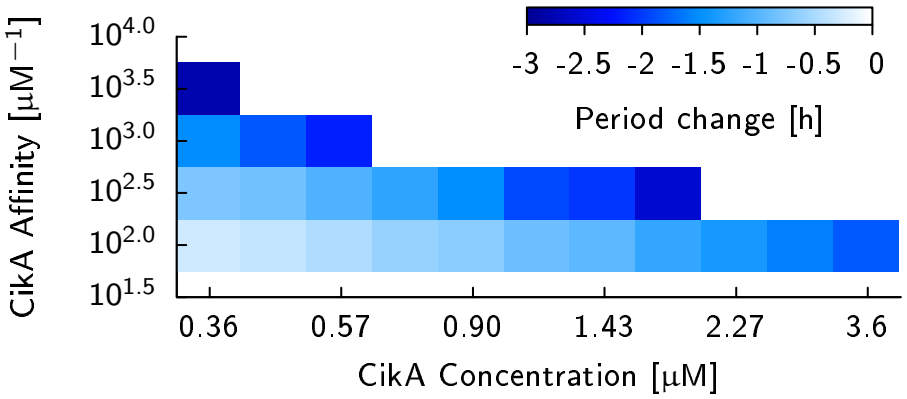

Figure 2.11: Heat plot showing the change in the period for the two site allosteric model as a function of the initial dKaiA concentration and the affinity of dKaiA for KaiB bound to KaiC. Note that both axes are log scale. When the dKaiA affinity is significantly lower than the KaiA affinity, which is the case for the values shown, dKaiA decreases the period of the oscillation. Parameter values corresponding to the area in white show no oscillations.

terminal domain of a hexamer can maximally sequester six dKaiA proteins. dKaiA can only be sequestered from solution when six KaiB monomers are bound to the N-terminal domain of KaiC. Just like the binding of KaiA on N-terminal in this model, dKaiA does not bind cooperatively.

In figure 2.11 we show the heat plot of the change in the period of the phosphorylation level as a function of the dKaiA concentration and the affinity of dKaiA for KaiC. In this plot, we only show results where dKaiA has a low affinity compared to the affinity of KaiA for N-terminal bound KaiB, which is $K_{\text{eq}}^{\text{N·KaiA}} = 107\mu M^{-1}$. Clearly, for all dKaiA concentrations and affinities shown in figure 2.11, the period of the oscillation decreases. Both the dKaiA concentration we use in our simulations and the resulting decrease in period are in good quantitative agreement with the experimental results shown in [26]. Also, when we look at time traces of the phosphorylation level in figure 2.12, it is clear that the troughs of the oscillation move up with increasing initial concentrations of dKaiA. This also agrees well with experiments.

Our simulations show that for the two-site allosteric model, adding a protein that competes with KaiA for the binding sites on the N-terminal domain reduces the period of the oscillator. The period reduces because, by blocking the KaiA binding sites, dKaiA decreases the the time that KaiC can sequester all KaiA from solution. This also explains why the trough of the phosphorylation level increases with the dKaiA level: Due to competition,

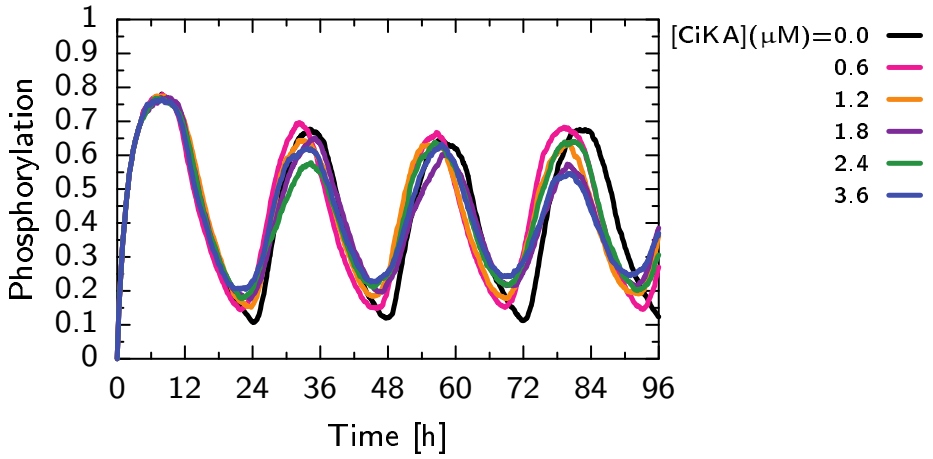

Figure 2.12: Time traces of the phosphorylation level at different concentrations of dKaiA, for the two site allosteric model. The affinity of dKaiA for the N-terminal domain of KaiC is $K_{\mathrm{eq}}^{\mathrm{CI\cdot KaiA}} = 100\mu M$. Consistent with experiments, the period decreases and the troughs of the oscillations move to a higher phosphorylation level with increasing dKaiA concentration.

a single hexamer can on average sequester fewer KaiA dimers. Because there a now more hexamers required to sequester all KaiA, and because these hexamers have a higher phosphorylation level compared to those that have already flipped back to the active state, the trough in the phosphorylation level moves up. The fact that the period decreases shows that, just as we concluded for the allosteric model, the oscillator in the two-site allosteric model behaves as a delay oscillator. Because dKaiA has a much lower affinity than KaiA for the N-terminal domain of KaiC, dKaiA is most effective competing with KaiA for free binding spots when there are only a few KaiA dimers in the solution. This is because the probability that either dKaiA or KaiA will bind to the N-terminal domain is roughly proportional to $dAK_{eq}^{N\cdot dKaiA}$ or $AK_{eq}^{N\cdot KaiA}$, respectively, where $K_{eq}^{N\cdot\circ}$is the dissociation constant of the associated reaction. Given that $K_{eq}^{N\cdot dKaiA} \ll K_{eq}^{N\cdot KaiA}$ in our simulations, dKaiA only has a reasonable chance to bind when the concentration of free KaiA is extremely low. This is only the case when all KaiA is sequestered by KaiC and only one or two KaiA are free in solution due to hexamers flipping back to the active states prematurely. Therefore dKaiA only has an effect at the end of the oscillation and not in the phase when most hexamers are in the active state and there is a lot of free KaiA in solution.

If, as proposed above, the two-site allosteric model can be understood as an example of a negative feedback model, these results are consistent with the simpler allosteric model. This further supports the conjecture that the effect on the period of adding dKaiA to the

oscillator would be a reliable readout of the sign of the feedback present in the system.

2.4 Discussion

We have presented a theoretical and computational study clarifying the differences between two simple types of models of the Kai oscillator. These models, the allosteric model and the monomer model, fall into the distinct classes of delay and relaxation oscillators, respectively, depending on the dynamical effect that KaiA sequestration introduces. These differences cause the period of the oscillator to change in opposing directions when the KaiA sequestration stoichiometry m is reduced. In the allosteric model KaiC hexamers can begin to phosphorylate earlier and the period decreases. In the monomer model, the system needs to wait longer for enough KaiA to be sequestered to reset the balance between phosphorylation and dephosphorylation and both the amplitude and period increase.

The different oscillation mechanisms have heretofore proven to be difficult to unambiguously distinguish experimentally. In the monomer model, positive feedback arises through SKaiC promoting its own production during dephosphorylation, with the rate of SKaiC production increasing as the free KaiA concentration decreases. Thus the essential question is whether free KaiA inhibits the dephosphorylation of KaiC that is competent to sequester KaiA (either inactive hexamers in the monomer model or SKaiC in the monomer model). On one hand, experiments with phosphomimetics indicated that KaiC with the serine residue phosphorylated (the form competent to bind KaiB and sequester KaiA) phosphorylates only very slowly on the T residue in the presence of free KaiA. [29, 132]. Similar experiments [132] suggest that dephosphorylation is independent of the action of KaiA and KaiB. These results imply that KaiA sequestration does not promote the creation of further species that sequester KaiA to a meaningful degree, that is, that KaiA sequestration does not strongly feed back positively on itself. This is consistent with the dynamics of the allosteric model, which also assumes that phosphorylation of KaiB-bound KaiC is not strong and that KaiA does not affect dephosphorylation rates. On the other hand, a study of the individual phosphostate time traces in the native protein showed that the dynamics could be fit very well using the monomer model, which includes a strong positive feedback loop [158].

Investigating the effects of competitive binding on these models has revealed robust, experimentally distinguishable behaviors. We showed that these behaviors can be distinguished by introducing a protein external to the oscillator that competes with KaiA for binding. This method has received little attention as a tool for systematically modulating parameters that

would otherwise be inaccessible, but it effectively probes for both the models and the in vitro oscillator, allowing modeling to directly augment the interpretation of experimental results. A strong candidate protein for such an assay is CikA, which is a known element of the clock output mechanism and binds to the KaiBC complex. Adding CikA to the in vitro system has been shown to decrease the amplitude and period [26]. CikA has also been shown to bind to the KaiA sequestration binding site [178]. This strongly suggests that the dynamics of the in vitro oscillator are primarily those of a delay oscillator.

Although descriptions based on KaiA sequestration have recently predominated, it is worth noting that there are also models of the Kai system whose operation cannot be mapped onto the two types of model considered here in an obvious way. One approach [85, 127] has been to focus on the possibility that exchange of monomers between hexamers, as an alternative to KaiA sequestration, is the primary mechanism of synchronizing the oscillations of individual hexamers. We have not considered these models here because we are focusing on the mechanism of KaiA sequestration.

This focus on modeling KaiA sequestration proved to be a useful starting point for revealing crucial mechanistic details about the system. By comparing two simple but qualitatively distinct numerical models of the oscillator it was possible to understand current experimental results in a new light, helping to contextualize relatively subtle differences that would have been difficult to interpret otherwise. We showed that perturbing the system by introducing a competitor for an important binding site, when compared to numerical results, identifies the type of feedback present in the in vitro system.

The identification of the Kai oscillator as one driven primarily by negative feedback with a delay (of a qualitatively different variety from that described in [90]) is itself a notable result. Understanding the dynamics of oscillators found in biological systems can provide information about why certain oscillator structures might be selected for, and it has been proposed [51] that positive feedback architectures provide certain robustness advantages. In the case of the Kai system it is possible that the large number of states in the oscillator mitigate these difficulties, suggesting a potential parameter regime in which negative feedback oscillators could preferentially be found in biological systems.

Chapter 3

Limitations on Precision in Mechanical Feedback Models

3.1 Introduction

Throughout development organs grow and must stop at appropriate sizes. How the cessation of growth is regulated to produce appropriate final sizes is a vital question in developmental biology, and understanding the details of the regulatory processes that govern it is necessary to address questions of how the usual growth plan breaks down, for example in the case of cancer. To begin to answer this question it is valuable to observe that dramatic variations in organ size between individuals in a species is rare, and bilateral symmetry on an individual basis can result in even smaller variations is size between two organs on the same individual. Such tightly controlled variation suggests that the regulation of organ growth should be precise. However, determining the precision of the mechanisms of size control is difficult.

In this work we compare different families of growth control models and make experimental predictions that distinguish their behavior. To do this we have developed an analytic framework capable of representing generic models of growth control by mechanical feedback. We use this framework to derive the fixed point conditions for these families of models and determine whether or not they predict a unique final size. Additionally, we describe biologically relelvant observables such as uniformity of growth rate and amount of apoptosis.

There is a long history of support for the idea that organ size control is substantially regulated organ-autonomously. From early experiments on salamanders to more recent work on rats (reviewed in [24]), it appears that organ transplants often growt to sizes comparable to those of the donor organism. Particularly striking are the results of experiments on the

Drosophila wing imaginal disk, in which the disk is dissected from the larva and cultured in the abdomen of an adult. One finds that when disks grown in the abdomen of the adult is extracted it has grown and stopped at a final size close to the final size of the wing imaginal disk on the larva [23, 65]. However, the precision of the target size is likely to be sharper than that described in the dissection experiments, since estimates of the variation in sizes between left and right wings on the same fly to be on the order of 1% [19].

Various models for how the growth of the *Drosophila* wing disk is controlled have been proposed. Although there are numerous morphogen distributions that must certainly play a role regulating the growth of the disk, the growth in the wing disk is uniform [115] while these morphogens have some nontrivial gradient. It is also not as simple as reading out the gradient of these distributions, since uniform expression of Dpp, a key morphogen, causes overgrowth [130].

One proposed growth control mechanism consistent with uniform growth in response to nonuniform morphogen distributions is feedback from local mechanical stresses [166]. The mechanical feedback model relies on the tendency of nonuniform growth to generate stresses. If growth is nonuniform, for example if a circular tissue grows more in the center than in the periphery, stresses will build up. Since the material elements in the center are constrained by the material elements in the periphery, their actual area is much smaller than their preferred area, whereas the inverse is true for the elements in the periphery. In a mechanical feedback model, if some localized section of the tissue overgrows, as in the center of such a disk, the local pressure that is produced will downregulate its growth rate in response. Recently there has been growing support for this mechanism in the *Drosophila* wing disk. Direct experiments on dissected disks have shown that mechanical strain increases the cell division rate [162]. Direct genetic modification of the putative mechanical feedback signaling pathway has been also been shown to interfere with uniformity of growth *in vivo* [139].

Mechanical feedback has also been identified in other organisms. In MDCK cells (Madin-Darby canine kidney cells, a well studied epithelian cell line) contact inhibition of growth, the phenomenon of growth in an epithelium slowing upon confluence, has been explained by mechanical feedback models [148]. In addition, the Piezo family of proteins is an evolutionarily conserved family of channel proteins implicated in mechanotransduction in *Drosophila*, zebrafish and mice [118].

In this work we will focus on the *Drosophila* wing disk and will compare the qualitative features of the models studied to the biological details of growth in the wing disk. There have been several [1, 2, 76] efforts to model mechanical feedback of growth control in this

system using numerical models. These are cell-vertex models [50], a type of numerical model which simulates an entire tissue at the level of individual cells which have elastic properties defined by their geometry. These studies have demonstrated that it is possible for mechanical feedback to cause a tissue such as the wing disk to halt its growth. An issue with these cell-based numerical models is that the fixed point structure is difficult to analyze and the relationship between the details of model structure and the specifics of the model behavior can be obscure.

Here we develop an analytic framework that allows different models of growth control with mechanical feedback to be directly compared and their fixed point structure to be analyzed. We are able to study the long time behavior and fixed point structure of broad families of models and to classify these models based on the predictions they make about the precision and uniqueness of the final size of the wing disk. Since we are focusing on the *Drosophila* wing disk, we emphasize relevant experimental observations such as the uniformity of the growth rate and the absence of spatiotemporal patterning of apoptosis during large portions of development. However, the analytic framework is straightforwardly generalizable to other systems that experience mechanical feedback.

We begin in section 3.2 by introducing a theory of elasticity that incorporates growth of the elastic material and describing the relationship between growth and stress. We introduce linearized elastic equations assuming small deformations and small deviations from uniform growth. We restrict our model to growth of an axially symmetric disk in 2D and introduce our formalism for growth feedback by a growth rate γ for the growth that drives the elastic stresses. This in turn introduces nontrivial dynamics for the total tissue size.

Different choices of model are defined by different choices of γ, which is considered as a power series in the pressure p and its derivatives, taken to low order. We show that high pressure in a central region with high growth must be accompanied by negative pressure in an exterior region with low growth, and thus that negative feedback on pressure operating uniformly throughout the disk causes disks to grow indefinitely. Thus we distinguish models based on how they regulate these regions of negative pressure. We define those models that require some threshold level of morphogen in order for any growth to occur, regardless of the pressure, as AND-type models in analogy with the logical operation. In contrast, we define OR-type models as those that allow the morphogen to trade off with mechanical feedback at all points on the disk. We show that AND-type models which set the growth rate to zero over macroscopic sections of the tissue do not predict unique final sizes, and that OR-type models are capable of precise final sizes.

3.2 Elasticity

Here we define the type of growing tissue that we will study and review the linear theory of elasticity we use to introduce the effects of growth. We describe growth of a two dimensional, initially axially symmetric disk of tissue, which will model the growing wing disk. We introduce isotropic growth represented by a scaling factor η and derive linearized elastic equations about uniform average growth, assuming small local fluctuations from uniform growth and small elastic displacements. We describe the elastic equilibrium in terms of the Cauchy stress σ_{ij}. Then in section 3.2.2 we calculate the pressure in terms of η for problem of axially symmetric growth of the initially axisymmetric disk.

In the main text we will assume the fields (the deformation, morphogen distributions, the dilation field η, the stresses, etc) will be axisymmetrtic except when calculating the linear stability of non-axisymmetric perturbations. The elasticity problem for general anisotropic growth can be found in appendix B.1, and the pressure for non-axysymmetric growth of the initially axisymmetric disk can be found in appendix B.1.3. Although the resulting linearized theory will be similar in form to standard results for linear elasticity with expansion due to nonuniform heating, the limit we are working in allows a uniform, isotropic component of the growth to become very large and take on nontrivial, nonlinear time dynamics which will describe the evolution of the total size of the tissue.

3.2.1 Problem fundamentals

We will now specify the fundamentals of the elastic problem we will be analyzing throughout this work. We will follow the standard elasticity convention of referring to coordinates in the Lagrangian configuration with upper case Roman letters (e.g. X_i for a coordinate vector, or R and Θ for polar Lagrangian coordinates) and coordinates in the Eulerian configuration with lower case Roman letters (e.g. x_i for a coordinate vector, or r and θ for polar Eulerian coordinates). We will take the Lagrangian configuration to be a disk with constant radius R_D. The Eulerian radius of the disk, r_d, then varies with time as required by the coordinate map $x_i(X_i)$. The dynamics controlling the Eulerian configuration will take the form of growth dynamics for the isotropic scaling factor η. Since we will be linearizing around uniform growth we must extract the uniform component of this dilation. To do this we define for any function on the Lagrangian configuration $f(X_i)$ the average $\langle f \rangle$ as follows:

$$\langle f \rangle = \frac{1}{\pi R_D^2} \int_0^{R_D} \int_0^{2\pi} f(R,\Theta) R dR d\Theta \tag{3.1}$$

Growth of this disk is encoded as a scaling factor η. Locally, η descibes how lengths of tissue elements are scaled. If an infinitesimal tissue element at location X_i has sides of length dX before growth, then, if it is not deformed elastically, after growth it will have linear dimensions $\eta(X_i)dX$. We define

$$\bar{\eta} \equiv \langle \eta \rangle \tag{3.2}$$

as the uniform component of the growth, and

$$\tilde{\eta} = \eta - \bar{\eta} \tag{3.3}$$

as the nonuniform component of the growth. Given this uniform component $\bar{\eta}$, we define the total deformation in the Eulerian configuration as a displacement w_i, which will be seen of order $\tilde{\eta}$, on top of a displacement due to uniform growth:

$$x_i(X_i) = \bar{\eta} X_i + w_i \tag{3.4}$$

Here the vector w_i is analogous to the displacement vector u_i in standard linear elasticity, but w_i describes a displacement from a (possibly very large) uniform dilation $\bar{\eta}$. We can then define a linear strain tensor in the usual way:

$$w_{ij} = \frac{1}{2}\left(\partial_i w_j + \partial_j w_i\right) \tag{3.5}$$

Elastic equilibrium can then be expressed as the following modification of the standard formulation of linear elasticity (see appendix B.1.2 for a derivation):

$$0 = \partial_i \sigma_{ij} = \frac{1}{\bar{\eta}} \partial_i \left(\lambda(w_{kk} - 2\tilde{\eta})\delta_{ij} + 2\mu(w_{ij} - \tilde{\eta}\delta_{ij})\right) \tag{3.6}$$

3.2.2 Pressure

We now proceed to calculate the pressure in this linearized elastic theory. Assuming axial symmetry, this reproduces a familiar result from the theory of thermal expansion in linear elastic media [93] and we determine that the radial component of the displacement is given by:

$$w_R(R) = \frac{2(\lambda + \mu)}{R(\lambda + 2\mu)} \int_0^R \tilde{\eta}(R') R' dR' \tag{3.7}$$

for stress-free boundary conditions. From this we can determine the local pressure:

$$p(R) = -\frac{1}{d}\sigma_{ii} = \frac{2\mu(\lambda+\mu)}{\lambda+2\mu}\frac{\tilde{\eta}}{\bar{\eta}} \tag{3.8}$$

So for an axisymmetric system the pressure can be found to be directly proportional to $\tilde{\eta}$, and since $\langle\tilde{\eta}\rangle \equiv 0$ as a result we have the following constraint on the pressure:

$$\langle p\rangle = 0 \tag{3.9}$$

If the disk experiences compression in one area there must be other areas that are under tension.

3.2.3 Disk size

Note that since $\langle\tilde{\eta}\rangle = 0$, we have $w(R_D) = 0$. This means that at the edge of the disk, the total deformation $x_i = \bar{\eta}X_i$ for the axially symmetric problem. Then the Eulerian radius of the grown disk is given by

$$r_d = \bar{\eta}R_D \tag{3.10}$$

In addition, non-axisymmetric contribtions to $\eta(R,\Theta)$ are proportional to $\sin(n\Theta)$ or $\cos(n\Theta)$ and have zero average over the disk. Thus to linear order they do not contribute to the total disk size. Therefore $\bar{\eta}$ gives the total size of the disk and we will use $\bar{\eta}$ and disk size interchangably throughout this work.

3.3 Growth dynamics

Now that we have developed the necessary fundamentals of elastic stresses due to growth we can introduce dynamics for the growth itself. We will restrict ourselves to the study of a 2D disk with an axisymmetric Lagrangian configutation. Growth is assumed to be isotropic and occurs in response to some combination of a distribution of morphogen or growth factor and feedback due to local stress. Growth dynamics take the form of a growth rate for η, which describes how the linear dimensions of a given material element are dilated by local growth. We assume an exponential growth law for η in terms of a growth rate γ:

$$\dot{\eta} = \gamma\eta \tag{3.11}$$

Our choice of a feedback model for growth control amounts to a choice for γ, which can depend on the local pressure, concentrations of morphogens, gradients or other operators acting on these quantities, or any other variables which are believed to play an important role in the regulation of tissue growth. Consistent with our linearized theory in which deviations from uniform growth are small we will in general consider $\gamma(p)$ as a power series in p and its derivatives.

The function γ also serves to determine the fixed point of our dynamics. Some systems, such as tumor spheroids, have homeostatic steady-states with cell growth and apoptosis organized in such a way that the total cell number is constant [66]. In the wing disk spatiotemporal patterns of apoptosis are not generally known to play an important role during the majority of development [116], so we will not consider steady states with non-zero growth. This means that steady states will be defined by the cessation of cell growth throughout the tissue. This condition is equivalent to the following condition for the fixed point pressure distribution p^*:

$$\gamma(p^*) \equiv 0 \tag{3.12}$$

Since the pressure p is a function of the growth field η, $\gamma\left(p(\eta^*)\right)$ defines a fixed point for η^* the growth dynamics as well.

3.3.1 Strong feedback and nondimensionalization

Because the results for the pressure in terms of the growth rely on the nonuniformities in the growth being small compared to the uniform average growth it is necessary that this assumption remains valid throughout the dynamics. With this in mind we note that the pressure is proportional to the nonuniformity in growth: $p \propto \tilde{\eta}/\bar{\eta}$. Thus, if the pressure remains "small" then so will $\tilde{\eta}/\bar{\eta}$ such that the linearity assumptions underlying the elastic equilibrium equations are maintained throughout growth. The magnitude of the pressure can be controlled by making the negative feedback on the pressure "strong". The precise form of the pressure feedback depends on the model, but we consider it here with only proportional negative feedback from pressure additively interacting with some basal growth rate γ_0 to illustrate:

$$\gamma = \gamma_0 - \kappa p = \gamma_0 - \kappa \frac{2\mu(\lambda+\mu)}{\lambda+2\mu}\frac{\tilde{\eta}}{\bar{\eta}} \equiv \gamma_0 - \tilde{\kappa}\frac{\tilde{\eta}}{\bar{\eta}} \tag{3.13}$$

where κ is the feedback strength of the pressure and $\tilde{\kappa}$ is the feedback in terms of η. Since $\tilde{\kappa}$ has the same dimensions as γ_0, we nondimensionalize time using γ_0 as a timescale:

$$t \to \gamma_0 t \tag{3.14}$$

such that the basal growth rate γ_0 is equal to 1, also nondimensionalizing the feedback strength. Then the assumption that feedback is strong takes the following form:

$$\frac{\tilde{\kappa}}{\gamma_0} = \frac{1}{\epsilon} \tag{3.15}$$

where $\epsilon \ll 1$, giving the following form for γ, after nondimensionalizing time:

$$\gamma = 1 - \frac{1}{\epsilon}\frac{\tilde{\eta}}{\bar{\eta}} \tag{3.16}$$

This ensures that $\tilde{\eta}/\bar{\eta} = \mathcal{O}(\epsilon)$ throughout the growth process (assuming it is small to begin with), ensuring that the assumptions underlying the linearized elasticity are maintained. Below, when we consider spatially varying morphogen distributions we will take the value of the growth rate at the center of the disk in the absence of pressure feedback as the growth rate γ_0 setting the time scale.

Since this approximation introduces a timescale tied to negative feedback on the ratio $\tilde{\eta}/\bar{\eta}$ it is natural to look for a separation of timescales between these quantities, with $\tilde{\eta}$ having very fast dynamics and approaching some quasi-steady-state $\tilde{\eta}_{qss}$ and $\bar{\eta}$ evolving on a longer timescale towards the fixed point, decoupled from the evolution of $\tilde{\eta}$. This does not happen in general, and whether or not it is possible depends strongly on the form of γ. To see this we calculate the time derivatives of $\bar{\eta}$ and $\tilde{\eta}$:

$$\begin{aligned} \dot{\bar{\eta}} = \langle \gamma\eta \rangle = \langle \gamma(\bar{\eta} + \tilde{\eta}) \rangle = \bar{\eta}\,\langle\gamma\rangle + \langle \gamma\tilde{\eta}\rangle = \bar{\eta}\left(\langle\gamma\rangle + \left\langle \gamma\frac{\tilde{\eta}}{\bar{\eta}}\right\rangle\right) = \bar{\eta}\,\langle\gamma\rangle\,(1+\mathcal{O}(\epsilon)) \\ \dot{\tilde{\eta}} = \gamma\eta - \langle\gamma\eta\rangle = \bar{\eta}\,(\gamma - \langle\gamma\rangle)\,(1+\mathcal{O}(\epsilon)) \end{aligned} \tag{3.17}$$

If we plug in the choice for γ in equation 3.16 this gives:

$$\dot{\tilde{\eta}} = \bar{\eta}\left(1 - \frac{1}{\epsilon}\frac{\tilde{\eta}}{\bar{\eta}} - \left\langle 1 - \frac{1}{\epsilon}\frac{\tilde{\eta}}{\bar{\eta}}\right\rangle\right) = -\frac{\tilde{\eta}}{\epsilon} \tag{3.18}$$

where the average $\langle\tilde{\eta}/\bar{\eta}\rangle = 0$ by equation 3.9. This clearly describes nonuniformities decaying quickly on timescales proprtional to ϵ^{-1}. The dynamics for $\bar{\eta}$ are then totally decoupled from

those of $\tilde{\eta}$:

$$\dot{\bar{\eta}} = \bar{\eta}\left\langle 1 - \frac{1}{\epsilon}\frac{\tilde{\eta}}{\bar{\eta}}\right\rangle = \bar{\eta} \tag{3.19}$$

This describes a disk that continues to grow uniformly for all time. In order to produce models in which growth eventually halts it will be necessary to introduce nontrivial spatial variation in the basal growth rate. As we will see it is not always possible to decouple the dynamics in this way, but by inspecting equation 3.17 we see that the condition

$$\gamma = \langle\gamma\rangle \tag{3.20}$$

for $\gamma \neq 0$ is both necessary and sufficient to define $\dot{\tilde{\eta}} = 0$ and therefore a quasi-steady state $\tilde{\eta}_{qss}$, and thus to decouple the dynamics of $\bar{\eta}$ and $\tilde{\eta}$. Whether or not this decoupling is possible there places qualitative constraints on the dynamics. Once our model families are defined we will show that the two families that we analyze differ in whether or not such a nontrivial quasi-steady-state exists, and that this has a qualitative impact on the dynamics. Not only is uniformity of growth a meaningful prediction consistent with a current understanding of a large portion of larval wing disk development, but since $\bar{\eta}$ determines the disk size this has implications for how the time it takes for the disk to reach its final size scales with the feedback strength.

We now introduce the two families of models which we will investigate. Each of these describes a different mechanism for halting growth in response to stress. These models are defined by a choice for $\gamma(p)$, and beginning in section 3.4 we examine the extent to which they describe a precise, robust final size for tissues growing under that growth law. To do so we compute the fixed point conditions and perform a linear stability analysis to determine the uniqueness of these fixed points and their stability.

3.3.2 Families of models

We will define the basal growth rate, in the absence of feedback from pressure, as a function $M(r)$. This function describes the spatial distribution of the morphogen but also contains information about all of the other quantities that affect the growth rate independent of the pressure, for example basal rates of apoptosis. We will take positive values of $M(r)$ to promote growth and assume that its effect declines with increasing r. This suggests that there will be more growth in the center of the disk and thus a higher pressure. Because of this, by equation 3.9, there must be some region far from the center with $p < 0$. If there is

negative feedback from pressure this will cause growth to occur in this region, which raises the question of how growth stops at all.

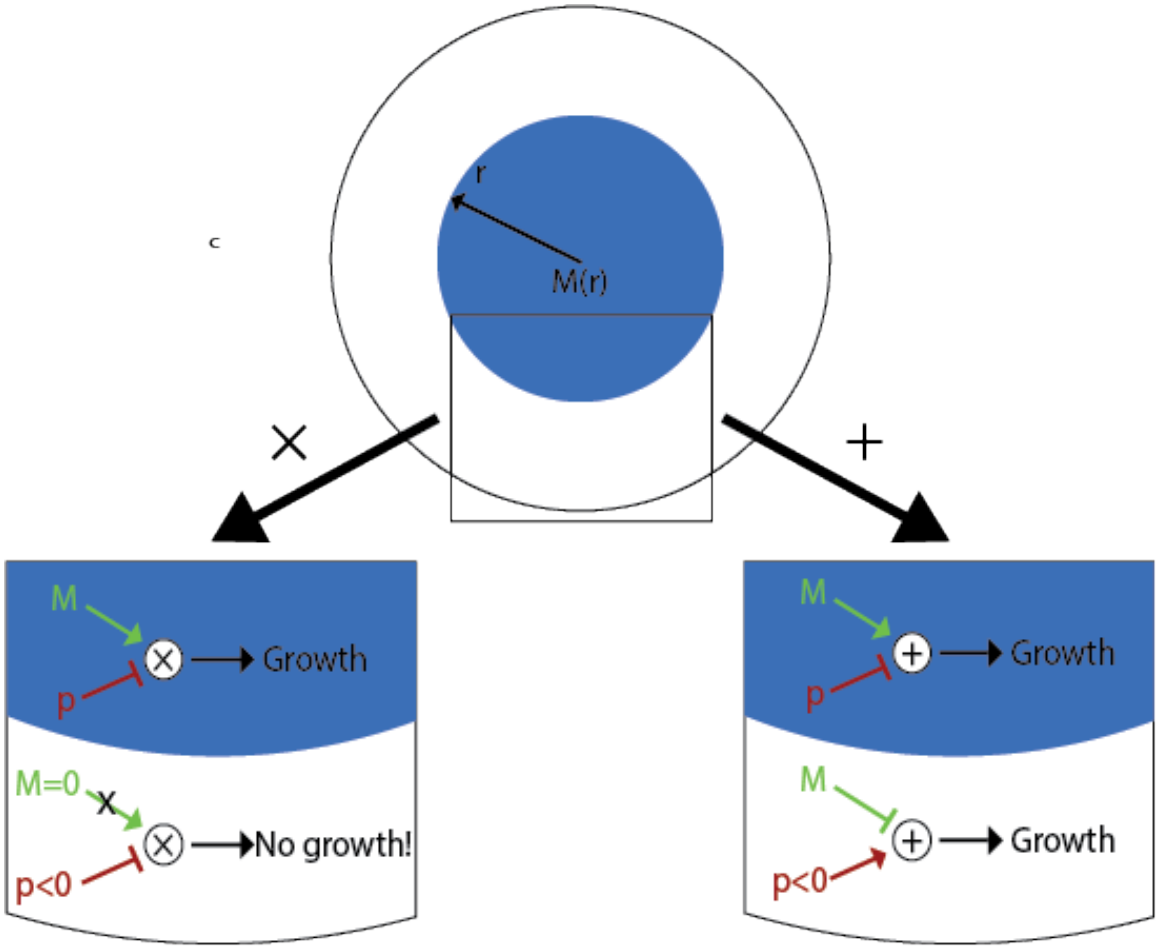

Figure 3.1: The two ways mechanical feedback models can arrest the growth of a disk. Each model represents a choice for how the $M(r)$ affects the pressure feedback at different distances from the center. $M(r)$ is represented (top center) as a step function, with a high value near the center of the disk and a sharp jump at some cutoff radius r_c. (lower left) The AND model requires both feedback from pressure and some threshold level of morphogen for growth to occur at all, in analogy with the logical "AND" operation and is therefore indicated by a "$\times$" symbol. Because of this the growth rate γ is identically zero in the exterior region of the disk, defined by $r > r_c$ (see equation 3.21). As the interior continues to grow, more tissue gets pushed into the region where $\gamma = 0$. Since this exterior region does not grow, as the interior grows it becomes increasingly stressed. Eventually the stress on the interior region from the exterior becomes large enough for the pressure feedback to halt growth in the interior. (lower right) In the OR model growth is allowed to trade off with growth over the entire disk, with growth being driven locally either by pressure feedback or local morphogen concentration, in analogy with the logical "OR" operation and is indicated by a "+" symbol. In order for the disk to stop growing it is necessary for the morphogen concentration to decrease to a level that, in the absence of growth promoted by the negative pressure in the exterior region required by equation 3.9, would cause apoptosis (see equation 3.22). This allows both growth to come to a local fixed point both near and far from the center of the disk, and both regions approach the fixed point simultaneously.

There are two different ways of formulating models that will allow growth to halt in this situation. One is to prevent growth from occurring at all in regions far from the center, including regions where $p < 0$. This is done by requiring some threshold level of morphogen for any growth to occur. We call this the "AND" model, shown schematically in figure 3.1, in analogy with the logical "AND" operation, which requires all inputs to be active in order to produce an active output. The simplest form for $\gamma(p)$ describing an AND model is:

$$\gamma = \Theta(r_c - r)\left(1 - \frac{1}{\epsilon}\frac{\tilde{\eta}}{\bar{\eta}}\right) \tag{3.21}$$

Since there is no growth in the exterior, as the interior continues to grow and more tissue is pushed past the cutoff at r_c, the greater amount of non-growthing tissue in the exterior produces increased pressure on the interior until it eventually reaches the threshold pressure. At this point growth on the interior also ceases and the disk has reached its final size.

Alternately, it is possible to formulate a feedback model in which growth may occur everywhere on the disk and the pressure and the morphogen concentration trade-off to regulate growth locally. In order to cause the growth to halt eventually in the region where $p < 0$, there must be some cutoff distance r_c such that $M(r) < 0$ for $r > r_c$. This model is shown schematically in figure 3.1. The simplest form for $\gamma(p)$ describing and OR model is:

$$\gamma = -\frac{1}{\epsilon}\frac{\tilde{\eta}}{\bar{\eta}} + \Theta(r_c - r) - a \tag{3.22}$$

where $0 < a < 1$. This has the interpretation that there is some basal level of apoptosis in the tissue and that away from the center of the disk the morphogen concentration is too low to prevent it. In these regions the negative pressure promoting growth is necessary for the disk to grow at all.

We will now analyze these different families of models. We describe the fixed points they define for η and do a linear stability analysis to identify the uniqueness and stability of these fixed points. The fixed point structure describes whether or not each of these families of models predict a unique final size for the disk, and under what conditions such a unique final size exists. We first treat the AND model family in section 3.4, and then the OR model in section 3.5.

3.4 AND model

The first model we address is what we will refer to as the "AND" model, since it requires both nonzero growth factor and pressure for growth to occur at all. In this model the growth rate γ depends multiplicatively on a morphogen distribution, with γ vanishing identically when this morphogen is reduced below some threshold. The necessity of some minimal concentration of this morphogen for any growth to occur at all is reminiscent of the logical "AND" operation, inspiring the name.

This model has the virtue of being straightforward and has been propsed by multiple groups in the literature on growth control in *Drosophila* [1, 76]. Its primary characteristic is that growth only occurs within some central region defined by a fixed Eulerian distance r_c from the center (so the region that is growing is constantly shrinking in terms of the Lagrangian coordinates). Growth depends on a basal growth rate, taken to be equal to 1, and negative pressure feedback. As more growth in this region occurs, more tissue is displaced from this central region into the exterior, which exerts a pressure on the interior growing region. The interior region experiences mechanical feedback due to this pressure and its growth rate declines as the pressure approaches a threshold level at which growth ceases. We thus define $\gamma(\eta)$ as follows:

$$\gamma = \Theta(r_c - r)\left(1 - \frac{1}{\epsilon}\frac{\tilde{\eta}}{\bar{\eta}}\right) \tag{3.23}$$

First, we can see that this growth law does not allow uniform growth across the entire disk. Since there is always a region with $\gamma = 0$, the only time the condition $\gamma = \langle\gamma\rangle$ is satisfied is when $\gamma = 0$ everywhere, i.e. when growth is completed. However, this does not necessarily mean that large nonuniformities in growth are expected over large section of the disk. In fact, in the limit of strong feedback the majority of the disk will be uniform with a small fringe region that contains all of the nonuniformities. Additionally, since there is no nontrivial, uniform γ the dynamics of $\bar{\eta}$ and $\tilde{\eta}$ cannot be decoupled. This suggests that there is some intrinsic connection tying the evolution of $\tilde{\eta}$ to those of $\bar{\eta}$.

To understand this we analyze the dynamics. Due to the simplicity of this model we can perform a dimensionality reduction and analyze its dynamics in the phase plane to get a better understanding of how $\tilde{\eta}$ and $\bar{\eta}$ are connected. Since the region $r > r_c$ has no dynamics, the only component of $\tilde{\eta}$ that contributes to the time evolution of the tissue is that within r_c. If this region is uniform at the onset of growth it will remain uniform throughout growth. Thus the dynamics are reduced to two numbers: $\bar{\eta}$, the average of η over the whole disk, and

$\tilde{\eta}_{\text{in}}$, the deviation away from uniform growth on the interior of the disk. Combined with the condition that $\langle\tilde{\eta}\rangle = 0$, these two numbers contain all of the information about the pressure that contributes to the dynamics. Their dynamics are described as follows:

$$\begin{aligned}\dot{\bar{\eta}} &= \langle\gamma\eta\rangle = \bar{\eta}\,\langle\gamma\rangle\,(1+\mathcal{O}(\epsilon)) \\ &= \bar{\eta}\left(1-\frac{1}{\epsilon}\frac{\tilde{\eta}_{\text{in}}}{\bar{\eta}}\right)\langle\Theta(r_c-r)\rangle = \frac{1}{\bar{\eta}}\left(1-\frac{1}{\epsilon}\frac{\tilde{\eta}_{\text{in}}}{\bar{\eta}}\right)(1+\mathcal{O}(\epsilon))\end{aligned} \tag{3.24}$$

Without loss of generality, we choose the inital scale of the disk such that at the onset of growth the Lagrangian radius of the disk R_d is equal to r_c. Physically, this means that $\bar{\eta} = 1$ corresponds to the scale of the disk just as totally uniform growth ends and the outer edge of the disk touches the morphogen cutoff for the first time. Prior to this all growth is totally uniform and generates no stress. A consequence of this choice is that the Eulerian radius of the disk $r_d = \bar{\eta}r_c + \mathcal{O}(\epsilon)$, thus that $\langle\Theta(r_c - r)\rangle = 1/\bar{\eta}^2$. We can then calculate the time derivative of $\tilde{\eta}_{\text{in}}$:

$$\dot{\tilde{\eta}}_{\text{in}} = \bar{\eta}\,(\gamma - \langle\gamma\rangle) = \bar{\eta}\left(1-\frac{1}{\epsilon}\frac{\tilde{\eta}_{\text{in}}}{\bar{\eta}}\right)\left(1-\frac{1}{\bar{\eta}^2}\right) \tag{3.25}$$

From this we can see that, except for a prefactor depending on $\bar{\eta}$, the expressions for $\dot{\tilde{\eta}}_{\text{in}}$ and $\dot{\bar{\eta}}$ have an identical form. In particular, the feedback term which defines the fixed point condition, is the same. This means that both $\bar{\eta}$ and $\tilde{\eta}_{\text{in}}$ have identical fixed point conditions, or that for this phase-plane system there is no unique fixed point, but rather a line of fixed points described by the relation:

$$\epsilon = \frac{\tilde{\eta}_{in}}{\bar{\eta}} \tag{3.26}$$

So the AND model does not describe a unique final size for the wing disk. Essentially, the dynamics encode an initial relaxation of $\tilde{\eta}$ to a steady state $\gamma = \langle\gamma\rangle = 0$. We can see directly that the final disk size, scales lienarly with ϵ (see appendix B.3). Thus, in the strong feedback limit, the extent of the nonuniformity is restricted to a narrow band on the exterior of the disk, with the width of this band scaling as $\sqrt{\epsilon}$ (see appendix B.3).

3.4.1 Robustness

Although the fixed point is not unique, the question of how this would manifest itself experimentally is still meaningful. For example, we can consider a transient change in the inverse feedback strength ϵ (which could arise as either from chemical signaling or a change in the

elastic constants in the material). This would change the fixed point, and thus the final size. However, when the perturbation ended and the original values were restored the disk would relax back to the original final size. To see this we note that neither of these coefficients is present when computing the integral curves of this phase-plane system $\partial\bar{\eta}/\partial\tilde{\eta}_{\text{in}} = \dot{\bar{\eta}}/\dot{\tilde{\eta}}$. Thus when ϵ is changed in a transient manner the phase-plane system remains on the same integral curve, tracking the intersection of the curve with the line $\epsilon\bar{\eta}^* = \tilde{\eta}^*_{\text{in}}$.

It has been suggested [30] that some mechanical feedback models are likely to predict overgrowth in response to tissue damage, in particular if, as in the case of the AND model, the cessation of growth is caused by the constriction of some central region by an exterior region. If this exterior region is damaged, it deforms itself into a lower stress state, decreasing the pressure in the interior. As the pressure on the interior decreases below the growth suppression threshold growth can begin again in the center until pressure builds up to the threshold again, at which point the tissue will have reached a different final size. We can observe this process numerically by simulating the 2D ODE describing the dynamics of $\bar{\eta}$ and $\tilde{\eta}_{\text{in}}$, shown in Fig. 3.2.

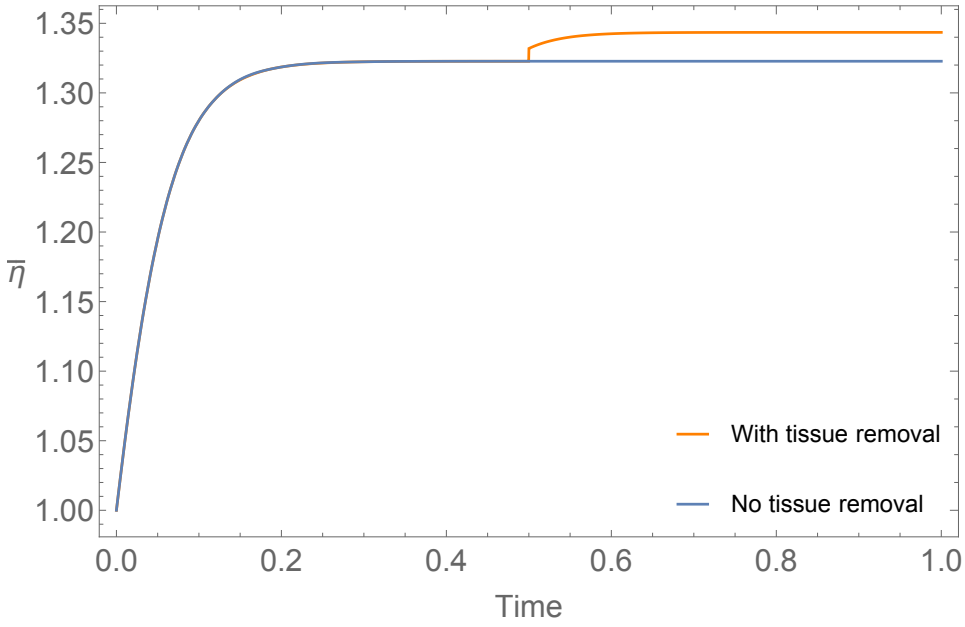

Figure 3.2: Two simulations of the ODE for the reduced system described in equations 3.24 & 3.25, with $\bar{\eta}$ describing the current size of the disk. Usual evolution to the fixed point in blue. Evolution after disk damage in orange. For disk damage simulation, at normalized time $t = 0.5$, an annulus with 5% of the total radius of the disk was removed from the edge of the disk. The orange curve grows to a larger final size

Such a perturbation does not change the local value of η itself, but it changes the area

over which it is averaged to calculate $\bar{\eta}$. This changes the relationship between $\bar{\eta}$ and $\tilde{\eta}$, in this case increasing the average $\bar{\eta}$ and decreasing the deviation from the average on the interior $\tilde{\eta}_{\text{in}}$, since the section that was removed had the lowest value for η. Since during normal evolution both the pressure and the disk size increase together, a perturbation that causes $\bar{\eta}$ to increase and $\tilde{\eta}_{\text{in}}$ to decrease causes the system to move to a different integral curve, resulting in the disk relaxing to a different final size. This new final size will again be robust to transient changes in the feedback parameters.

That the AND model not predicting a unique final size is perhaps not surprising. The fixed point condition $\gamma = 0$ does not define a unique configuration for the pressure, and thus for η, indicating some non-uniqueness. The key point is that the growth dynamics do not depend on the configuration of the disk outside the cutoff r_c, so the only way they affect the dynamics are through the pressure they exert on the interior. It is possible for both large disks that have been deformed relatively little or small disks that have experienced larger deformations to exert the same pressure on the interior, and thus are equally valid final sizes for the disk under the AND model.

3.4.2 Linear stability

To understand this in more detail we will study the linear stability of this system to small perturbations $\delta\eta$ to the steady state η^*. That is, we will be solving the eigenvalue problem:

$$\delta\dot{\eta} = \lambda\delta\eta = (\gamma^* + \delta\gamma)(\eta^* + \delta\eta) = \delta\gamma\eta^* \tag{3.27}$$

Assuming that the perturbations $\delta\eta$ are small and that $\gamma^* = \dot{\eta}^* = 0$. We then take $\gamma = 0 + \delta\gamma$ to first order in $\delta\eta$:

$$\delta\gamma = \Theta(r_c - r)\left(-\frac{1}{\epsilon}\right)\left(\frac{\delta\tilde{\eta}}{\bar{\eta}^*} - \delta\bar{\eta}\frac{\tilde{\eta}^*}{\bar{\eta}^{*2}}\right) \tag{3.28}$$

Note that there is no contribution to $\delta\gamma$ proportional to the derivative of the $\Theta(r_c - r)$ term, even though r depends on $\delta\eta$ since it would be proportional to $\gamma(\eta^*) = 0$. We then examine the eigenvalue equation in detail:

$$\begin{aligned}\lambda\delta\eta &= \Theta(r_c - r)\left(-\frac{\bar{\eta}^*}{\epsilon}\right)\left(\frac{\delta\tilde{\eta}}{\bar{\eta}^*} - \delta\bar{\eta}\frac{\tilde{\eta}^*}{\bar{\eta}^{*2}}\right) + \mathcal{O}(\epsilon) \\ &= \Theta(r_c - r)\left(1 - \frac{1}{\epsilon}\frac{\delta\tilde{\eta}}{\delta\bar{\eta}}\right)\delta\bar{\eta}\end{aligned} \tag{3.29}$$

Where we have used the identity $\tilde{\eta}^*/\bar{\eta}^* = \epsilon$ in the second line. We can see that since $\delta\gamma = 0$ for $r > r_c$, either $\delta\eta = 0$ or $\lambda = 0$. Thus any eigenmodes that are nonzero in the exterior have $\lambda = 0$ and are soft. Additionally, $\delta\tilde{\eta} = \epsilon\delta\bar{\eta}$ is a $\lambda = 0$ mode, consistent with the degeneracy of the fixed point in the reduced ODE model. To understand the $\lambda \neq 0$ modes we will transform $\delta\tilde{\eta} = \delta\eta - \delta\bar{\eta}$ since $\delta\eta = 0$ for $r > r_c$, simplifying the analysis. We can then consider the eigenvalue problem for $r < r_c$:

$$\begin{aligned}
\lambda\delta\eta &= -\frac{1}{\epsilon}\left(\delta\eta - \delta\bar{\eta}\frac{\eta^*}{\bar{\eta}^{*2}}\right) \\
\delta\eta\left(\lambda\epsilon + 1\right) &= \delta\bar{\eta}\frac{\eta^*}{\bar{\eta}} \\
\frac{\delta\eta}{\delta\bar{\eta}} &= \frac{1}{\epsilon}\frac{1+\epsilon}{\lambda\epsilon+1} \\
\left\langle\frac{\delta\eta}{\delta\bar{\eta}}\right\rangle = 1 &= \frac{1}{\bar{\eta}^{*2}}\frac{1+\epsilon}{\lambda\epsilon+1} \\
\lambda &= \frac{1}{\epsilon}\left(\frac{1}{\bar{\eta}^{*2}} - 1\right)
\end{aligned} \tag{3.30}$$

where in the fourth line we have taken an average over the disk, with the average of $\Theta(r_c - r)$ contributing the factor of $1/\bar{\eta}^{*2}$ as before. Then since $\bar{\eta}^* > 1$ we have $\lambda < 0$. Thus the modes that do not have $\lambda = 0$ are stable.

We then study non-axisymmetric perturbations. We define

$$\frac{\delta\tilde{\eta}}{\bar{\eta}^*} = \sum_{n=0}^{\infty} \sin(n\theta)\delta\eta_{n,a} + \cos(n\theta)\delta\eta_{n,b} \tag{3.31}$$

as before and note that for $n > 0$ $\delta\eta = \delta\tilde{\eta}$ since these modes are proportional to $\sin(n\theta)$ or $\cos(n\theta)$ and thus average to zero over the disk. Then, from our expression for the correction to the pressure from non-axisymmetric growth we have:

$$\lambda\delta\eta_{n,i} = -\frac{1}{\epsilon}\left(\delta\eta_{n,i} - 2(n+1)\left(\frac{R}{R_D}\right)^n \int_0^{R_D} \delta\eta_{n,i}\left(\frac{R'}{R_D}\right)^{n+1}\frac{dR'}{R_D}\right)\Theta(r_c - r) \tag{3.32}$$

Again, all modes with $\delta\eta_{n,i} \neq 0$ for $r > r_c$ have $\lambda = 0$ (this includes the necessary zero modes from compatible growth, see appendix B.1.4). To find $\lambda \neq 0$ modes we require that $\delta\eta_{n,i} = 0$ for $r > r_c$. This requires that $\delta\eta \propto R^n\Theta(r_c - r)$, and the eigenvalue problem can be solved

as follows:

$$\begin{aligned} R^n(\epsilon\lambda+1) &= 2(n+1)\left(\frac{R}{R_D}\right)^n \int_0^{R_c} R'^n \left(\frac{R'}{R_D}\right)^{n+1} \frac{dR'}{R_D} \\ \epsilon\lambda+1 &= 2(n+1)R_D^{-2(n+1)} \int_0^{R_c} R'^{2n+1} dR' \\ &= \frac{1}{\bar{\eta}^{*2(n+1)}} \\ \lambda &= \frac{1}{\epsilon}\left(\frac{1}{\bar{\eta}^{*2(n+1)}} - 1\right) < 0 \end{aligned} \tag{3.33}$$

So again all modes with $\lambda \neq 0$ are stable. In this linear stability analysis we have reproduced the soft mode seen in the reduced model, as well as identifying modifications to the exterior where no growth occurs as being key in producing soft modes. This implies that for a mechanical feedback model to predict a unique final size it is necessary for it to define a fixed point pressure everywhere in the tissue. Since there are areas where the pressure will be negative, the basal growth rate must itself be negative in these regions for growth to stop. Essentially, it is necessary for the growth driven by morphogens and growth driven by pressure feedback to be able to trade off everywhere in the disk.

3.5 OR model

As we observed, the AND model predicts a continuous family of final sizes due to the fixed point condition described by $\gamma = 0$ not constraining the configuration of the material where growth is set to zero by the growth factor concentration. This solved the problem of negative pressure in the exterior region promoting growth by halting the dynamics completely. The OR model allows the exterior region where there is negative pressure to have dynamics by allowing the growth factor to be mildly inhibitory of growth in the regions where negative pressure would be expected. The OR model is a model of such a trade-off mechanism. The simplest form of the OR model is expressed by the following choice for γ:

$$\gamma = -\kappa p + M(r) \tag{3.34}$$

Again, we choose the distribution M to depend on the Eulerian coordinate r. In the axisymmetric case we can express γ in terms of η as follows:

$$\gamma = -\frac{1}{\epsilon}\frac{\tilde{\eta}}{\bar{\eta}} + M(r) \tag{3.35}$$

This choice for γ specifies a fixed point η^* defined by:

$$\frac{\tilde{\eta}^*}{\bar{\eta}^*} = \epsilon M(r^*(R)) \tag{3.36}$$

3.5.1 Separation of scales

The OR model predicts a separation of timescales between $\tilde{\eta}$ and $\bar{\eta}$ and thus predicts uniform growth. To see this we first see that the evolution equations take the following form:

$$\begin{aligned} \dot{\bar{\eta}} &= \bar{\eta}\left(-\frac{1}{\epsilon}\frac{\tilde{\eta}}{\bar{\eta}} + (M - \langle M\rangle)\right) \\ \epsilon\dot{\tilde{\eta}} &= -\tilde{\eta} + \epsilon\bar{\eta}\,(M - \langle M\rangle) \equiv -(\tilde{\eta} - \tilde{\eta}_{qss}) \end{aligned} \tag{3.37}$$

where we have defined

$$\tilde{\eta}_{qss} = \epsilon\bar{\eta}\,(M - \langle M\rangle) \tag{3.38}$$

and we see that deviations from $\tilde{\eta}_{qss}$ decay exponentially quickly in the $\epsilon \ll 1$ limit. This quasi-steady-state does still evolve in time, but very slowly. It can be seen from its definition that $\dot{\tilde{\eta}}_{qss} = \mathcal{O}(\epsilon)$, as opposed to $\mathcal{O}(1)$ or $\mathcal{O}(\epsilon^{-1})$, for $\dot{\bar{\eta}}$ and $\partial_t(\tilde{\eta} - \tilde{\eta}_{qss})$, respectively, as we show below. The time dependence derives from $\bar{\eta}$ directly as well as via the dependence of both $M(r)$ (through $r = \bar{\eta}R + \mathcal{O}(\epsilon)$) and the average over the disk. Effectively, the quasi-steady-state pressure is the locally related to the fixed point pressure by a constant offset determined by $\langle M\rangle$. This constant is necessary since one only has $\langle M\rangle = 0$ at the fixed point disk size $\bar{\eta}^*$. We then determine the final size from the fixed point value $\bar{\eta}^*$. For a simple choice of M this can be calculated directly. We choose $M(r) = \Theta(r_c - r) - a$, where $0 < a < 1$, so that it is positive for $r < r_c$ and negative for $r > r_c$, as previously specified. Then we have:

$$\dot{\bar{\eta}} = \bar{\eta}\,\langle M\rangle = \bar{\eta}\left(\frac{1}{\bar{\eta}^2} - a\right) \tag{3.39}$$

This demonstrates that the strength of the feedback does not affect the average growth rate of the whole tissue, as opposed to the AND model where no nontrivial $\tilde{\eta}_{qss}$ could be found.

Distributions of $\tilde{\eta}_{qss}$ for different values of $\langle M \rangle$ are plotted in figure 3.3. In the OR model the time scale of the evolution of the total tissue size is set only by the morphogen distribution. Then to find the final size of the disk we set $\dot{\bar{\eta}} = 0$ to find

$$\bar{\eta}^* = \frac{1}{\sqrt{a}} \tag{3.40}$$

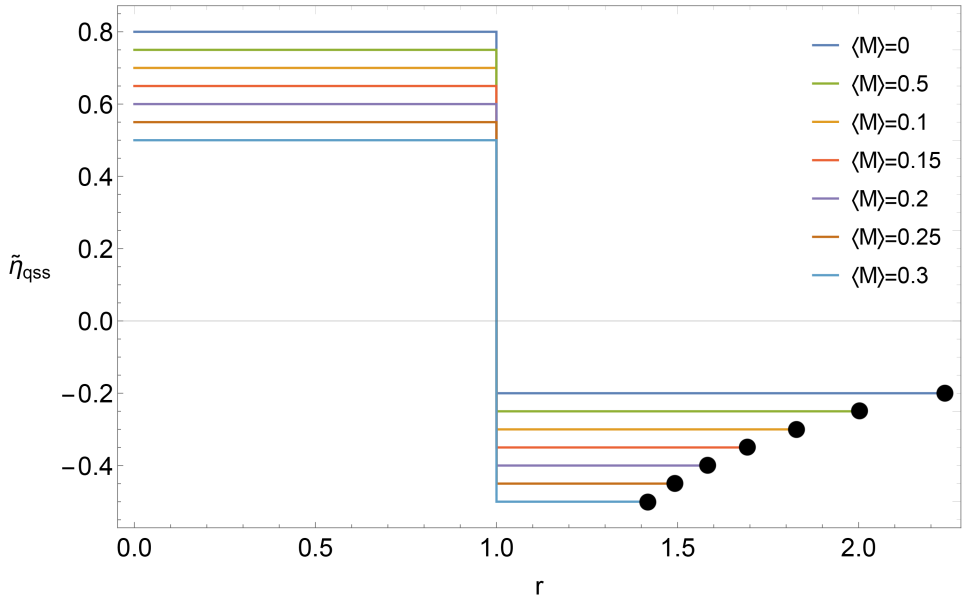

Figure 3.3: The quasi-steady-state distribution $\tilde{\eta}_{qss}$, given in equation 3.38, for different values of $\langle M \rangle$, or equivalently, different times. As the system evolves and $\bar{\eta}$ increases to its fixed point value $\langle M \rangle$ decreases to zero. The disk size for each trace is indicated by a black dot. Traces for larger values of $\langle M \rangle$ end earlier, since they describe a smaller disk size. Since $\langle \tilde{\eta}_{qss} \rangle = 0$, if the disk is smaller then $\tilde{\eta}_{qss}$ must be more strongly negative in the exterior in order to meet this condition. It becomes shallower as the system approaches the fixed point.

3.5.2 Linear stability

To understand the properties of this fixed point in more detail we move to the linear stability problem. We begin as before by calculating the growth rate $\delta\gamma$ corresponding to a small

perturbation to the fixed point:

$$\begin{aligned}\delta\gamma &= -\frac{1}{\epsilon}\left(\frac{\delta\tilde{\eta}}{\bar{\eta}^*} - \delta\bar{\eta}\frac{\tilde{\eta}^*}{\bar{\eta}^{*2}}\right) + \delta r M'(r) \\ &= -\frac{1}{\epsilon}\frac{\delta\tilde{\eta}}{\bar{\eta}^*} + \frac{\delta\bar{\eta}}{\bar{\eta}^*}M(r) + r\frac{\delta\bar{\eta}}{\bar{\eta}^*}M'(r)\end{aligned} \tag{3.41}$$

Where $\delta r = R\delta\bar{\eta} + \mathcal{O}(\epsilon) = r\delta\bar{\eta}/\bar{\eta}^* + \mathcal{O}(\epsilon)$. We then find $\langle\gamma\rangle$:

$$\langle\gamma\rangle = \frac{\delta\bar{\eta}}{\bar{\eta}^*}\langle M + rM'(r)\rangle = \frac{\delta\bar{\eta}}{\bar{\eta}^*}\langle rM'(r)\rangle \tag{3.42}$$

For our choice of $M = \Theta(r_c - r) - a$ these take the form:

$$\begin{aligned}\delta\gamma &= -\frac{1}{\epsilon}\frac{\delta\tilde{\eta}}{\bar{\eta}} + \frac{\delta\bar{\eta}}{\bar{\eta}^*}\left(\Theta(r_c - r^*) - r^*\delta(r_c - r^*)\right) \\ \langle\delta\gamma\rangle &= -\frac{\delta\bar{\eta}}{\bar{\eta}}\langle r\delta(r_c - r^*)\rangle = -\frac{\delta\bar{\eta}}{\bar{\eta}}\frac{2r_c}{r_d^*} = -2a\frac{\delta\bar{\eta}}{\bar{\eta}^*}\end{aligned} \tag{3.43}$$

The full linear stability problem is then again expressed as

$$\lambda\delta\bar{\eta} = \bar{\eta}^*\langle\delta\gamma\rangle, \quad \lambda\delta\tilde{\eta} = (\delta\gamma - \langle\delta\gamma\rangle) \tag{3.44}$$

We can then see that any modes with $\delta\bar{\eta} \neq 0$ have $\lambda = -2a$ and any modes with $\delta\bar{\eta} = 0$ must have $\lambda = -\epsilon^{-1}$. Thus there are no $\lambda = 0$ modes and all modes are stable. In particular we can conclude that the OR model does predict a unique final size as well as uniform growth, suggesting that it may provide the foundation for a description of the behavior of growth control in the wing disk.

3.5.3 Apoptosis

Although the OR model predicts a unique final size and uniform growth it has other difficulties that may prevent it from being an fully accurate description of the qualitative growth dynamics of the wing disk. In particular it is generally understood that apoptosis does not have meaningful spatiotemporal patterning during the majority of wing disk growth [116]. We will demonstrate that the OR model as presented thus far predicts apoptosis patterns for sharp enough gradients in M. Steplike gradients in the relevant morphogen are potentially biologically meaningful if the molecule directly affecting the growth rate is regulated by the key morphogens, such as Dpp, by an ultrasensitive switch. A highly nonlinear activation

response could amplify even shallow gradients in these key morphogens.

Apoptosis could occur if at some point R_0 the local pressure overshoots the local value of the fixed point pressure. This would require negative growth to return to the fixed point when growth ends, which would involve apoposis. Oovergrowth could occur if the local pressure was advected past the local fixed point value, causing apoptosis. A sharp gradient would decrease the time it would take to advect the pressure past the fixed point pressure, so a sharp enough gradient should result in overgrowth. To address this we consider the difference in the time derivatives of the instantaneous pressure and the advected fixed point pressure:

$$\frac{\partial}{\partial t}\left(p(R,t) - p^*(r(R,t))\right) = \dot{p}(R,t) - p^{*\prime}(r(R,t))\frac{\partial r(R,t)}{\partial t} \tag{3.45}$$

We will consider in this case a morphogen distribution that takes the value $M = -m_p$ in the exterior region, and a time t_0 and point $R_0 > R_c(t_0)$ such that $p(R_0,t_0) = p^*(r(R_0,t_0))$ which implies $\gamma(R_0,t_0) = 0$. This gives:

$$\begin{aligned}
\frac{\partial}{\partial t}\left(p(R,t) - p^*(r(R,t))\right) =& -\frac{2\mu(\lambda+\mu)\eta}{\bar{\eta}^2(\lambda+2\mu)}\langle\gamma\eta\rangle \\
&+ m_p\epsilon\left[\langle\gamma\eta\rangle\,\tilde{R} + \frac{2(\lambda+\mu)}{\tilde{R}(\lambda+2\mu)}\int_0^{\tilde{R}}(\gamma\eta - \langle\gamma\eta\rangle)R'dR'\right] \\
=& -\langle\gamma\eta\rangle\,\frac{2\mu(\lambda+\mu)\eta}{\bar{\eta}^2} \\
&+ m_p\epsilon\left[\langle\gamma\eta\rangle\,\tilde{R}\left(1 - \frac{\lambda+\mu}{\lambda+2\mu}\right) + \frac{2(\lambda+\mu)}{\tilde{R}(\lambda+2\mu)}\int_0^{\tilde{R}}\gamma\eta R'dR'\right]
\end{aligned} \tag{3.46}$$

The first term is negative and the second is positive. As m_p becomes large with respect to ϵ^{-1}, the positive term will dominate. Essentially, since the OR model can support arbitrarily large gradients in steady state, there exist gradients large enough that the advection due to growth causes the tissue to overgrow past its steady state value. This overgrowth will then lead to spatiotemporally localized patterns of apoptosis as the system approaches its fixed point, which is unknown during the majority of development [116]. Such apoptosis could be avoided if the fixed point distribution could have a gradient set independently of the gradient of the morphogen. This suggests that this difficulty could be avoided by introducing feedback on the gradient of the pressure, which would cause the steady-state pressure to be smoother and potentially prevent overgrowth.

3.6 Gradient OR model

In order to address the prediction of patterns of apoptosis we introduce the gradient OR model. With feedback on the gradient of the pressure sharp changes in pressure promote growth. The resulting pressure distributions then become much smoother than they would be for the model with only proportional feedback. Here we show that the crucial properties of the OR model, such as uniform growth and a unique final size, carry over to a model with additional gradient feedback. For the gradient OR model γ takes the following form:

$$\gamma = -\kappa(p + c(r)p'(r)) + M(r) \tag{3.47}$$

We require the gradient be taken with respect to the Eulerian coordinate r, as the tissue would not be able to directly measure the gradient with respect to the Lagrangian coordinate R. Such a term could appear in the growth rate γ as the dot product of the gradient of the pressure and an auxiliary morphogen $M_2(r)$, decreasing monotonically with r, giving the term $\nabla M_2 \cdot \nabla p$, which has the appropriate symmetry and sign. We take $c(r) = c\Theta(r - r_c)$ following [2] corresponding to spatial pattern of the regulation of the membrane proteins Ds and Fj, proteins hypothesized to introduce gradient feedback [2], by key morphogens and their effect on growth. Then in the axisymmetric case we have:

$$\gamma = -\frac{1}{\epsilon}\frac{\tilde{\eta}}{\bar{\eta}} - \frac{c\Theta(r - r_c)}{\epsilon}\frac{\tilde{\eta}'}{\bar{\eta}} + M(r) \tag{3.48}$$

Now the steady state condition $\gamma(\eta) = 0$ is a differential equation and therefore requires a boundary condition to produce a unique solution. The steplike activity of the gradient feedback, combined with the condition that γ not diverge anywhere on the disk, will provide this boundary condition as follows. Take a small region of width 2δ around r_c and consider

the limit in which $\delta \to 0$:

$$\begin{aligned}
0 &= \lim_{\delta\to 0} \int_{r_c-\delta}^{r_c+\delta} \gamma(R) dR \\
&= \lim_{\delta\to 0} \int_{r_c-\delta}^{r_c+\delta} -\frac{1}{\epsilon}\frac{\tilde{\eta}}{\bar{\eta}} - \frac{c\Theta(r(R)-r_c)}{\epsilon}\frac{\tilde{\eta}'}{\bar{\eta}} + M(r(R)) dR \\
&= -\lim_{\delta\to 0} \int_{r_c-\delta}^{r_c+\delta} \frac{c\Theta(r(R)-r_c)}{\epsilon}\frac{\tilde{\eta}'}{\bar{\eta}} dR \\
&= -c\lim_{\delta\to 0} \left[\Theta(r(R)-r_c)\tilde{\eta}(R)\Big|_{r_c-\delta}^{r_c+\delta} - \int_{r_c-\delta}^{r_c+\delta} \delta(r-r_c)\tilde{\eta}(R) \right] \\
&= -c\lim_{\delta\to 0} \left[\Theta(r(R)-r_c)\tilde{\eta}(R)\Big|_{r_c-\delta}^{r_c+\delta} - \frac{1}{2}\left(\tilde{\eta}(r_c+\delta) + \tilde{\eta}(r_c-\delta)\right) \right] \\
&= -c\lim_{\delta\to 0} \left(\tilde{\eta}(r_c+\delta) - \tilde{\eta}(r_c-\delta)\right)
\end{aligned} \tag{3.49}$$

so we can see that $\tilde{\eta}$ must be continuous at r_c, providing the boundary condition necessary for the ODE describing the fixed point condition to have a unique solution.

3.6.1 Separation of scales

Next we observe that the separation of timescales proceeds in the same manner as before. Again, we choose $0 = \epsilon\bar{\eta}\left[\gamma(\tilde{\eta}_{qss}) - \langle\gamma(\tilde{\eta}_{qss})\rangle\right]$. For the gradient model and our previous choice of morphogen distribution $M(r) = \Theta(r_c - r) - a$ this gives:

$$\begin{aligned}
&-\frac{1}{\epsilon}\frac{\tilde{\eta}_{qss}}{\bar{\eta}} - \frac{c\Theta(r-r_c)}{\epsilon}\frac{\tilde{\eta}'_{qss}}{\bar{\eta}} + M = \left\langle -\frac{c\Theta(r-r_c)}{\epsilon}\frac{\tilde{\eta}'_{qss}}{\bar{\eta}} + M \right\rangle \\
&\implies \tilde{\eta}_{qss} = \begin{cases} \langle c\Theta(r-r_c)\tilde{\eta}_{qss}\rangle + \bar{\eta}\epsilon\left(1 - \frac{1}{\bar{\eta}^2}\right) & r < r_c \\ \langle c\Theta(r-r_c)\tilde{\eta}_{qss}\rangle - \frac{\epsilon}{\bar{\eta}} \end{cases}
\end{aligned} \tag{3.50}$$

where the value of $\langle c\Theta(r-r_c)\tilde{\eta}_{qss}\rangle$ is determined self-consistently. Again, this quasi-steady-state has a time derivative that is of order $\mathcal{O}(\epsilon)$, and the same separation of scales is achieved as in the basic OR model. Analytically finding the fixed point size exactly is not possible due to the complexity of the problem. We will instead estimate the final size in the limits

$c \ll r_c$ and $c \gg r_c$. The fixed point condition is as follows:

$$\langle \gamma \rangle = 0 \implies \epsilon \bar{\eta}^* \langle M \rangle = \langle c\Theta(r - r_c)\tilde{\eta}^{*\prime} \rangle \implies \bar{\eta}^{*2} = \frac{1}{a + \left\langle \frac{c\Theta(r-r_c)}{\epsilon} \frac{\tilde{\eta}^{*\prime}}{\bar{\eta}} \right\rangle} \tag{3.51}$$

The $\gamma = 0$ condition gives the fixed point distribution $\tilde{\eta}^*/\bar{\eta}^*$, illustrated in Fig 3.4:

$$\frac{\tilde{\eta}^*}{\bar{\eta}^*} = \begin{cases} \epsilon(1-a) & r < r_c \\ \epsilon\left(e^{\frac{r_c - r}{c}} - a\right) & r > r_c \end{cases} \tag{3.52}$$

and the gradient:

$$\frac{\tilde{\eta}^{*\prime}}{\bar{\eta}^*} = \begin{cases} 0 & r < r_c \\ \frac{\epsilon}{c}\left(e^{\frac{r_c - r}{c}}\right) & r > r_c \end{cases} \tag{3.53}$$

3.6.2 Final size

In calculating the corrections to the final size and the solutions to the eigenvalue problem it will be convient to introduce the dimensionless constants $\tilde{c} = 1/z = c/r_c$. The weak feedback limit then corresponds to an expansion in small $\tilde{c}$ and the strong feedback limit corresponds to small z. We first address the weak feedback limit. In this limit we have:

$$\begin{aligned} \left\langle c\Theta(r - r_c)\frac{\tilde{\eta}^{*\prime}}{\bar{\eta}} \right\rangle &= \frac{2\epsilon\tilde{c}}{\bar{\eta}^{*2}}\left[e^{\frac{1-\bar{\eta}^*}{\tilde{c}}}\left(\frac{\bar{\eta}^*}{\tilde{c}} + 1\right) - \left(\frac{1}{\tilde{c}} + 1\right)\right] \\ &= -2\epsilon\frac{\tilde{c}(1+\tilde{c})}{\bar{\eta}^{*2}} \end{aligned} \tag{3.54}$$

where the exponential term was dropped because it vanishes in the limit $c \to 0$. If we choose $\bar{\eta}^* = \bar{\eta}_0^* + \tilde{c}\bar{\eta}_1^*$ this condition simplifies to:

$$\left\langle c\Theta(r - r_c)\frac{\tilde{\eta}^{*\prime}}{\bar{\eta}} \right\rangle = -2\epsilon\frac{\tilde{c}}{\bar{\eta}_0^{*2}} + \mathcal{O}(\tilde{c}) \tag{3.55}$$

Then by matching terms with the fixed point condition for $\bar{\eta}^*$ we find:

$$\bar{\eta}^* = \frac{1}{\sqrt{a}}(1 + \tilde{c}) + \mathcal{O}(\tilde{c}) \tag{3.56}$$

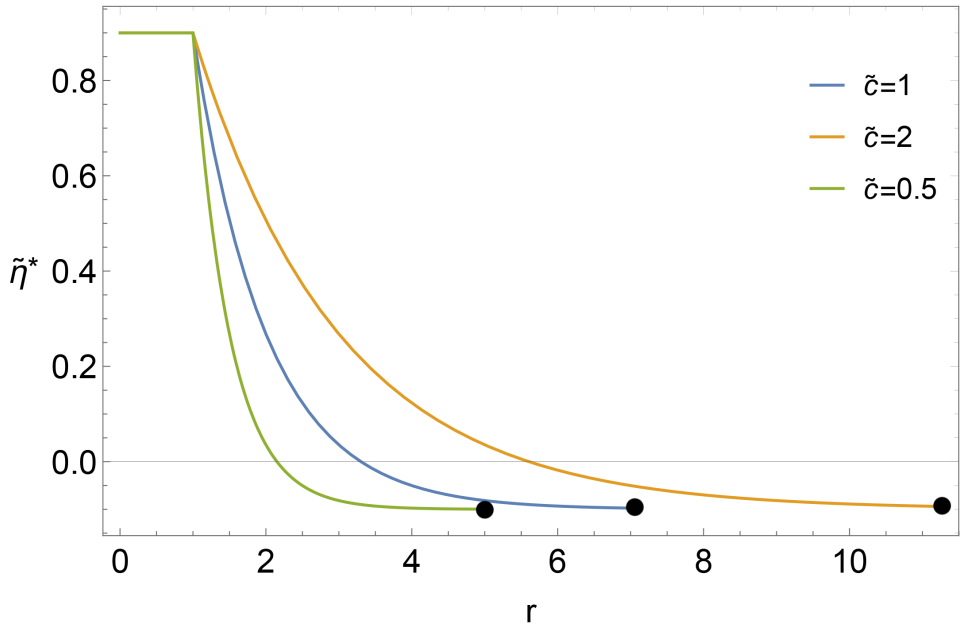

Figure 3.4: The fixed point distributions for the OR model with gradient feedback, plotted for different values of $\tilde{c} = c/r_c$, in units with $r_c = 1$. The size of the disk for each trace is indicated by a black dot. The traces for each distribution end at the final size of the disks they describe, calculated by the condition that $\langle \tilde{\eta}^* \rangle = 0$. If the gradient feedback strength is weak, $\tilde{c} \ll 1$, then the steady state distribution has a sharp gradient and the final size is similar to that of the non-gradient model. For strong gradient feedback with $\tilde{c} \gg 1$, the gradients of the steady-state distribution are much less sharp and the size of the disk is set by the feedback strength rather than the cutoff distance.

We can then take the strong feedback limit, the limit of small z, next. We rearrange the fixed point condition as follows:

$$1 = a\bar{\eta}^{*2} + 2\left[e^{z(1-\bar{\eta}^*)}\left(\frac{\bar{\eta}^*}{z} + \frac{1}{z^2}\right) - \left(\frac{1}{z} + \frac{1}{z^2}\right)\right] \tag{3.57}$$

If $\bar{\eta}^*(z)$ were to diverge faster than z^{-1} as $z \to$, the exponential term could be neglected. In doing so, one finds that $\bar{\eta}^*$ diverges as z^{-1}, indicating that

$$\bar{\eta}^* = \bar{\eta}^*_{-1} z^{-1} + \bar{\eta}^*_0 + \mathcal{O}(z) \tag{3.58}$$

is a consistent expansion. Rearranging, we arrive at the following expression for $\bar{\eta}^*$:

$$0 = a\bar{\eta}^{*2}_{-1} + 2\left[e^{-\bar{\eta}^*_{-1}}\left(\bar{\eta}^*_{-1} + 1\right) - 1\right] + 2z\left[a\bar{\eta}^*_{-1}\bar{\eta}^*_0 + e^{-\bar{\eta}^*_{-1}}\left(1 + \bar{\eta}^*_{-1}(1 - \bar{\eta}^*_0)\right) - 1\right] \tag{3.59}$$

If $\bar{\eta}^*_{-1} > 1$ we may ignore the exponential term. Doing so, we find

$$\bar{\eta}^*_{-1} = \sqrt{\frac{2}{a}} \tag{3.60}$$

so the approximation is consitent. From the higher order term we then find

$$\bar{\eta}^*_{0} = \frac{1}{\sqrt{2a}} \tag{3.61}$$

so that in both limits we have $\bar{\eta}^* \sim \tilde{c}$, so that the disk size is set by the length scale of the gradient feedback. This is consistent with the intuition that gradient feedback will smoothen the spatial distribution of pressure.

3.6.3 Apoptosis

For strong enough gradient feedback this model will not produce apoptosis even for steep gradients in the morphogen. For this model, the gradient of the fixed point pressure (as before, taking the morphogen to be linear with some steep slope $-m_p$) takes the form:

$$p^{*\prime} = -m_p \epsilon \left(1 + (z-1)\, e^{z(1-r/r_c)}\right) \tag{3.62}$$

For large enough $z = r_c/c$ this gradient can be made small enough that the negative term $\dot{p}$ will cause the time derivative

$$\frac{\partial}{\partial t}\left(p(R,t) - p^*(r(R,t))\right) \tag{3.63}$$

to become negative, preventing apoptosis.

3.6.4 Linear stability

In order to fully understand the fixed point structure and uniqueness of the final size for this model we must address the linear stability problem. As before this involves calculating $\delta\gamma$,

initially for the axisymmetric case:

$$\begin{aligned}
\delta\gamma &= -\kappa(\delta p + c(r)\delta p' - \delta r c'(r) p^{*\prime}) + \delta r M' \\
&= -\frac{1}{\epsilon}\left(\frac{\delta\tilde{\eta}}{\bar{\eta}^*} - \delta\bar{\eta}\frac{\tilde{\eta}^*}{\bar{\eta}^{*2}}\right) - r\frac{c'(r^*)}{\epsilon}\frac{\delta\bar{\eta}}{\bar{\eta}^*}p^{*\prime} - \frac{c(r^*)}{\epsilon}\left(\frac{\delta\tilde{\eta}'}{\bar{\eta}^*} - \delta\bar{\eta}\frac{\tilde{\eta}^{*\prime}}{\bar{\eta}^{*2}}\right) + r\frac{\delta\bar{\eta}}{\bar{\eta}^*}M'(r) \\
&= -\frac{1}{\epsilon}\frac{\delta\tilde{\eta}}{\bar{\eta}^*} - \frac{c(r)}{\epsilon}\frac{\delta\tilde{\eta}'}{\bar{\eta}^*} + \frac{\delta\bar{\eta}}{\bar{\eta}^*}\left[\epsilon M + r\left(M' - \frac{c'}{\epsilon}\frac{\tilde{\eta}^{*\prime}}{\bar{\eta}^*}\right)\right]
\end{aligned} \tag{3.64}$$

Since $\delta\gamma$ includes derivatives of step functions there will be discontinuities at r_c. They can be calculated as before:

$$\begin{aligned}
0 &= \lim_{\delta\to 0}\int_{r_c-\delta}^{r_c+\delta}\delta\gamma dr \\
&= \lim_{\delta\to 0}\int_{r_c-\delta}^{r_c+\delta}\left(-\kappa\delta r c'(r^*)p^{*\prime} - \kappa c(r^*)\delta p' + \delta r M'(r^*)\right)dr \\
&= \lim_{\delta\to 0}\int_{r_c-\delta}^{r_c+\delta}\left(-r\kappa c\frac{\delta\bar{\eta}}{\bar{\eta}^*}\delta(r-r_c)p^{*\prime} - \Theta(r-r_c)\kappa c\delta p' - r\frac{\delta\bar{\eta}}{\bar{\eta}^*}\delta(r-r_c)\right)dr \\
&= \lim_{\delta\to 0}\left[-r_c\frac{\delta\bar{\eta}}{\bar{\eta}^*}\left(\kappa c\frac{1}{2}\left(p^{*\prime}(r_c-\delta) + p^{*\prime}(r_c+\delta)\right) + 1\right) - \int_{r_c-\delta}^{r_c+\delta}\Theta(r-r_c)\kappa c\delta p' dr\right] \\
&= \lim_{\delta\to 0}\left[-r_c\frac{\delta\bar{\eta}}{\bar{\eta}^*}\left(\kappa c\frac{1}{2}\left(p^{*\prime}(r_c-\delta) + p^{*\prime}(r_c+\delta)\right) + 1\right) - \kappa c\frac{1}{2}\left(\delta p(r_c+\delta) - \delta p(r_c-\delta)\right)\right] \\
&= \lim_{\delta\to 0}\left[-r_c\frac{\delta\bar{\eta}}{\bar{\eta}^*}\frac{1}{2} - \kappa c\frac{1}{2}\left(\delta p(r_c+\delta) - \delta p(r_c-\delta)\right)\right]
\end{aligned} \tag{3.65}$$

Since $\tilde{\eta}^*$ is continuous this translates into the following jump condition for $\delta\tilde{\eta}$:

$$\lim_{\delta\to 0}\left(\delta\tilde{\eta}(r_c+\delta) - \delta\tilde{\eta}(r_c-\delta)\right) = -\epsilon\delta\bar{\eta}\frac{r_c}{c} \tag{3.66}$$

The eigenvalue problem can then be posed:

$$\lambda\delta\bar{\eta} = \bar{\eta}^*\left\langle\delta\gamma\right\rangle; \quad \lambda\delta\tilde{\eta} = \bar{\eta}^*\left(\delta\gamma - \left\langle\delta\gamma\right\rangle\right) \tag{3.67}$$

with

$$\begin{aligned}\langle\delta\gamma\rangle &= -\frac{\langle c(r)\delta\tilde{\eta}'\rangle}{\epsilon\bar{\eta}} + \frac{\delta\bar{\eta}}{\bar{\eta}^*}\left[\epsilon\left(\frac{1}{\bar{\eta}^{*2}} - a\right) + \left\langle r\left(M'(r) - \frac{c'(r)}{\epsilon}\frac{\tilde{\eta}^{*\prime}}{\bar{\eta}^*}\right)\right\rangle\right] \\ &= -\frac{\langle c(r)\delta\tilde{\eta}'\rangle}{\epsilon\bar{\eta}^*} - \epsilon a\frac{\delta\bar{\eta}}{\bar{\eta}^*}\end{aligned} \tag{3.68}$$

And for $\delta\tilde{\eta}$ we have (assuming $\delta\bar{\eta} \neq 0$):

$$\delta\tilde{\eta} = \begin{cases} \frac{1}{1+\lambda\epsilon}\left(\epsilon\delta\bar{\eta} + \langle c(r)\delta\tilde{\eta}'\rangle\right) & r < r_c \\ \delta\bar{\eta}\epsilon\left(\frac{1}{1+\lambda\epsilon} - \frac{r_c}{c}\right)e^{-\frac{r_c-r}{c}(1+\lambda\epsilon)} + \frac{\langle c(r)\delta\tilde{\eta}'\rangle}{1+\lambda\epsilon} & r > r_c \end{cases} \tag{3.69}$$

where the prefactor for the exponential is determined by the jump condition at r_c as previously calculated. The average $\langle c(r)\delta\tilde{\eta}'\rangle$ can then be calculated. The simplest case is the $\lambda = 0$ problem. In this case the fixed point relation

$$\left\langle\Theta(r - r_c)e^{-\frac{r}{c}}\right\rangle = e^{-\frac{r_c}{c}}\left(a - \frac{1}{\bar{\eta}^{*2}}\right) \tag{3.70}$$

simplifies the problem:

$$\begin{aligned}\lambda\bar{\eta} = 0 &= -\frac{\langle c(r)\delta\tilde{\eta}'\rangle}{\epsilon} - \epsilon a\frac{\delta\bar{\eta}}{\bar{\eta}^*} \\ &= -\delta\bar{\eta}\left[a - \frac{1}{\bar{\eta}^{*2}} - \left(1 - \frac{r_c}{c}\right)\left(a - \frac{1}{\bar{\eta}^{*2}}\right)\right] \\ &= -\delta\bar{\eta}\frac{r_c}{c}\left(1 - \frac{1}{\bar{\eta}^{*2}}\right)\end{aligned} \tag{3.71}$$

which is zero if and only if $\bar{\eta}^* = 1/\sqrt{a}$, which is the fixed point condition for the non-gradient OR model. Since there are necessarily corrections depending on $\tilde{c}$, this shows that there are no valid $\lambda = 0$ modes, and thus that the fixed point predicted by the gradient OR model is unique. The next simplest case is the case where $\delta\bar{\eta} = 0$. In this case we have

$$\begin{aligned}\lambda\delta\tilde{\eta} &= \bar{\eta}^*\left(\delta\gamma - \langle\delta\gamma\rangle\right) \\ &= -\frac{1}{\epsilon}\delta\tilde{\eta} - \frac{c(r)}{\epsilon}\delta\tilde{\eta}' + \frac{1}{\epsilon}\langle c(r)\delta\tilde{\eta}'\rangle\end{aligned} \tag{3.72}$$

Since the discontinuity at r_c is proportional to $\delta\bar{\eta}$ these modes are continuous at the jump. Then since both sides of the jump have the same constant offset $\langle c(r)\delta\tilde{\eta}'\rangle$, constant of

integration is zero unless the average $\langle c(r)\delta\tilde{\eta}'\rangle$ is zero. Because of this, no modes with $\delta\bar{\eta} = 0$ are nonzero for $r > r_c$. Then the problem reduces to:

$$\lambda\delta\tilde{\eta} = -\frac{1}{\epsilon}\delta\tilde{\eta} \tag{3.73}$$

So all modes with $\delta\bar{\eta} = 0$ are stable with eigenvalue $-\epsilon^{-1}$, but there are no $\delta\bar{\eta} = 0$ modes that are nonzero for $r > r_c$. In order to access the rest of the spectrum the $\delta\bar{\eta} \neq 0$ modes are necessary. Since we are assuming $\delta\bar{\eta} \neq 0$, it is sufficient to address the eigenvalue problem for $\delta\bar{\eta}$:

$$\begin{aligned}
\lambda\delta\bar{\eta} &= -\frac{1}{\epsilon}\left\langle c(r)\delta\tilde{\eta}'\right\rangle - a\delta\bar{\eta} \\
&= -\frac{1}{\epsilon}\left[-\epsilon\delta\bar{\eta}\frac{r_c}{2}\left\langle\delta(r_c - r)\right\rangle - \bar{\eta}\epsilon\left(1 - \frac{r_c(1+\lambda\epsilon)}{c}\right)\left\langle e^{\frac{r_c - r}{c}(1+\lambda\epsilon)}\Theta(r - r_c)\right\rangle\right] - a\delta\bar{\eta} \\
&= \delta\bar{\eta}\left[\frac{1}{\bar{\eta}^{*2}} - a + \left(1 - \frac{r_c}{c}(1+\lambda\epsilon)\right)\left\langle e^{\frac{r_c - r}{c}(1+\lambda\epsilon)}\Theta(r - r_c)\right\rangle\right]
\end{aligned} \tag{3.74}$$

This transcendental equation for λ describes the spectrum of the operator for all eigenfunctions $\delta\eta$ that have nonzero $\delta\bar{\eta}$ and thus $\delta\tilde{\eta}(r > r_c) \neq 0$. This cannot be solved analytically in general, but first order approximations to the family of solutions can be found. We describe the first order approximations for small ϵ, then taking the additional limits of weak and strong gradient feedback. First, to low order in ϵ the problem becomes:

$$\begin{aligned}
\lambda\delta\bar{\eta} &= \delta\bar{\eta}\left[\frac{1}{\bar{\eta}^{*2}} - a + \left(1 - \frac{r_c}{c}(1+\lambda\epsilon)\right)\left\langle e^{\frac{r_c - r}{c}(1+\lambda\epsilon)}\Theta(r - r_c)\right\rangle\right] \\
&= \delta\bar{\eta}\left[\frac{1}{\bar{\eta}^{*2}} - a + \left(1 - \frac{r_c}{c}(1+\lambda\epsilon)\right)\left\langle e^{\frac{r_c - r}{c}}\left(1 + \lambda\epsilon\frac{r_c - r}{c}\right)\Theta(r - r_c)\right\rangle\right] + \mathcal{O}(\epsilon) \\
&= \delta\bar{\eta}\left[\frac{1}{\tilde{c}}\left(\frac{1}{\bar{\eta}^{*2}} - a\right) + \lambda\epsilon\left(\frac{1}{\tilde{c}}\left(\frac{1}{\bar{\eta}^{*2}} - a\right) + \frac{1}{\tilde{c}}\left(1 - \frac{1}{\tilde{c}}\right)\left\langle e^{\frac{1 - r/r_c}{\tilde{c}}}\left(1 - \frac{r}{r_c}\right)\Theta(r - r_c)\right\rangle\right)\right]
\end{aligned} \tag{3.75}$$

This then gives an expression for λ:

$$\begin{aligned}
&\lambda\left[1-\epsilon\left(\frac{1}{\tilde{c}}\left(\frac{1}{\bar{\eta}^{*2}}-a\right)+\frac{1}{\tilde{c}}\left(1-\frac{1}{\tilde{c}}\right)\left\langle e^{\frac{1-r/r_c}{\tilde{c}}}\left(1-\frac{r}{r_c}\right)\Theta(r-r_c)\right\rangle\right)\right]=\frac{1}{\tilde{c}}\left(\frac{1}{\bar{\eta}^{*2}}-a\right)\\
\implies &\lambda=\frac{1}{\tilde{c}}\left(\frac{1}{\bar{\eta}^{*2}}-a\right)\left[1+\epsilon\left(\frac{1}{\tilde{c}}\left(\frac{1}{\bar{\eta}^{*2}}-a\right)+\frac{1}{\tilde{c}}\left(1-\frac{1}{\tilde{c}}\right)\left\langle e^{\frac{1-r/r_c}{\tilde{c}}}\left(1-\frac{r}{r_c}\right)\Theta(r-r_c)\right\rangle\right)\right]
\end{aligned} \tag{3.76}$$

The average of the remaining exponential is calculated as follows:

$$\begin{aligned}
\left\langle e^{\frac{1-r/r_c}{\tilde{c}}}\left(1-\frac{r}{r_c}\right)\Theta(r-r_c)\right\rangle =&\frac{2}{r_d^2}\int_{r_c}^{r_d} e^{\frac{1-r/r_c}{\tilde{c}}}\left(1-\frac{r}{r_c}\right)rdr\\
=&\frac{4\tilde{c}^3}{\bar{\eta}^{*2}}\left(e^{\frac{1-\bar{\eta}^*}{\tilde{c}}}-1\right)+\frac{2\tilde{c}^2}{\bar{\eta}^{*2}}\left(e^{\frac{1-\bar{\eta}^*}{\tilde{c}}}(2\bar{\eta}^*-1)-1\right)\\
&+\frac{2\tilde{c}}{\bar{\eta}^*}e^{\frac{1-\bar{\eta}^*}{\tilde{c}}}(\bar{\eta}^*-1)
\end{aligned} \tag{3.77}$$

In the limit of weak feedback the exponential terms do not contribute, leaving:

$$\left\langle e^{\frac{1-r/r_c}{\tilde{c}}}\left(1-\frac{r}{r_c}\right)\Theta(r-r_c)\right\rangle=-\frac{2\tilde{c}^2}{\bar{\eta}^{*2}}\left(2\tilde{c}+1\right) \tag{3.78}$$

This gives the following value for λ:

$$\lambda=a(-2+\tilde{c}(3-2a\epsilon))+\mathcal{O}(\epsilon^2,\tilde{c}^2) \tag{3.79}$$

As expected, this is a $\mathcal{O}(\tilde{c}$ correction to the $\delta\tilde{\eta}\neq 0$ eigenvalue for the $\delta\bar{\eta}\neq 0$ mode for the non-gradient OR model. In the strong feedback limit the exponential terms become linear and λ takes the following form:

$$\lambda=\frac{a}{\tilde{c}}\left(-1+2a\epsilon\right) \tag{3.80}$$

In both cases $\lambda<0$ indicating that the system is stable.

The stability for non-axisymmetric perturbations is described by the growth rate $\delta\gamma_{n,i}$ for $\delta\eta_{n,i}$ as defined previously.

$$\begin{aligned}
\lambda\delta\eta_{n,i}=&\bar{\eta}^*\delta\gamma_n=-\frac{1}{\epsilon}\left(\delta\eta_{n,i}-2(n+1)\left(\frac{r}{r_d}\right)^n\int_{r_c}^{r_d}\left(\frac{r}{r_d}\right)^{n+1}\delta\eta_{n,i}\frac{dr}{r_d}\right)\\
&-\frac{c(r)}{\epsilon}\left(\delta\eta'_{n,i}-\frac{2n(n+1)}{r_d}\left(\frac{r}{r_d}\right)^{n-1}\int_{r_c}^{r_d}\left(\frac{r}{r_d}\right)^{n+1}\delta\eta_{n,i}\frac{dr}{r_d}\right)
\end{aligned} \tag{3.81}$$

Analogous to the axisymmetric case, if $\delta\eta$ is chosen such that the integral is zero one finds $\lambda = -1/\epsilon$ for modes that vanish for $r > r_c$. The zero mode associated with compatible growth (see appendix B.1.4) is also present. The rest of the spectrum is made up of modes with $\delta\eta_n = r^n + \delta H_n$, where $\delta H_n = 0$ for $r < r_c$. The eigenvalue problem for $r > r_c$ is the following (since $\delta\bar{\eta} = 0$ for higher harmonic modes these modes are continuous at $r = r_c$, providing the necessary boundary condition):

$$\delta\eta_{n,i}(\lambda\epsilon + 1) + c\delta\eta'_{n,i} = 2(n+1)(r + nc)\frac{r^{n-1}}{r_d^n}\int_0^{r_d}\left(\frac{r'}{r_d}\right)^{n+1}\delta\eta_{n,i}\frac{dr}{r_d} \tag{3.82}$$

Due to the complexity of this problem we only address the strong feedback case, as it is of the greatest relevance. We rescale r to $\rho = r/r_c$ and as before let $z = r_c/c$. Then the eigenvalue problem becomes:

$$(\lambda\epsilon + 1)\delta\eta_n = 2(n+1)\rho^n\tilde{I} \qquad \rho < 1 \tag{3.83}$$

$$z(\lambda\epsilon + 1)\delta\eta_n + \delta\eta'_n = 2(n+1)\rho^{n-1}(z\rho + n)\tilde{I} \qquad \rho > 1 \tag{3.84}$$

Where

$$\tilde{I} = \bar{\eta}^{*-2(n+1)}\int_0^{\bar{\eta}^*}\rho^{n+1}\delta\eta_n d\rho \tag{3.85}$$

with continuity at the boundary, since $\delta\bar{\eta} = 0$. This can be solved exactly:

$$\begin{aligned}\delta\eta_n =& \frac{2(n+1)\tilde{I}\rho^n}{\lambda\epsilon + 1} \\ &+ \frac{2(n+1)n\lambda\epsilon(-1)^n\tilde{I}}{z^n(1+\lambda\epsilon)^{n+1}}e^{-\rho z(1+\lambda\epsilon)}\left[\Gamma_n\left(-z(1+\lambda\epsilon)\right) - \Gamma_n\left(-rz(1+\lambda\epsilon)\right)\right] \\ \equiv& \frac{2(n+1)\tilde{I}\rho^n}{\lambda\epsilon + 1} + \tilde{I}H_n\end{aligned} \tag{3.86}$$

The definition of $\tilde{I}$ then becomes the eigenvalue equation:

$$\begin{aligned}
\tilde{I} &= \int_0^1 \frac{2(n+1)\tilde{I}\rho^{2n+1}}{1+\lambda\epsilon} d\rho + \left(\frac{2az^2}{(z+2)^2}\right)^{n+1} \int_1^{\bar{\eta}^*} \tilde{I}\rho^{n+1} H_n d\rho \\
&\equiv \int_0^1 \frac{2(n+1)\tilde{I}\rho^{2n+1}}{1+\lambda\epsilon} d\rho + \tilde{I}\tilde{H} \\
\implies 1 &= \frac{1}{1+\lambda\epsilon} + \tilde{H} \\
\implies \lambda\epsilon &= \frac{1}{1-\tilde{H}} - 1
\end{aligned} \tag{3.87}$$

Then in order to determine the stability of the system we need only to examine the behavior of $\tilde{H}$:

$$\begin{aligned}
\tilde{H} = &\left(\frac{2az^2}{(z+2)^2}\right)^{n+1} \frac{2(n+1)n\lambda\epsilon(-1)^n}{z^n(1+\lambda\epsilon)^{n+1}} \\
&\times \int_1^{\bar{\eta}^*} \rho^{n+1} e^{-\rho z(1+\lambda\epsilon)} \left[\Gamma_n\left(-z(1+\lambda\epsilon)\right) - \Gamma_n\left(-\rho z(1+\lambda\epsilon)\right)\right] d\rho
\end{aligned} \tag{3.88}$$

We first note that $\lambda = 0$ gives a valid solution, representing the modes describing compatible growth (see appendix B.1.4). In order to analyze the rest of the spectrum some limiting arguments will be required. The limit of strong feedback corresponds to $z \to 0$, with λ depending on z.

It is helpful to consider $\lambda \to \lambda_0 z^m$, distinguishing three cases: $m > 0$, $m < 0$, and $m = 0$. For $m > 0$, we find that we must have

$$\tilde{H} \to 0 \tag{3.89}$$

as $z \to 0$. Thus the eigenvalue condition is reduced to

$$\lambda = \tilde{H} \tag{3.90}$$

Then since H_n is proportional to λ we define $\lambda_0 \tilde{H}_0 \equiv \tilde{H}$. This implies that $\tilde{H}_0 \sim z^m$. On the other hand, it is clear from the definition of H_n that $\tilde{H}_0 \sim z^{m-n}$. So we have a contradiction and cannot have $\lambda = \mathcal{O}(z^m)$ for $m > 0$. For $m < 0$ the eigenvalue condition requires that

$$\tilde{H} \to 1 \tag{3.91}$$

in the limit $z \to 0$. On the othe hand, the integrand H_n can be seen to limit to either 0 or $\pm\infty$, depending on the sign of λ_0 and n, giving another contradiction. Thus we must have $\lambda = \mathcal{O}(z^0)$. In this limit the integral can be evaluated as follows:

$$\tilde{H} = \left(\frac{a}{2}\right)^{n+1} \frac{\lambda\epsilon}{\lambda\epsilon+1} {}_2F_2\left(1, (2(n+1)); n+1, 3+2n; -(1+\lambda\epsilon)\right) \tag{3.92}$$

Where ${}_2F_2$ is the generalized hypergeometric function. The eigenvalue condition then simplifies to

$$\left(\frac{2}{a}\right)^{n+1} = {}_2F_2\left(1, (2(n+1)); n+1, 3+2n; -(1+\lambda\epsilon)\right) \tag{3.93}$$

Since the second set of arguments of ${}_2F_2$ are larger than the first for all $n > 0$, the hypergeometric function is bounded from above by $\exp(-(1+\lambda\epsilon))$, which only has $\lambda < 0$ solutions for the eigenvalue problem, showing that the system is stable.

Since the growth rate is considered as a power series in the pressure and its derivative it is natural to consider feedback on the Laplacian of the pressure as well. This can be done (see appendix B.2) and the resulting model can be shown to reproduce similar qualitative features as the gradient model, including uniform growth of a quasi-steady state, stability except for the necessary soft modes due to compatible growth (see appendix B.1.4), and a unique final disk size.

Gradient feedback is a consistent model of growth control by mechanical feedback. Gradient feedback smoothens the pressure configurations generated through growth, and strong enough gradient feedback can make up for a sharp cutoff in morphogen concentration to prevent apoptosis. Such a sharp cutoff could be present if the signaling molecule directly regulating the growth rate is downstream from the primary morphogens with weak gradients and is controlled by an ultrasensitive switch. Such a switching mechanism would magnify the cutoff detected by the tissue.

3.7 Discussion

Our goal was to compare different models of growth control by mechanical feedback and distinguish them based on macroscopic properties, using the *Drosophila* wing imaginal disk as a model system. To this end we introduced a theoretical framework and a limit which allows different families of models to be analyzed on equal terms, giving direct comparisons for the macroscopic properties of interest, including robustness of final tissue size, the spatiotemporal patterning of apoptosis, and the uniformity of growth.

We introduced two broad families of mechanical feedback models, distinguished by how they produce growth arrest despite extensile stresses in peripheral regions of the disk. The AND family of models prohibits all growth in these exterior regions, turning off growth control dynamics completely. The OR family of models allows growth factor concentrations to trade off with local pressure in different ways at different locations in the disk, leading to growth inhibition even in some sections where the pressure is negative.

We demonstrated that models in the AND model family, those that require the growth rate to vanish over macroscopic sections of tissue, do not predict unique final sizes for tissues, and confirmed arguments [30] that direct damage to the tissue would result in overgrowth. Moreover, we identified this overgrowth response as deriving from a fundamental nonuniqueness implicit in the model structure.

Models in the OR family predict unique final sizes as a consequence of the fixed point conditions describing a unique growth state at every point on the disk, which for the simple OR model and the gradient OR model comes at the cost of predicting a negative $M(r)$ far from the center. This means that these models predict cell death is predicted in these regions in the absence of extensile stress, which could be produced either by cutting the tissue to relax the stresses or by biochemically perturbing the system such that the signaling pathway detected either an absence of stress or contractile stress. For shallow morphogen gradients, the region where $M(r) < 0$, and therefore the region in which such perturbations would induce apoptosis, is macroscopically large. On the other hand, the simplest model in the OR family predicts apoptosis for steep morphogen gradients. Introducing gradient feedback, promoting growth in response to sharp changes in pressure, prevents apoptosis for strong enough gradient feedback. We showed that models with gradient feedback predict a unique final disk size under the condition that gradient feedback is not active close enough to the center of the disk. This provides the necessary boundary conditions for the fixed point condition to have a unique solution, and is supported by the biochemistry of the *Drosophila* wing disk [2]. We introduced two models of derivative feedback, one that feeds back on gradients in pressure and one that feeds back on the Laplacian, either of which could appear as a low order term in an expansion of the growth rate as a power series in the pressure and its derivatives, with appropriate morphogen distributions. The gradient model is a simple extension of the gradient-free OR model and reduces to it in the limit where the strength of the gradient feedback vanishes. The Laplacian feedback model does not necessarily reduce to a valid simple OR model in the limit of vanishing Laplacian feedback since it does not require $M(r) < 0$ anywhere. In cases where $M(r) > 0$ everywhere, in the limit of vanishing

Laplacian feedback the model predicts dramatic overgrowth before apoptosis leading to a small final size (see appendix B.2). The lack of a necessary region where $M(r) < 0$, combined with the natrual interperetation of detecting a Laplacian of the pressure by cells averaging over pressures detected by their neighbors, make the Laplacian model a potentially appealing alternative. We analyzed the fixed point structures of these models and showed that they are linearly stable. The experimental predictions associated with each of the families of model that we analyzed are summarized in table 3.1.

Model Predictions		
AND model:		· No unique final size · Final size depends on feedback strength
OR models:	All	· Unique final size · Final size independent of feedback strength
	Proportional feedback	· Sharp morphogen gradients: spatiotemporal apoptosis patterns near edge of disk · Shallow morphogen gradients: apoptosis over large sections of disk if pressure vanishes
	Gradient feedback	· No apoptosis even with sharp morphogen gradients for $\tilde{c} \gg 1$ · Shallow morphogen gradients: apoptosis over large sections of disk if pressure vanishes
	Laplacian feedback	· No apoptosis even with sharp morphogen gradients for $\tilde{c} \gg 1$ · Disk doesn't stop growing if pressure vanishes

Table 3.1: Summary of results

This study focused on a strong feedback limit (low order in ϵ) to control the elasticity and ensure that linear elasticity was valid at all points. It is, however, possible for linearized elasticity to be valid outside of the regime of strictly small w_{ij} due to material properties. It may then be valid to linearize the elasticity but allow some higher order terms in ϵ into the dynamics. In this case we expect the essential results are valid. For example, it is possible to derive a similar system of ODEs for the AND model and see that the line of degenerate fixed points is maintained, as are the essential results of the linear stability (see appendix B.4). In the OR model the analysis becomes substantially more complex, but it can be demonstrated that terms proportional to $\delta w M'(r)$ will appear, which could play a similar role to θ dependence in $M(r, \theta)$ in removing soft modes in the non-axisymmetric problem (see appendix B.5).

Although the specific model system that we treated was the *Drosophila* wing disk, this

model framework is broadly generalizable to any systems in which growth is controlled by mechanical feedback, with the specifics of the biology determining the relevant observables and limits. Work studies of plants [8] have used mechanical feedback models to describe a qualitatively different situation, in which mechanical feedback introduces nonuniformities in growth. In this case a growth rate that is nonlinear in the stress (or equivalently the growth) is necessary to amplify the nonuniformities in this way. Additionally, studies of tumor spheroids have also demonstrated mechanical feedback [66] and the biology of this system is also radically different. In the tumor spheroid systems, due to the presence of significant apoptosis, steady-states with net fluxes of cells are possible, indicating that $\gamma = 0$ is not a valid criterion for identifying the steady state.

If fully anisotropic growth is considered the dynamics would be given in terms of a symmetric growth rate tensor γ_{ij}, depending on the full stress tensor σ_{ij} as well as tensors deriving from morphogen distributions. This would introduce feedback on the shear stress, which can cause fluidization of the tissue on long timescales [152]. Such a fluidization process could complicate the mechanism of precise tissue size detemination by mechanical feedback if the shear relaxation time is short compared to the timescale of development. If the shear relaxation time were short it could potentially disrupt the fixed points described here. This is not expected in the AND model, since there is no growth at all in the exterior region and in the interior region there is a uniform pressure, which can be supported by a fluid. Such a fluidization could disrupt the OR model but there are general issues with feedback on the full stress tensor (see appendix B.6) that suggest that size control mechanisms should involve primarily isotropic feedback.

There are other models of the *Drosophila* wing disk that we do not treat here. The entelechia model, in which information about position is inferred from neighboring interactions, has been proposed as a mechanism for size determination but it has yet to be shown that the necessary candidate signaling molecules are expressed in the shallow gradient patters necessary for this model [67]. Models in which individual cells measure time derivatives of relevant morphogens in order to control growth have also been proposed but these are known to not predict a unique final disk size [125]. A mechanism that allows a tissue to robustly reach a final size by the measuring the dilution of some morphogen distribution has been demonstrated to be consistent with the growth dynamics of the *Drosophila* eye disk [188], but this mechanism is not consistent with wing disk growth [189].

In summary, it is nontrivial for mechanical feedback models of growth control to predict a unique final tissue size. Models that require the growth rate to be identically zero over

some finite region will necessarily have a continuous family of possible final sizes. Only models that allow the growth dynamics due to pressure and due to chemical signaling by morphogens over the entire tissue can have unique final sizes. Future work will investigate the ability of mechanical feedback models to control "compatible growth" modes that evolve without generating stress, as well as study how stochastic fluctuations can affect the growth dynamics described here.

Chapter 4

Conclusion

In this work we have seen two examples where it has been possible to distinguish different feedback structures by identifying characteristic dynamics. We first showed that it was possible to identify whether positive or negative feedback was dominant in the circadian oscillator of S. Elongatus by examining how the period of the oscillation changed when the effect of KaiA sequestration was modulated. We then showed how different feedback structures for mechanical feedback models of growth control would respond to perturbations of different kinds, such as tissue damage or biochemical disruption of the feedback pathway.

Phenomenology and a detailed understanding of the experimental details in these systems was vital for coming to these conclusions. Which kinds of experiments have been done, and which are reasonably feasible, determine what sorts of observables are meaningful, and which kinds of properties it is meaningful for models to constrain. For example, if one knew every reaction rate for each reaction in the Kai protein oscillator it would be trivial to distinguish positive from negative feedback. On the other hand, it would be an understatement to say that acquiring that information to the accuracy necessary for such a judgement would be unrealistic. Identifying readily accessible (and in this case, available) experimental observables is therefore as necessary as being able to formally distinguish the models, if they are to be useful to other workers in the field.

Essentially, comparing models that are highly constrained by directly available experiments is a way of making the most efficient use of those experimental results. This is a benefit of phenomenological models in general. These models can produce nontrivial predictions that are not immediately obvious to a qualitative analysis, and being able to distinguish between different models provides a great deal of information about the structure of the system under investigation. This is perhaps an explanation for their broad application at many

different levels of organization in biology.

Just as important as identifying practical experimental observables is identifying reliable theoretical foundations. Mass action kinetics and elasticity provide firm foundations for theoretical modeling, and are based on fundamental physical principles, such as the laws of thermodynamics, that place strict constraints on the forms of the models that are based on them. These fundamental principles will remain valid for any biological process, even if they are pushed into unfamiliar territory.

Thus, it is the principles of physics that describe the individual motions and forces that make up the construction of biological systems. While DNA contains the information necessary for life, the physical motions and structures that make up individual living things rely on physical processes acting in regular ways. Even when biological design principles are discovered, to the extent to which they are not required by these fundamental physics, it will always be possible to find exceptions.

Appendix A

Further Discussion of Clock Models

A.1 Modifications of basic models don't change qualitative behavior

To test how robust these results are to complications to the model structure we investigated published extensions to the previously presented models. These extensions show very similar responses to changing their sequestration stoichiometry as the original models do, supporting the hypothesis that these responses represent a general distinction between dynamics that are driven primarily by delay or primarily by positive feedback.

A.1.1 Allosteric model

In 2010 a number of extensions to the allosteric model were introduced [203], but the one that is most relevant here is one that allows KaiA to bind to KaiC and promote autophosphorylation in either one of the conformational states hypothesized by the allosteric model. It allows KaiA to promote autophosphorylation in the inactive allosteric state, adding the following interactions:

$$\begin{aligned} \tilde{C}_i + A &\leftrightharpoons A\tilde{C}_i \rightarrow C_{i+1} + A \\ A_m B_2 \tilde{C}_i + A &\leftrightharpoons A_{m+1} B_2 \tilde{C}_i \rightarrow A_m B_2 C_{i+1} + A \end{aligned} \tag{A.1}$$

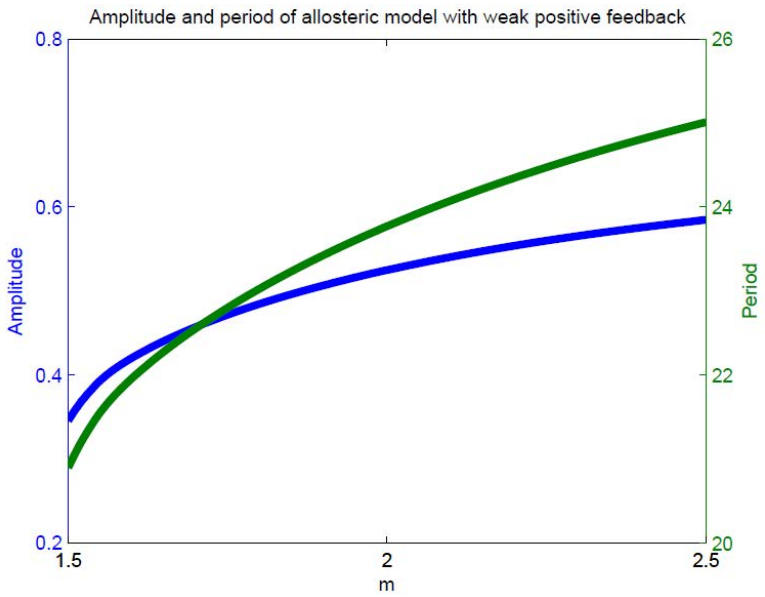

Figure A.1: The qualitative trends in the amplitude and period dependence of the allosteric model are robust to the addition of a small amount of positive feedback into the model. Parameters are identical to the standard allosteric model but with KaiA binding to the C-terminal domain and promoting phosphorylation on inactive KaiC hexamers at 1/100 the affinity of an active hexamer

A.1.2 Monomer model

The monomer model was also extended [146], in this case to include explicit KaiB binding, and allows the KaiB-bound doubly phosphorylated state to weakly sequester KaiA in addition to the state that is phosphorylated only on the serine residue. It still relies on positive feedback on the S phosphorylation state, albeit now bound to KaiB, so it should exhibit a similar response to the original model to the modification of sequestration stoichiometry. We see this is supported in A.3. This model differs from the 2007 version of the model by adding an irreversible step that corresponds to ATPase activity allowing KaiB to bind to the S and D states. These KaiB bound monomers are then the ones that participate in sequestering KaiA. Ddoes in fact participate in KaiA sequestration, but only to 2% of the extent to which Ssequesters KaiA, according to the published parameter set. The ODEs

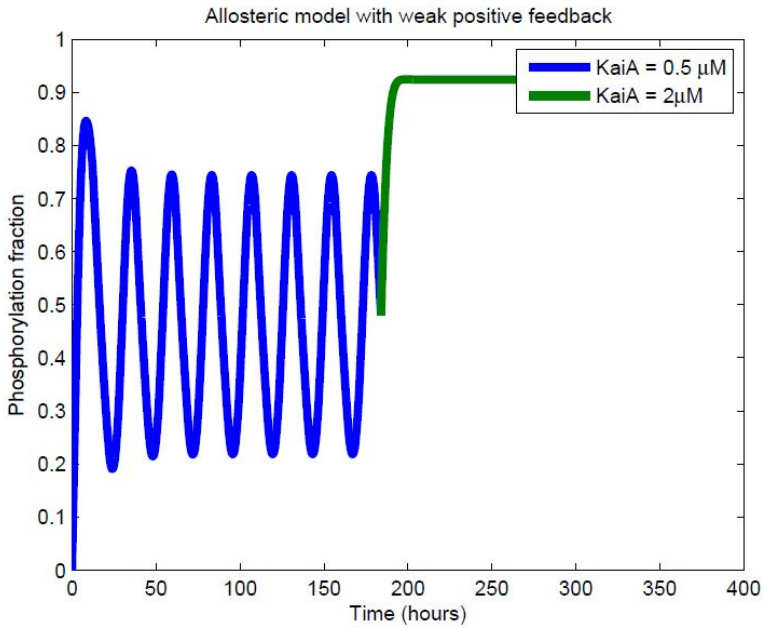

Figure A.2: The addition of a small amount of positive feedback to the allosteric model allows it to reproduce the experimental result that adding a large amount of KaiA during dephosphorylation will cause an increase in phosphorylation, while maintaining dynamics that are generally dominated by negative feedback and delay effects. The addition of KaiA is indicated by the trace changing from blue to green.

that govern the system are then:

$$\begin{aligned}
\frac{dU}{dt} &= k_{TU}(S)\,T + k_{SU}(S)\,S + k_{SBU}(S)\,SB - k_{UT}(S)\,U - k_{US}(S)\,U \\
\frac{dS}{dt} &= k_{US}(S)\,U + k_{DS}(S)\,D - k_{SU}(S)\,S - k_{SD}(S)\,S - k_{bc}S \\
\frac{dT}{dt} &= k_{UT}(S)\,U + k_{DT}(S)\,D - k_{DBT}(S)\,DB - k_{TU}(S)\,T - k_{TD}(S)\,T \\
\frac{dD}{dt} &= k_{TD}(S)\,T + k_{SD}(S)\,S - k_{DT}(S)\,D - k_{DS}(S)\,D - k_{bc}D \\
\frac{dDB}{dt} &= k_{bc}D + k_{SBDB}(S)\,SB - k_{DBSB}(S)\,DB - k_{DBT}(S)\,DB \\
\frac{dSB}{dt} &= k_{bc}S + k_{DBSB}(S)\,DB - k_{SBDB}(S)\,SB - k_{SBU}(S)\,SB
\end{aligned} \tag{A.2}$$

Where the S dependence of the reaction rates is the same as before, and k_{bc} is an S independent rate of ATPase triggered catalysis of complex formation. The amount of free KaiA is given by $A = \max\{0, A^T - mSB - nDB\}$. Unless otherwise stated the parameters are those given by table S5 in [146].

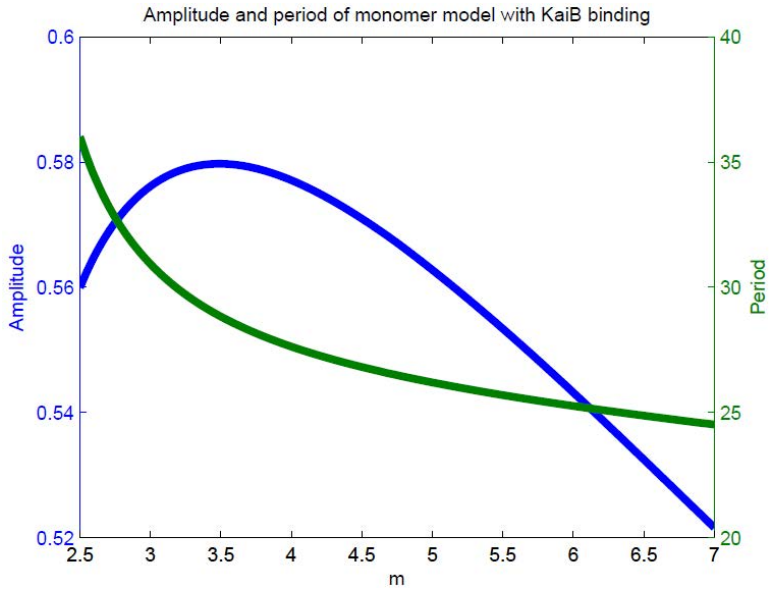

Figure A.3: The amplitude and period of the monomer model with explicit KaiB binding as described show the same general trends and features as in the original monomer model.

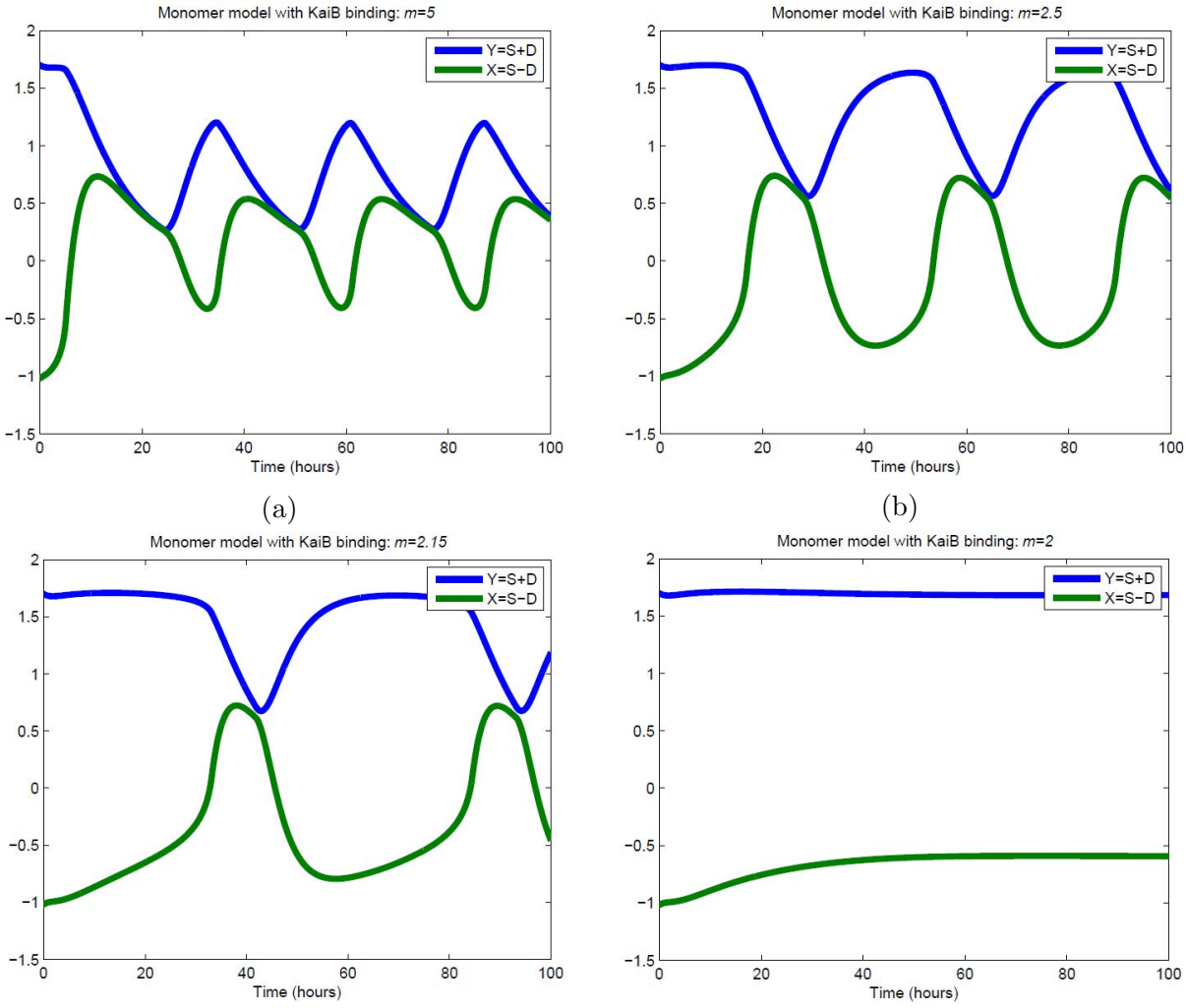

Figure A.4: An examination of a version of the monomer model extended to include explicit KaiB binding. Comparing to Fig. 10, it is possible to see the same general qualitative features that were predicted by the reduced 2 degree of freedom model, as described in the main text.

By comparing A.4 to 2.8 it is possible to see that it shares the key characteristics that indicate that the dynamics described in the reduced model are still dominant for this extension. Specifically, changes in the sign of the derivative of Y are associated with large changes in the magnitude of X, and the majority of the effect on the period is from the time when most of the KaiA is unsequestered. This suggests that this behavior is generic or at least very common in models that involve strong positive feedback as the primary driver of the oscillation. Here the effective sequestration stoichiometry for D DB is changed in proportion with that for SB .

Thus the effect of varying the stoichiometry m of KaiA sequestration is robust to minor changes in the models studied here. This suggests that the effect of introducing a competitive binder for the KaiA sequestration site on the amplitude and the period is a reliable indicator of the sign of the feedback that KaiA sequestration introduces into the dynamics of the S. Elongatus circadian system.

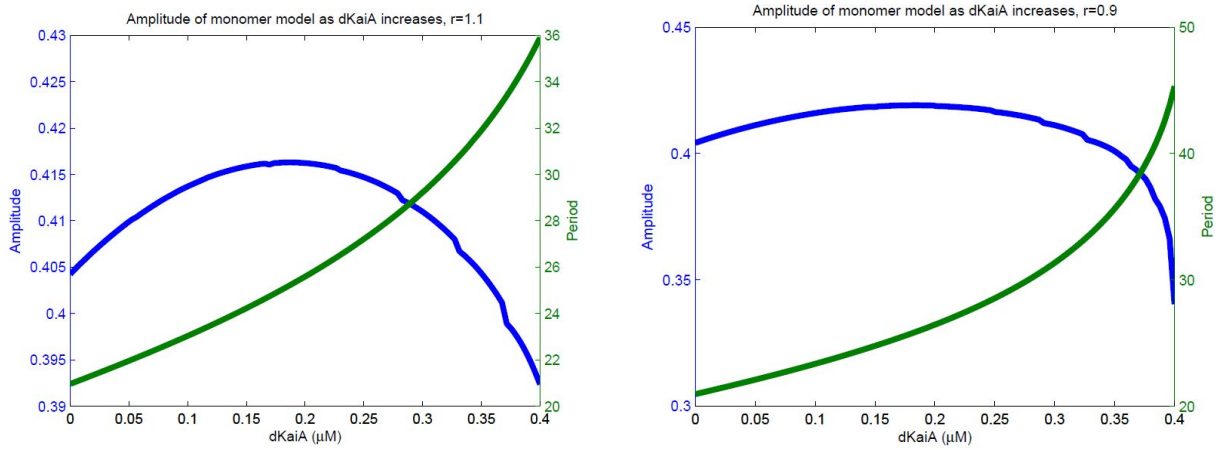

(a) (b)

Figure A.5: An examination of a version of the monomer model extended to include explicit KaiB binding. Comparing to Fig. 10, it is possible to see the same general qualitative features that were predicted by the reduced 2 degree of freedom model, as described in the main text.

A.1.3 ODEs for allosteric model

And the following differential equations:

$$\begin{aligned}
\frac{dC_i^T}{dt} =& \sigma_{i-1}^{ps} C_{i-1}^T + \sigma_{i+1}^{dps} C_i^T - (\sigma_i^{ps} + \sigma_i^{dps}) C_i^T - \sigma_i^{Ff} C_i^T + \sigma_i^{Fb} \tilde{C}_i \\
\frac{d\tilde{C}_i}{dt} =& \tilde{k}_{ps} \tilde{C}_{i-1} + \tilde{k}_{dps} \tilde{C}_{i+1} - (\tilde{k}_{ps} + \tilde{k}_{dps}) \tilde{C}_i + \sigma_i^{Ff} C_i^T - \sigma_i^{Fb} \tilde{C}_i \\
& - k_i^{Bf} \left(B^T - 2 \sum_i B_2 \tilde{C}_i^T \right)^2 \tilde{C}_i + \frac{k_i^{Bb} \tilde{K}_i^m B_2 \tilde{C}_i^T}{\tilde{K}_i^m + A^m} \\
\frac{B_2 \tilde{C}_i^T}{dt} =& \tilde{k}_{ps} B_2 \tilde{C}_{i-1}^T + \tilde{k}_{dps} B_2 \tilde{C}_{i+1}^T - (\tilde{k}_{ps} + \tilde{k}_{dps}) B_2 \tilde{C}_i^T \\
& + k_i^{Bf} \left(B^T - 2 \sum_i B_2 \tilde{C}_i^T \right)^2 \tilde{C}_i - \frac{k_i^{Bb} \tilde{K}_i^m B_2 \tilde{C}_i^T}{\tilde{K}_i^m + A^m}
\end{aligned} \tag{A.3}$$

Where concentration of total KaiA is enforced by the condition:

$$A + \sum_{i=0}^{6} \frac{A C_i^T}{K_i + A} + m \sum_{i=0}^{6} \frac{A^m B_2 \tilde{C}_i^T}{\tilde{K}_i^m + A^m} - A^T = 0 \tag{A.4}$$

Here and throughout we use the same symbol for both concentration and species and let context distinguish them. Here A and B and the concentrations of free KaiA and KaiB, respectively. $C_i$and $\tilde{C}_i$ are the concentrations of active and inactive KaiC hexamers with i monomers phosphorylated. Concentrations marked with a superscript T are the total concentrations of the respective protein. The effective phosphorylation rates are:

$$\sigma_i^{ps} = \frac{k_{ps} K_i + k_{pf} A}{K_i + A}, \quad \sigma_i^{dps} = \frac{K_i k_{dps}}{K_i + A} \tag{A.5}$$

The flipping rates are $\sigma_i^{Ff} = \frac{f_i K_i}{K_i + A}$, $\sigma_i^{Fb} = b_i . K_i$ and $\tilde{K}_i$ are the dissociation constants for KaiA binding to the active and inactive allosteric state, respectively. $\tilde{k}_{ps}$ and $\tilde{k}_{dps}$ are the phosphorylation and dephosphorylation rates. The transition rates between the active and inactive allosteric states are f_i and b_i. $K_i = \frac{k_i^{Ab}}{k_i^{Af}}$ and $\tilde{K}_i = \frac{\tilde{k}_i^{Ab}}{\tilde{k}_i^{Af}}$ are the dissociation constants for KaiA binding to the active and inactive segments of the cycle. K_i^{Bf} and K_i^{Bb} are the forward and backward rates for KaiB binding to inactive KaiC.

A.2 Derivations for monomer model analytics

A.2.1 Reducing the monomer model

Due to the simplicity of the original monomer model it is possible to derive analytic results which can describe the relationship between m and the period. The only approximation is that the separation of time scales is large. In particular, by taking phosphorylation on the threonine residue to be much faster than that on the serine residue it is possible to reduce this to a 2 degree of freedom system, for which there exist powerful tools for the analysis of nonlinear oscillations, especially of the relaxation type. This is valid because the rate constants for T phosphorylation in the model as published are generally higher than those for S. This is implemented analytically by multiplying the fast rates (phosphorylating and dephosphorylating the threonine residue) by $\frac{1}{\epsilon}$:

$$\begin{aligned}
\dot{U} &= \frac{1}{\epsilon}\left(k_{tu}T - k_{ut}U\right) + k_{su}S - k_{us}U \\
\dot{T} &= \frac{-1}{\epsilon}\left(k_{tu}T - k_{ut}U\right) + k_{dt}D - k_{td}T \\
\dot{D} &= \frac{1}{\epsilon}\left(k_{sd}S - k_{ds}D\right) - k_{dt}D + k_{td}T \\
\dot{S} &= \frac{-1}{\epsilon}\left(k_{sd}S - k_{ds}D\right) - k_{su}S + k_{us}U
\end{aligned} \tag{A.6}$$

We then take the change of variables:

$$\begin{aligned}
W &= T + U \\
X &= S - D \\
Y &= S + D \\
Z &= T - U
\end{aligned} \tag{A.7}$$

Solving for the new variables gives:

$$\begin{aligned}
S &= \frac{X+Y}{2} \\
D &= \frac{Y-X}{2} \\
T &= \frac{W+Z}{2} \\
U &= \frac{W-Z}{2}
\end{aligned} \tag{A.8}$$

Rewriting the ODE in terms of the new variables gives:

$$\begin{aligned}
\dot{W} =& \frac{Y}{2}\left(k_{su}+k_{dt}\right)+\frac{X}{2}\left(k_{su}-k_{dt}\right)-\frac{W}{2}\left(k_{us}+k_{td}\right)-\frac{M}{2}\left(k_{td}-k_{us}\right)\\
\dot{X} =& \frac{1}{\epsilon}\left(Y\left(k_{ds}-k_{sd}\right)-X\left(k_{ds}+k_{sd}\right)\right)+\frac{W}{2}\left(k_{us}-k_{td}\right)-\frac{Z}{2}\left(k_{us}+k_{td}\right)\\
&+\frac{Y}{2}\left(k_{dt}-k_{su}\right)-\frac{X}{2}\left(k_{dt}+k_{su}\right)\\
\dot{Y} =& \frac{W}{2}\left(k_{td}+k_{us}\right)+\frac{Z}{2}\left(k_{td}-k_{us}\right)-\frac{L}{2}\left(k_{dt}+k_{su}\right)-\frac{X}{2}\left(k_{su}-k_{dt}\right)\\
\dot{Z} =& \frac{1}{\epsilon}\left(W\left(k_{ut}-k_{tu}\right)-Z\left(k_{ut}+k_{tu}\right)\right)+\frac{Y}{2}\left(k_{dt}-k_{su}\right)-\frac{X}{2}\left(k_{dt}+k_{su}\right)\\
&+\frac{W}{2}\left(k_{us}-k_{td}\right)-\frac{Z}{2}\left(k_{us}+k_{td}\right)
\end{aligned} \tag{A.9}$$

In the $\epsilon \to 0$ limit the $\dot{X}$ and $\dot{Z}$ expressions result in self-consistent equations:

$$\begin{aligned}
0 &= -k_{tu}^{0}\left(W+Z\right)+f\left(X,Y\right)\left(k_{ut}^{A}\left(W-Z\right)-k_{tu}^{A}\left(W+Z\right)\right)\\
0 &= k_{ds}^{0}\left(Y-X\right)+f\left(X,Y\right)\left(k_{ds}^{A}\left(L-K\right)-k_{sd}^{A}\left(K+L\right)\right)
\end{aligned} \tag{A.10}$$

Where each k_{ab} is of the form $k_{ab}^{0}+f\left(X,Y\right)k_{ab}^{A}$ where $f\left(X,Y\right)=\frac{\max\left\{0,A^{T}-m(X+Y)\right\}}{k_{\frac{1}{2}}+\max\{0,A^{T}-m(X+Y)\}}$. So when there is no free KaiA, $f\left(X,Y\right)=0$ and the expression for X and Y simply gives $X=Y$. Then when there is free KaiA we can take $f\left(X,Y\right)=\frac{A^{T}-m(X+Y)}{k_{\frac{1}{2}}+A^{T}-m(X+Y)}$. The equation for X and Y gives

$$\begin{aligned}
0 =& X^{2}m\left(k_{ds}^{0}+k_{sd}^{A}+k_{ds}^{A}\right)\\
&+X\left(-k_{ds}^{0}\left(k_{\frac{1}{2}}A^{T}-mY\right)-mk_{ds}^{0}Y-\left(k_{ds}^{A}+k_{sd}^{A}\right)\left(A^{T}-mY\right)+mY\left(k_{ds}^{A}-k_{sd}^{A}\right)\right)\\
&+k_{ds}^{0}Y(k_{\frac{1}{2}}+A^{T}-mY)+\left(A^{T}-mY\right)\left(k_{ds}^{A}-k_{sd}^{A}\right)Y
\end{aligned} \tag{A.11}$$

A.2.2 Finding the turning points in the reduced monomer model

One can see from this expression that there will be terms sublinear in Y in the expression of $X\left(Y\right)$. This also provides the endpoints of each branch. One endpoint is found by finding the intersection of this expression with the line $X=Y$, the expression for the nullcline when there is no free KaiA. This reduces to:

$$0=2Y^{2}m+Y\left(-A^{T}\right) \tag{A.12}$$

Or

$$Y = \frac{A^T}{2m} \tag{A.13}$$

To find the other turning point we must remember that the parabola described above must have two distinct branches as a function of X as a function of Y. We can then find the point at which the two branches meet. This occurs at the point where the discriminant of the quadratic equation for X is equal to 0. This requirement is expressed by the relation:

$$\begin{aligned} 0 = &- \left(-k_{\frac{1}{2}}k^0_{ds} - A^T\left(k^0_{ds} + k^A_{ds} + k^A_{sd}\right) + 2k^A_{ds}Ym\right)^2 \\ &+ 4m\left(k^0_{ds} + k^A_{ds} + k^A_{sd}\right)\left(mY^2\left(-k^0_{ds} + k^A_{sd} - k^A_{ds}\right) + k^0_{ds}Y\left(A_T + k_{\frac{1}{2}}\right) - YA_T\left(k^A_{sd} - k^A_{ds}\right)\right) \end{aligned} \tag{A.14}$$

This expression is now quadratic in Y, giving two solutions:

$$\begin{aligned} 2\left(k^0_{ds} + k^A_{ds}\right)^2 mY =& A^T\left(k^0_{ds} + k^A_{ds}\right)\left(k^0_{ds} + k^A_{ds} + k^A_{sd}\right) + k_{\frac{1}{2}}k^0_{ds}\left(k^0_{ds} + k^A_{ds} + 2k^A_{sd}\right) \\ &\pm 2\sqrt{k_{\frac{1}{2}}k^0_{ds}k^A_{ds}\left(k_{\frac{1}{2}}k^0_{ds} + A^T\left(k^0_{ds} + k^A_{ds}\right)\right)\left(k^0_{ds} + k^A_{ds} + k^A_{sd}\right)} \end{aligned} \tag{A.15}$$

Obviously only one of these can be the actual value at which the points of the parabola meet so by plugging in the published parameter values it is clear that the negative of the radical must be taken since if the positive term is taken the value achieved is several orders of magnitude too high (approximately $1450/m$ as opposed to approximately $1/m$).

A.2.3 Estimating the period dependence of the of the monomer model

By reducing the system to 2 degrees of freedom we attain a model that is amenable to the mathematically well understood regime of phase plane analysis. In 2.8d we plot the nullclines of this system, curves along which each degree of freedom is constant. These nullclines have a motif, where one nullcline has an S shape and the other has a linear section that crosses the middle branch of the S-shaped nullcline, that indicates a type of positive feedback dynamics known as a relaxation oscillator. This describes a system which tracks slowly along the outer branches of S-shaped nullcline until the vertical cusp is reached. It then quickly switches to the other branch and moves slowly in the opposite direction until it reaches the other cusp and switches back to the first branch, restarting the cycle. Relaxation oscillators are sometimes understood in terms of simple electric circuits which involve a capacitor slowly

charging up to a certain voltage, suddenly discharging, and the slowly building a charge back up again. It appears that a similar mechanism is at work in the KaiA sequestration dynamics of this model. The linear part of the of the S-shaped nullcline corresponds to the situation in which all of the KaiA is sequestered and the KaiC monomers are dephosphorylating, in which case the original model becomes completely linear. This can be seen directly from the nullcline plot as both X and Y are decreasing indicating that the sum $S + T$ is decreasing, indicating dephosphorylation, but the relative amount of S, the sequestering protein, is also decreasing. By reducing the model to a one dimensional model along this nullcline it is possible to derive an analytic expression for the time spent on this branch as a function of m. The amount of time the system spends with all KaiA sequestered, which we call T_{seq}, is of the form:

$$T_{seq} = \int_{\frac{z_1}{m}}^{\frac{z_2}{m}} \frac{1}{\dot{Y}_{seq}(X(Y), Y)} dY = \int_{\frac{z_1}{m}}^{\frac{z_2}{m}} \frac{1}{-cY} dY = -\frac{\ln(Y)}{c}\Big|_{\frac{z_1}{m}}^{\frac{z_2}{m}} = -\frac{\ln(z_2) - \ln(z_1)}{c} \tag{A.16}$$

This result is notable in that it suggests that even in the full model the time spent fully sequestered does not vary strongly with m. This is supported by **??**. The expression for the time derivative of $Y$is linear since for zero free KaiA even the full three degree of freedom system becomes linear. The turning points can be shown to depend only on the reaction rate constants and the total KaiA concentration. Full expressions for the constants c, z_1, and z_2 can be found in the supplementary material. On the other branch the KaiC monomers are phosphorylating, first on the T residue and then more slowly on the S residue. This is can be seen on the nullcline plot by noting that on the nonlinear branch Y increases but X remains roughly constant, actually decreasing slightly, indicating an increase in the doubly phosphorylated KaiC as well as a smaller increase in S phosphorylated KaiC. Then once a certain amount of KaiA has been sequestered the doubly phosphorylated KaiC begins to dephosphorylate, increasing the amount of S, causing more KaiA to be sequestered in a positive feedback process. The KaiC monomers then begin to dephosphorylate and the cycle begins again. The time spent when the amount of free KaiA is nonzero has the form:

$$T_{unseq} = \int_{\frac{z_1}{m}}^{\frac{z_2}{m}} \frac{1}{\dot{Y}_{unseq}(X(Y), Y)} dY \tag{A.17}$$

$\dot{Y}_{unseq}$ is much more complex so the integral is not directly tractable. Despite this it is possible to gain some insight from this. In this case $X(Y)$ is the solution to a self-consistent

equation that leads to a quadratic equation for X, of the form:

$$X(Y) = \frac{d_1 + d_2 mY \pm \sqrt{d_3 + d_4 mY + d_5 m^2 Y^2}}{m} \tag{A.18}$$

The linear term under the radical would cause $\dot{Y}_{unseq}$ to vary sublinearly with $Y$and integrating such a term between endpoints z_1 and z_2 would cause the value of the integral to vary inversely with m.

Appendix B

Further Discussion of Disk Models

B.1 The nonlinear elasticity of growth

The linear elasticity presented in section 3.2 can be derived from a fully nonlinear theory of elasticity, incorporating deformations due to tissue growth [45, 61, 155]. This theory of elasticity modifies standard nonlinear elasticity, which distinguishes between a Lagrangian configuration for the material (assumed to be stress-free) and an Eulerian, elastically strained configuration of the material. Because growth can cause displacements in materials and induce stresses without the material being otherwise elastically strained it is necessary to introduce an intermediate configuration. This intermediate configuration is distinguished from the Lagrangian configuration, which defines some pre-growth state, and represents an abstract stress-free configuration, which may not be able to be represented in usual Euclidean space. We define the Lagrangian, intermediate, and Eulerian configurations as Ω_L, Ω_I, and Ω_E, respectively. We will follow standard convention in nonlinear elasticity and use capital Roman indices for tensors indices referring to the Lagrangian configuration and lower case Roman indices for tensor indices in the Eulerian configuration. Additionally, we will use lower case Greek indices for tensor indices in the intermediate configuration. We will be using the Einstein summation convention for repeated indices throughout, and will not distinguish between covariant and contravariant indices. There are multiple equivalent [46] ways to formulate elasticity by relating such an intermediate configuration to the standard formalism of classical nonlinear elasticity.

We begin in section B.1.1 by introducing two formalisms for treating nonlinear elasticity in growing materials, and showing that they desribe the same physics. Then in section B.1.2 we derive the linearized elasticity described in the main text from the full nonlinear theory.

In section B.1.3 we describe the solution of the linear problem for non-axisymmetric growth and derive an expression for the pressure. In section B.1.4 we describe the general conditions which can lead to growth without induced stress.

B.1.1 Comparison of different formalisms for elasticity of growing materials

Representing the elasticity of growing materials builds from the model of standard nonlinear elasticity, which relates the deformation of the Lagrangian to the Eulerian configuration by a coordinate map $x_i(X_I)$. The elastic strain tensor is then given in terms of this deformation map:

$$\mathcal{E}_{IJ} = \frac{1}{2}\left(\partial_I x_k \partial_J x_k - \delta_{IJ}\right) \tag{B.1}$$

Elastic equilibrium is the condition that the stress have zero divergence or that the variation of the total elastic free energy $\mathcal{F} = \int f d\Omega_L$ vanish:

$$0 = \partial_I S_{IJ} \tag{B.2}$$

or

$$0 = \frac{\delta \mathcal{F}}{\delta x_i(X_I)} \tag{B.3}$$

where S_{IJ} is the second Piola-Kirchoff stress tensor [31], which relates forces mapped into the stress-free configuration to areas in the stress-free configuration, which is identical to the Lagrangian configuration in standard nonlinear elasticity, in the absence of growth. We will assume that the growing tissue is an isotropic material, and thus that S_{IJ} can be represented as a derivative with respect to the energy density f:

$$S_{IJ} = \frac{\partial f}{\partial \mathcal{E}_{IJ}} \tag{B.4}$$

One can then derive similar relations for other stress tensors, such as the Cauchy stress, which relates forces to areas in the deformed configuration. There are two ways to integrate growth into this nonlinear elastic theory.

We will focus on what can be called the "target metric" formalism [45] that emphasizes how the definition of the strain in the Lagrangian configuration can be modified to encode

the growth of the material, with the strain being redefined as follows:

$$\mathcal{E}_{IJ} = \frac{1}{2}\left(C_{IJ} - \bar{g}_{IJ}\right) \tag{B.5}$$

where

$$C_{IJ} = \frac{\partial x_i}{\partial X_I}\frac{\partial x_i}{\partial X_J} \tag{B.6}$$

is the standard Cauchy-Green deformation tensor, describing the total deformation of the material in the Lagrangian configuration to the Eulerian configuration, and $\bar{g}_{IJ}$ is the "target metric", describing the local geometry of the "stress-free" configuration after growth. Effectively, all of the information about the growth is encoded in $\bar{g}_{IJ}$.

The other formalism, usually known as "morphoelasticity", focuses on the tangent maps between the three different spaces and makes explicit the distinction between deformation by growth and deformation by elastic strain [61]. In this formalism the tangent map $\partial x_i/\partial X_I$ is factored into a map defining the growth and a map defining the strain:

$$\frac{\partial x_i}{\partial X_I} \equiv \frac{\partial x_i}{\partial \xi_\alpha}\frac{\partial \xi_\alpha}{\partial X_I} \tag{B.7}$$

where the two tensors $\partial x_i/\partial \xi_\alpha$ and $\partial \xi_\alpha/\partial X_I$ are to be intepreted as defining the tangent maps from the intermediate configuration to the Eulerian configuration (defining the elastic deformation gradient) and from the Lagrangian configuration to the intermediate configuration (defining the growth deformation gradient), respectively. The totally elastic part of the strain $\mathcal{E}^e$ is then defined in the same way as usual, but on the intermediate, stress free configuration (here and in the future using the convention that repeated indicies are summed over):

$$\mathcal{E}^e_{\alpha\beta} = \frac{1}{2}\left(\frac{\partial x_i}{\partial \xi_\alpha}\frac{\partial x_i}{\partial \xi_\beta} - \delta_{\alpha\beta}\right) \tag{B.8}$$

If we pull this strain back to the Lagrangian configuration we arrive at the strain defined above:

$$\begin{aligned}\mathcal{E}^e_{\alpha\beta}\frac{\partial \xi_\alpha}{\partial X_I}\frac{\partial \xi_\beta}{\partial X_J} &= \frac{1}{2}\left(\frac{\partial x_i}{\partial X_I}\frac{\partial x_i}{\partial X_J} - \frac{\partial \xi_\alpha}{\partial X_I}\frac{\partial \xi_\alpha}{\partial X_J}\right)\\ &= \frac{1}{2}\left(C_{IJ} - \bar{g}_{IJ}\right)\end{aligned} \tag{B.9}$$

where in the last line we have identified

$$\bar{g}_{IJ} \equiv \frac{\partial \xi_\alpha}{\partial X_I} \frac{\partial \xi_\alpha}{\partial X_J} \tag{B.10}$$

so these two formalisms define the same strain tensor, up to a change of coordinates.

In each case, the elastic free energy density f is properly considered as a function on the intermediate, stress-free configuration: $f = f(\mathcal{E}^e_{\alpha\beta})$. In each case, the stress can be described as a derivative of the elastic free energy with respect to the strain [31, 45, 155], which can be calculated starting from a virtual work argument. Even for the target metric formalism it will be necessary to transform to the intermediate coordinates to take the derivative.

$$\begin{aligned}
\mathcal{F} &= \int_{\Omega_I} f(\mathcal{E}^e_{\alpha\beta}) dV_I \\
\delta\mathcal{F} &= \int_{\Omega_I} \frac{\partial f}{\partial \mathcal{E}^e_{\alpha\beta}} \delta\mathcal{E}^e_{\alpha\beta} dV_I \\
&= \int_{\Omega_L} \frac{\partial \xi_\alpha}{\partial X_I} \frac{\partial f}{\partial \mathcal{E}^e_{\alpha\beta}} \frac{\partial \xi_\beta}{\partial X_J} \delta\mathcal{E}_{IJ} J_g dV_L \\
&= \int_{\Omega_L} \frac{\partial f}{\partial \mathcal{E}_{IJ}} \delta\mathcal{E}_{IJ} J_g dV_L
\end{aligned} \tag{B.11}$$

Where J_g is the Jacobian of the map from the Lagrangian cofiguration to the grown, intermediate stress-free configuration. Note that

$$\delta\mathcal{E}^e_{\alpha\beta} = \frac{\partial \xi_\alpha}{\partial X_I} \frac{\partial \xi_\beta}{\partial X_J} \delta\mathcal{E}_{IJ} \tag{B.12}$$

since strain tensors are covariant objects and transform under changes of coordinates in the opposite way as stress tensors, which are contravariant objects. This is necessary since they must be contracted together to form the work done, a scalar quantity.

This shows the relationship between the Second Piola-Kirchoff stress tensor, defined as the work-conjugate of the elastic strain on the intermediate stress-free configuration, which we call $\Sigma_{\alpha\beta}$, and the stress tensor induced in the Lagrangian coordinate system, S_{IJ}. This relationship is given by:

$$S_{IJ} = \frac{\partial X_I}{\partial \xi_\alpha} \Sigma_{\alpha\beta} \frac{\partial X_J}{\partial \xi_\alpha} J_g \tag{B.13}$$

We can then similarly derive the Cauchy stress by transforming to the Eulerian configuration:

$$\begin{aligned}\delta\mathcal{F} &= \int_{\Omega_I} \frac{\partial f}{\partial \mathcal{E}^e_{\alpha\beta}} \delta\mathcal{E}^e_{\alpha\beta} d\Omega_I \\ &= \int_{\Omega_E} \frac{\partial \xi_\alpha}{\partial x_i} \frac{\partial f}{\partial \mathcal{E}^e_{\alpha\beta}} \frac{\partial \xi_\beta}{\partial x_j} \delta e_{ij} J_e^{-1} d\Omega_E \\ &= \int_{\Omega_E} \frac{\partial f}{\partial \mathcal{E}_{ij}} \delta e_{ij} J_e^{-1} d\Omega_E\end{aligned} \tag{B.14}$$

where e_{ij} can be seen to be the strain transformed to the Eulerian coordinates and thus is the analog of the Eulerian-Almansi finite strain tensor, the work-conjugate tensor to the Cauchy stress:

$$e_{ij} = \frac{1}{2}\left(\delta_{ij} - \frac{\partial X_K}{\partial x_i}\frac{\partial X_K}{\partial x_j}\right) \tag{B.15}$$

So we can write the Cauchy stress as follows:

$$\sigma_{ij} = J_e^{-1}\frac{\partial x_i}{\partial \xi_\alpha}\Sigma_{\alpha\beta}\frac{\partial x_j}{\partial \xi_\beta} = J_g^{-1}J_e^{-1}\frac{\partial x_i}{\partial X_I}S_{IJ}\frac{\partial x_j}{\partial X_J} \tag{B.16}$$

We can see that these formalisms must describe the same physics by understanding that they provide different interpretations of the same elastic free energy function. In the morphoelasticity formalism, the energy is usually expressed in terms of the totally elastic strain $\mathcal{E}^e_{\alpha\beta}$. Then the Saint Venant-Kirchoff elastic free energy is given by:

$$f(\mathcal{E}^e_{\alpha\beta}) = \frac{\lambda}{2}\mathcal{E}^{e2}_{\alpha\alpha} + \mu\mathcal{E}^{e2}_{\alpha\beta} \tag{B.17}$$

In the target metric formalism the total strain $\mathcal{E}$ is the fundamental strain tensor. The energy is still considered to be a function on the intermediate configuration (and therefore a function of the elastic strain $\mathcal{E}^e_{\alpha\beta}$), and thus it is necessary to represent the energy function in terms of the tangent maps in addition to the total strain $\mathcal{E}_{IJ}$. It therefore becomes convenient to express the elastic free energy density in terms of an elasticity tensor $A_{\alpha\beta\delta\gamma}$ [45]:

$$f(\mathcal{E}^e_{\alpha\beta}) = A_{\alpha\beta\delta\gamma}\mathcal{E}^e_{\alpha\beta}\mathcal{E}^e_{\delta\gamma} = \frac{1}{2}\left(\lambda\delta_{\alpha\beta}\delta_{\delta\gamma} + \mu\left(\delta_{\alpha\gamma}\delta_{\beta\delta} + \delta_{\alpha\delta}\delta_{\beta\gamma}\right)\right)\mathcal{E}^e_{\alpha\beta}\mathcal{E}^e_{\delta\gamma} \tag{B.18}$$

In order to represent this energy in the target metric formalism, in terms of the total strain, it is necessary to transform the elasticity tensor to an elasticity tensor $\tilde{A}_{IJKL}$ in the Lagrangian

configuration:

$$\tilde{A}_{IJLK} = \frac{\partial X_I}{\partial \xi_\alpha}\frac{\partial X_J}{\partial \xi_\beta}\frac{\partial X_K}{\partial \xi_\delta}\frac{\partial X_L}{\partial \xi_\gamma}A_{\alpha\beta\delta\gamma} \tag{B.19}$$

It is then possible to represent this same elastic free energy density in the Lagrangian configuration in terms of the inverse target metric $\bar{g}^{-1}_{IJ} = (\partial X_J/\partial \xi_\beta)(\partial X_I/\partial \xi_\beta)$:

$$f(\mathcal{E}_{IJ}) = \tilde{A}_{IJLK}\mathcal{E}_{IJ}\mathcal{E}_{KL} = \frac{1}{2}\left(\lambda \bar{g}^{-1}_{IJ}\bar{g}^{-1}_{KL} + \mu\left(\bar{g}^{-1}_{IK}\bar{g}^{-1}_{JL} + \bar{g}^{-1}_{IL}\bar{g}^{-1}_{JK}\right)\right)\mathcal{E}_{IJ}\mathcal{E}_{KL} \tag{B.20}$$

Once this elastic free energy density is defined on the Lagrangian configuration it is possible to derive the equations of equilibrium by demanding that the variation of the elastic free energy with respect to the configuration $x_i(X_I)$ vanish:

$$\begin{aligned} 0 =& \frac{\delta \mathcal{F}}{\delta x_i(X_I)} = \int \frac{\delta w(\mathcal{E}_{IJ})}{\delta x_i(X_I)} J_g d\Omega_L = \int \frac{\partial w(\mathcal{E}_{IJ})}{\partial \mathcal{E}_{IJ}}\frac{\delta \mathcal{E}_{IJ}}{\delta x_i(X_I)} J_g d\Omega_L \\ =& \int \frac{1}{2}\left[\frac{\partial x_j}{\partial X_J}\frac{\partial}{\partial X_I}\delta(X_I - X'_I) + \frac{\partial x_i}{\partial X_I}\frac{\partial}{\partial X_J}\delta(X_J - X'_J)\right]\frac{\partial w(\mathcal{E}_{IJ})}{\partial \mathcal{E}_{IJ}} J_g d\Omega_L \\ =& \frac{\partial}{\partial X_I}\left(\frac{\partial x_j}{\partial X_J}\frac{\partial w(\mathcal{E}_{\mathcal{I}\mathcal{J}})}{\partial \mathcal{E}_{IJ}} J_g\right) \end{aligned} \tag{B.21}$$

This can then be compared to the prescription commonly given by morphoelasticity, a definition for the Cauchy stress as a derivative of an energy density:

$$\sigma_{ij} = J_e^{-1}\frac{\partial x_i}{\partial \xi_\alpha}\frac{\partial x_j}{\partial \xi_\beta}\frac{\partial w}{\partial \mathcal{E}^e_{\alpha\beta}} \tag{B.22}$$

The equilibrium equations are then defined by the condition that $\partial_i \sigma_{ij} = 0$. In order to compare these we will need to transform the divergence in the Eulerian configuration to one in the Lagrangian configuration, not only transforming the derivative operator in accordance with the chain rule but also transforming the vector index it contracts with to one in the

Lagrangian configuration, by using a Piola transform:

$$\begin{aligned} 0 =& \frac{\partial}{\partial x_i}\sigma_{ij} \\ \implies 0 =& \frac{\partial}{\partial X_I}\left(J\frac{\partial X_I}{\partial x_i}\sigma_{ij}\right) \\ 0 =& \frac{\partial}{\partial X_I}\left(J\frac{\partial X_I}{\partial x_i}J_e^{-1}\frac{\partial x_i}{\partial \xi_\alpha}\frac{\partial x_j}{\partial \xi_\beta}\frac{\partial w}{\partial \mathcal{E}^e_{\alpha\beta}}\right) \\ =& \frac{\partial}{\partial X_I}\left(\frac{\partial x_j}{\partial X_J}\frac{\partial w(\mathcal{E}_{\mathcal{I}\mathcal{J}})}{\partial \mathcal{E}_{IJ}}J_g\right) \end{aligned} \tag{B.23}$$

which can be seen to be the same is the equilbrium equation found by varying the energy defined using the target metric formalism.

B.1.2 Linearization

Having defined the nonlinear theory necessary for describing growth in an elastic material we may now derive the linearized elasticity described in the main text. Since we are concerned with the limit of nearly uniform growth we will consider growth locally as a uniform, isotropic component $\bar{\eta}$ with small, nonuniform and potentially anisotropic perturbations $\tilde{\eta}_{I\alpha}$ and define the growth map and target metric as follows:

$$\bar{g}_{IJ} = \partial_I\xi_\alpha\partial_J\xi_\alpha = \left(\bar{\eta}\delta_{I\alpha} + \tilde{\eta}_{I\alpha}\right)\left(\bar{\eta}\delta_{J\alpha} + \tilde{\eta}_{J\alpha}\right) \equiv \bar{\eta}^2\left(\delta_{IJ} + \frac{2}{\bar{\eta}}\tilde{\eta}_{IJ} + \frac{\tilde{\eta}_{I\alpha}\tilde{\eta}_{J\alpha}}{\bar{\eta}^2}\right) = \bar{\eta}^2\delta_{IJ} + 2\bar{\eta}\tilde{\eta}_{IJ} + \mathcal{O}(\epsilon^2) \tag{B.24}$$

where we have defined $\tilde{\eta}_{IJ} = \tilde{\eta}_{I\alpha}\delta_{J\alpha} + \tilde{\eta}_{J\alpha}\delta_{I\alpha}$, and assumed that the nonuniform $\tilde{\eta}$ is of order $\epsilon \ll 1$ compared to the uniform, isotropic growth $\bar{\eta}$:

$$\frac{\tilde{\eta}_{IJ}}{\bar{\eta}} = \mathcal{O}(\epsilon) \tag{B.25}$$

We will also take $\bar{\eta}$ as the total average growth, such that the average, as defined in equation 3.1, of $\tilde{\eta}_{IJ}$ over the disk is traceless:

$$\langle\tilde{\eta}_{KK}\rangle = 0 \tag{B.26}$$

We define the deformation as some small displacement w_I about uniform growth:

$$x_i(X_I) = \bar{\eta}X_I + w_I \tag{B.27}$$

Then the linearized strain takes the following form:

$$\begin{aligned}\mathcal{E}_{IJ} =&\frac{1}{2}(\partial_I x_k \partial_J x_k - \bar{g}_{IJ})\\ =&\frac{1}{2}\left[\left(\bar{\eta}\delta_{IJ} + \partial_I w_K\right)\left(\bar{\eta}\delta_{JK} + \partial_J w_K\right) - \bar{\eta}^2\left(\delta_{IJ} + \frac{2}{\bar{\eta}}\tilde{\eta}_{IJ} + \frac{\tilde{\eta}_{I\alpha}\tilde{\eta}_{J\alpha}}{\bar{\eta}^2}\right)\right]\\ =&\frac{\bar{\eta}}{2}\left(\partial_J w_I + \partial_I w_J\right) - \bar{\eta}\tilde{\eta}_{IJ} + \mathcal{O}(\epsilon^2)\\ \simeq&\bar{\eta}(w_{IJ} - \tilde{\eta}_{IJ})\end{aligned} \tag{B.28}$$

We then choose a Saint Venant-Kirchoff strain energy. This strain energy is properly considered a function on the intermediate configuration Ω_I, and thus we must define it not only in terms of the strain $\mathcal{E}_{IJ}$, but also in terms of the inverse target metric $\bar{g}^{-1}_{IJ}$ (see equation B.20), which is defined such that $\bar{g}_{IJ}\bar{g}^{-1}_{JK} = \delta_{IK}$:

$$f(\mathcal{E}_{IJ}) = \frac{\lambda}{2}(w_{KK} - \tilde{\eta}_{KK}) + \mu(w_{IJ} - \tilde{\eta}_{IJ})^2 + \mathcal{O}(\epsilon) \tag{B.29}$$

This energy density is related to the linearized Cauchy stress σ_{ij} (dropping the distinction between indices in different spaces for simplicity)via the principle of virtual work, with a force F_i, a virtual displacement δw_i and Eulerian and Lagrangian volumes v and V, respectively:

$$\begin{aligned}\delta\mathcal{F} =& \int F_i \delta w_i dv = \int \frac{\partial \sigma_{ij}}{\partial x_j}\delta w_i dv = \frac{1}{\bar{\eta}}\int \frac{\sigma_{ij}}{\partial X_j}\delta w_i |\partial_i x_k| dV\\ =& \bar{\eta}\int \frac{\partial \sigma_{ij}}{\partial X_j}\delta w_i dV + \mathcal{O}(\epsilon^3) = -\bar{\eta}\int \sigma_{ij}\delta\frac{\partial w_i}{\partial X_j}dV = -\bar{\eta}\int \sigma_{ij}\delta w_{ij} dV\end{aligned} \tag{B.30}$$

Thus we identify

$$\bar{\eta}\sigma_{ij} = \frac{\partial f}{\partial w_{ij}} \implies \sigma_{ij} = \frac{1}{\bar{\eta}}\frac{\partial f}{\partial w_{ij}} = \frac{1}{\bar{\eta}}\lambda\left(w_{kk} - \tilde{\eta}_{kk}\right)\delta_{ij} + 2\mu\left(w_{ij} - \tilde{\eta}_{ij}\right) \tag{B.31}$$

The linearized equilibrium equations are then given by:

$$\partial_i \sigma_{ij} = 0 \tag{B.32}$$

Expressed in terms of the linearized displacement $\vec{w}$ the equilibrium equations take the form:

$$(\lambda + 2\mu)\partial_j\partial_k w_k - \mu\epsilon_{jik}\epsilon_{kmn}\partial_i\partial_m w_n = \lambda\partial_j\tilde{\eta}_{kk} + 2\mu\partial_i\tilde{\eta}_{ij} \tag{B.33}$$

which is equivalent to the standard Cauchy-Navier equation of linear elasticity with an active stress. In the case where $\tilde{\eta}_{ij} = \tilde{\eta}\delta_{ij}$ we find a body force with potential $-\tilde{\eta}$, familiar from thermoelasticity [14]. This can be seen to describe linear elasticity with active stresses around a coordinate system uniformly scaled by $\bar{\eta}$, with the $\bar{\eta}^{-1}$ scaling in the Cauchy stress relating to the . This also demonstrates why we choose the limit that $\tilde{\eta}/\bar{\eta} \ll 1$ rather than simply $\tilde{\eta} \ll 1$, since $\tilde{\eta}/\bar{\eta}$ is the quantity that appears in the Cauchy stress.

B.1.3 Non-axisymmetric growth

In the non-axisymmetric case the equations of equilibrium cannot be directly integrated and a different approach is necessary. Since the system is in 2D and elastic equilibrium is still defined by $\partial_i \sigma_{ij} = 0$, the standard Airy stress function formalism is useful. We introduce the Airy stress function $\phi(\vec{X})$ as follows:

$$\sigma_{xx} = \frac{\partial^2 \phi}{\partial y^2}; \quad \sigma_{yy} = \frac{\partial^2 \phi}{\partial x^2}; \quad \sigma_{xy} = \sigma_{yx} = -\frac{\partial^2 \phi}{\partial x \partial y} \tag{B.34}$$

From here we can invert the linearized stress-strain relation to express the elements of the strain in terms of $\tilde{\eta}$ and ϕ:

$$\begin{aligned} w_{xx} &= \tilde{\eta}_{xx} + \frac{1}{4\mu(\lambda+\mu)}\left((\lambda+2\mu)\frac{\partial^2\phi}{\partial y^2} - \lambda\frac{\partial^2\phi}{\partial x^2}\right) \\ w_{yy} &= \tilde{\eta}_{yy} + \frac{1}{4\mu(\lambda+\mu)}\left((\lambda+2\mu)\frac{\partial^2\phi}{\partial x^2} - \lambda\frac{\partial^2\phi}{\partial y^2}\right) \\ w_{xy} &= \tilde{\eta}_{xy} - \frac{1}{2\mu}\frac{\partial^2\phi}{\partial x \partial y} \end{aligned} \tag{B.35}$$

If we then combine these expressions for w_{ij} with the compatability condition, which ensures that w_{ij} can be written as a symmetrized gradient (i.e. that there exists a displacement vector w_i such that $w_{ij} = 1/2(\partial_i w_j + \partial_j w_i)$) [14]:

$$0 = \frac{\partial^2 w_{xx}}{\partial y^2} - 2\frac{\partial^2 w_{xy}}{\partial x \partial y} + \frac{\partial^2 w_{yy}}{\partial x^2} \tag{B.36}$$

to arrive at the non-homogeneous biharmonic equation governing ϕ:

$$\nabla^4 \phi = -\frac{4\mu(\lambda+\mu)}{\lambda+2\mu}\left(\frac{\partial^2 \tilde{\eta}_{xx}}{\partial y^2} - 2\frac{\partial^2 \tilde{\eta}_{xy}}{\partial x \partial y} + \frac{\partial^2 \tilde{\eta}_{yy}}{\partial x^2}\right) \tag{B.37}$$

In the case of isotropic $\tilde{\eta}$ this reduces to:

$$\nabla^4\phi = -\frac{4\mu(\lambda+\mu)}{\lambda+2\mu}\nabla^2\tilde{\eta} \tag{B.38}$$

Since isotropic and anisotropic growth both result in a non-homogeneous biharmonic equation for ϕ, the following results for the isotropic case can be directly generalized to the anisotropic case. Because of this we proceed with the isotropic case for simplicity. We begin by writing ϕ as a sum of particular and general solutions $\phi = \phi_p + \phi_g$. We choose ϕ_p such that we reproduce the result for the pressure in the axisymmetric case: $\nabla^2\phi_p \propto \tilde{\eta}$. The general solution, ϕ_g will then be chosen to match stress-free boundary conditions. Because we have chosen a circular domain as our Lagrangian configuration, the Michell solution [114] for the planar biharmonic equation gives a series solution for ϕ_g:

$$\begin{aligned}\phi_g =& R^3(A_1\cos\Theta + B_1\sin\Theta)\\ &+\sum_{n=2}^{\infty}\left(A_n r^{n+2} + C_n r^n\right)\cos(n\Theta)\\ &+\sum_{n=2}^{\infty}\left(B_n r^{n+2} + D_n r^n\right)\sin(n\Theta)\end{aligned} \tag{B.39}$$

where we have omitted the terms forbidden by the geometry of the disk, and the axially symmetric which is described by the main text. These are determined by the boundary conditions:

$$\sigma_{RR}(R_D,\Theta) = 0, \quad \sigma_{R\Theta}(R_D,\Theta) = 0 \tag{B.40}$$

This places boundary conditions on ϕ_g in terms of ϕ_p, or equivalently, $\tilde{\eta}$. Choosing $\nabla^2\phi_p \propto \tilde{\eta}$ results in the following expression for ϕ_p:

$$\begin{aligned}\phi_p(R,\Theta) \equiv& \sum_{n=0}^{\infty}\left(\cos(n\Theta)\phi_{n,a}(R) + \sin(n\Theta)\phi_{n,b}(R)\right)\\ =& \frac{4\mu(\lambda+\mu)}{\lambda+2\mu}\sum_{n=0}^{\infty}\left(\int_0^{\infty}\left(\cos(n\Theta)\frac{\hat{\tilde{\eta}}_{n,a}(k)}{k^2} + \sin(n\Theta)\frac{\hat{\tilde{\eta}}_{n,b}(k)}{k^2}\right)J_n(Rk)kdk\right)\end{aligned} \tag{B.41}$$

where the $\hat{\tilde{\eta}}$ are defined by

$$\tilde{\eta}(R,\Theta) = \sum_{n=0}^{\infty}\left(\int_0^{\infty}\left(\cos(n\Theta)\hat{\tilde{\eta}}_{n,a}(k) + \sin(n\Theta)\hat{\tilde{\eta}}_{n,b}(k)\right)J_n(Rk)kdk\right) \tag{B.42}$$

The boundary conditions then give the following values for the coefficients:

$$\begin{aligned} A_n =& \frac{1}{2R_D^{n+2}}\left((3n+1)\phi_{n,a}(R_D) - RD\frac{d\phi_{n,a}}{dR}(R_D)\right) \\ C_n =& \frac{1}{2R_D^{n+2}}\left(-3(n+1)\phi_{n,a}(R_D) + RD\frac{d\phi_{n,a}}{dR}(R_D)\right) \end{aligned} \tag{B.43}$$

and the values for B_n and D_n are the same, substituting $\phi_{n,b}$ for $\phi_{n,a}$. Combining these we arrive at the pressure for a non-axisymmetric, isotropic growth field:

$$\begin{aligned} p =& \frac{2\mu(\lambda+\mu)}{\bar{\eta}(\lambda+2\mu)}\left[\tilde{\eta}\right. \\ &\left. -\sum_{n=1}^{\infty}\left(2(n+1)\left(\frac{R}{R_D}\right)^n\int_0^{R_D}\left(\frac{R}{R_D}\right)(\sin(n\theta)\tilde{\eta}_{n,a}(R') + \cos(n\theta)\tilde{\eta}_{n,b}(R'))dR'\right)\right] \end{aligned} \tag{B.44}$$

B.1.4 Growth without stress

From the form of equation B.37, the biharmonic equation for ϕ, it is clear that if $\tilde{\eta}_{ij}$ satisfies the compatability condition

$$0 = \frac{\partial^2\tilde{\eta}_{xx}}{\partial y^2} - 2\frac{\partial^2\tilde{\eta}_{xy}}{\partial x\partial y} + \frac{\partial^2\tilde{\eta}_{yy}}{\partial x^2} \tag{B.45}$$

the biharmonic equation is homogeneous and, given stress-free boundary conditions, growth of this form will produce no stress. This is the anisotropic generalization of "harmonic growth", which is known to produce no stress [80]. To understand the source of this stress-free growth note that this condition implies that $\tilde{\eta}_{ij}$ can be written as the symmetrized gradient of a vector [14]:

$$\tilde{\eta}_{ij} = \frac{1}{2}\left(\partial_i\tilde{\eta}_j + \partial_j\tilde{\eta}_i\right) \tag{B.46}$$

Then if we choose the displacement $w_i = \tilde{\eta}_i$ the linearized stress is zero. This condition extends to the full nonlinear case as well, where the condition for $\bar{g}_{ij}$ to be written as a square gradient $\partial_i\bar{g}_k\partial_j\bar{g}_k$ is that the Riemannian curvature of the metric $\bar{g}$ must be zero, that is, that

$\bar{g}$ describes a flat metric, embeddable in Euclidean space. This notion of compatible growth can be found in early work on the introduction of growth to theories of elasticity [170] and is important for understanding the origin of stress due to growth. From this perspective, we can see that the requirement that growth occur without stress is equivalent to the statement that the intermediate stress-free "grown" configuration of the material is flat Euclidean space. In this case where growth is compatible with Euclidean space and it defines a deformation vector η_i it is possible for each material element to "follow" the displacement defined by the growth exactly, remaining in stress-free configuration. This is equivalent to taking $x_i = \eta_i$.

The presence of growth modes that do not produce stress raises potential problems for theories that rely on local feedback on stress to halt the growth of a tissue, let alone at a precise final size. Mechanical feedback was originally introduced to explain how growth could be uniform in the presence of nonuniform growth factors [166], and harmonic growth has been implicated in the growth of leaves [80] [7], suggesting that mechanical feedback can lead to cases where stress-free growth occurs. From the perspective of precise control of tissue size, though, this has the potential to present a problem. We note that in the case of linearized elasticity on a disk, these stress-free growth modes are all proportional to $\sin(n\theta)$ or $\cos(n\theta)$ and thus do not affect the final size, given by $\bar{\eta}$, since terms proportional to sin and cos have zero average over the disk. On the other hand, it is nontrivial for mechanical feedback models to be able to prevent these modes from growing due to random fluctuations, eventually making the linear approximation invalid and potentially affecting the total size of the disk. However, it is possible to control these models dynamically, for example via certain kinds of boundary conditions or interactions with morphogens.

B.2 Laplacian OR model

If γ is considered as a power series in p and its derivatives, the presence of a ∇p term could arise from a term such as $\nabla M_c \cdot \nabla p$ where M_c is some morphogen signaling the activation of gradient feedback. From this perspective, feedback proportional to the Laplacian of the pressure might be considered more generic. Laplacian feedback has many of the same characteristics of gradient feedback with symmetry properties that are valuable in some analytic contexts. We will see that, aside from some minor differences, the majority of the previous results follow. We define γ as follows:

$$\gamma = -\kappa p + \kappa c^2(r)\nabla^2 p + M(r) \tag{B.47}$$

As before we require the Laplacian feedback to operate only for $r > r_c$. As in the gradient case we define the Laplacian feedback stength in terms of the length scale c.

The jump condition can be derived in the same way as before:

$$\begin{aligned} 0 &= \lim_{\delta\to 0}\int_{r_c-\delta}^{r_c+\delta}\gamma dr = c^2\lim_{\delta\to 0}\int_{r_c-\delta}^{r_c+\delta}\Theta(r-r_c)\nabla^2 p(r)dr \\ &= \lim_{\delta\to 0} p'(r_c+\delta) - p'(r_c-\delta) \end{aligned} \tag{B.48}$$

So the first derivative of the pressure must be continuous at the boundary r_c. If the pressure is not continuous, the laplacian is not defined and the integral diverges even in the limit.

Since the Laplacian measures the curvature instead of simply the gradient it is necessary to change the form of the morphogen $M(r)$ in the exterior. In order for the fixed point condition to produce a valid pressure satisfying $\langle p\rangle = 0$ we must have $M(r > r_c) > M(r < r_c)$. As before we will choose $M(r)$ to be steplike:

$$M(r) = b\Theta(r-r_c) + 1 \tag{B.49}$$

where $b > 0$. Note that this morphogen distribution does not define a non-gradient model with a valid fixed point, since the morphogen distribution is not negative anywhere. This means that the weak feedback limit is singular, but since we are concerned primarily with the opposite limit this does not pose a problem. As before, a quasi-steady state exists where $\gamma = \langle\gamma\rangle$. It is defined by:

$$\frac{\tilde{\eta}_{qss}}{\bar{\eta}} = \begin{cases} \epsilon\left(1-\langle\gamma\rangle\right) & r < r_c \\ \frac{\epsilon}{c}\left[1(1+b-\langle\gamma\rangle) - r_c(b-2\langle\gamma\rangle)\left(I_1\left(\frac{r_c}{c}\right)K_0\left(\frac{r}{c}\right) + I_0\left(\frac{r}{c}\right)K_1\left(\frac{r_c}{c}\right)\right)\right] & r > r_c \end{cases} \tag{B.50}$$

where I_n and K_n are the modified Bessel functions of order n.

B.2.1 Fixed point

As before, the dynamics reduce to $\dot{\bar{\eta}} = \bar{\eta}\langle\gamma\rangle$ and the fixed point is determined by $\gamma = 0$. The fixed point is then given by

$$\frac{\tilde{\eta}^*}{\bar{\eta}^*} = \begin{cases} \epsilon & r < r_c \\ \epsilon\left(1-b+b\frac{r_c}{c}\left(I_1\left(\frac{r_c}{c}\right)K_0\left(\frac{r}{c}\right) + I_0\left(\frac{r}{c}\right)K_1\left(\frac{r_c}{c}\right)\right)\right) & r > r_c \end{cases} \tag{B.51}$$

Since c still sets the length scale the final size for strong feedback, $1 \gg z = r_c/c$, must still scale as $\bar{\eta}^* = z^{-1}\bar{\eta}^*_{-1} + \bar{\eta}^*_0 + \bar{\eta}^*_1 + \mathcal{O}(z^2)$. The fixed point distributions for different values of the feedback length scale c are shown in figure B.1 For weak feedback, the fixed

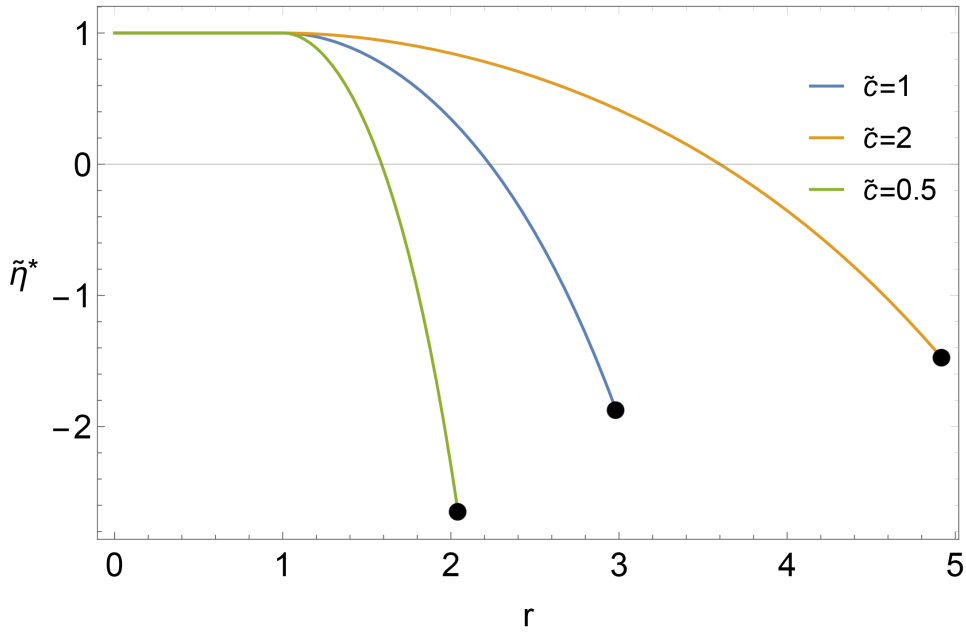

Figure B.1: The fixed point distributions for the OR model with Laplacian feedback, plotted for different values of $\tilde{c} = c/r_c$, in units with $r_c = 1$. The size of the disk for each trace is indicated by a black dot. The traces for each distribution end at the final size of the disks they describe, calculated by the condition that $\langle\tilde{\eta}^*\rangle = 0$. If the Laplacian feedback strength is weak, $\tilde{c} \ll 1$, then the steady state distribution has a sharp gradient, since the weak-feedback limit is singular. For strong Laplacian feedback with $\tilde{c} \gg 1$, the gradients of the steady-state distribution are much less sharp and the size of the disk is set by the feedback strength rather than the cutoff distance.

point distribution has a very sharp divergence and $\bar{\eta}^*$ scales differently. This is because the Laplacian model does not reduce to an OR model with a valid fixed point, and therefore does not stop growing. For small $\tilde{c}$ the disk must then overgrow dramatically and then apoptose down to the fixed point.

The fixed point condition can be simplified as follows:

$$\begin{aligned} 0 &= \langle \gamma \rangle \\ \langle M \rangle &= -\frac{c^2}{\epsilon} \left\langle \Theta(r - r_c) \frac{\nabla^2 \tilde{\eta}}{\bar{\eta}} \right\rangle \\ 1 + b\left(1 - \frac{1}{\bar{\eta}^{*2}}\right) &= \frac{2bz\epsilon}{\bar{\eta}^*} \left(I_1(z)K_1(z\bar{\eta}^*) - I_1(\bar{\eta}^*)K_1(z)\right) \end{aligned} \tag{B.52}$$

Then each side can be expanded for small z, and the values of $\bar{\eta}_i^*$ can be determined by matching terms. The lowest order is as follows:

$$\bar{\eta}_{-1}^*(1 + b) = 2bI_1(\bar{\eta}_{-1}^*) \tag{B.53}$$

Because there is no requirement that b be small or large, the transcendental equation that describes $\bar{\eta}_{-1}^*$ cannot be simplified as in the gradient case. Since $\langle M \rangle$ has no term proportional to z while $-\frac{c^2}{\epsilon}\left\langle \Theta(r - r_c)\frac{\nabla^2\tilde{\eta}}{\bar{\eta}} \right\rangle$ does, we have $\bar{\eta}_0^* = 0$. Note also that this condition implies

$$\bar{\eta}_{-1}^* > 1 \tag{B.54}$$

The next correction, $\bar{\eta}_1^*$, is given by:

$$\bar{\eta}_1^* = \frac{1}{4I_2(\bar{\eta}_{-1}^*)} \left(-\frac{2}{\bar{\eta}_{-1}^*} + 2K_1(\bar{\eta}_{-1}^*) + I_1(\bar{\eta}_{-1}^*)(1 - 2\gamma + \log(4) + 2\log(z)) \right) \tag{B.55}$$

Where above γ is the Euler-Mascheroni constant.

B.2.2 Linear Stability

The linear stablility problem can now be addressed, beginning with defining $\delta\gamma$ and the jump condition for small perturbations.

$$\begin{aligned} \delta\gamma &= -\frac{1}{\epsilon}\left(\frac{\delta\tilde{\eta}}{\bar{\eta}^*} - \frac{\delta\bar{\eta}}{\bar{\eta}^*}\frac{\tilde{\eta}^*}{\bar{\eta}^*}\right) + \Theta(r - r_c)\frac{c^2}{\epsilon}\left(\frac{\nabla^2\delta\tilde{\eta}}{\bar{\eta}^*} - \frac{\delta\bar{\eta}}{\bar{\eta}^*}\frac{\nabla^2\tilde{\eta}^*}{\bar{\eta}^*}\right) + \delta r\delta(r - r_c)\left(b + \frac{c^2}{\epsilon}\frac{\nabla^2\tilde{\eta}^*}{\bar{\eta}}\right) \\ &= -\frac{1}{\epsilon}\frac{\delta\tilde{\eta}}{\bar{\eta}^*} + \Theta(r - r_c)\frac{c^2}{\epsilon}\frac{\nabla^2\delta\tilde{\eta}}{\bar{\eta}} + \frac{\delta\bar{\eta}}{\bar{\eta}^*}\left(M(r) + \frac{r_c b}{2}\delta(r - r_c)\right) \end{aligned} \tag{B.56}$$

The jump condition is then given by:

$$0 = \lim_{\delta\to 0}\int_{r_c-\delta}^{r_c+\delta} \delta\gamma dr \tag{B.57}$$

$$= \lim_{\delta\to 0}\int_{r_c-\delta}^{r_c+\delta} \left[\frac{c^2\Theta(r-r_c)}{\epsilon}\frac{\nabla^2\delta\tilde{\eta}}{\bar{\eta}^*} + \frac{\delta\bar{\eta}}{\bar{\eta}^*}r_c\delta(r-r_c)\left(b+\frac{c^2}{\epsilon}\left(-\frac{b\epsilon}{2c^2}\right)\right)\right]dr \tag{B.58}$$

$$= \lim_{\delta\to 0}\left[\frac{c^2}{2\epsilon\bar{\eta}^*}(\delta\tilde{\eta}'(r_c+\delta)-\delta\tilde{\eta}'(r_c-\delta)) + \frac{\delta\bar{\eta}}{\bar{\eta}^*}\frac{br_c}{2}\right] \tag{B.59}$$

As before, this jump condition cancels the singularity in $\delta\gamma$. The axisymmetric eigenvalue problem is defined by:

$$\begin{aligned}
\lambda\delta\bar{\eta} &= \bar{\eta}^*\langle\delta\gamma\rangle = \frac{c^2}{\epsilon}\left\langle\Theta(r-r_c)\nabla^2\delta\tilde{\eta}\right\rangle + \delta\bar{\eta}\left[1+b\left(1-\frac{1}{\bar{\eta}^{*2}}\right)\right] \\
\lambda\delta\tilde{\eta} &= \bar{\eta}^*\left(\delta\gamma - \langle\delta\gamma\rangle\right) \\
&= \begin{cases} -\frac{\delta\tilde{\eta}}{\epsilon} - \frac{c^2}{\epsilon}\left\langle\Theta(r-r_c)\nabla^2\delta\tilde{\eta}\right\rangle + \epsilon b\delta\bar{\eta}\left(\frac{1}{\bar{\eta}^{*2}}-1\right) & r<r_c \\ -\frac{\delta\tilde{\eta}}{\epsilon} + \frac{c^2}{\epsilon}\left(\Theta(r-r_c)\nabla^2\delta\tilde{\eta} - \left\langle\Theta(r-r_c)\nabla^2\delta\tilde{\eta}\right\rangle\right) + \frac{\epsilon b\delta\bar{\eta}}{\bar{\eta}^{*2}} & r>r_c \end{cases}
\end{aligned} \tag{B.60}$$

As for the gradient case, if we choose $\delta\bar{\eta}=0$ we find that $\delta\tilde{\eta}=0$ for $r>r_c$ and $\lambda=-1/\epsilon$, and for the rest of the spectrum we may analyze the equation for $\lambda\delta\bar{\eta}$. To do so the expression for $\delta\tilde{\eta}$ as a function of λ is necessary, defining $L=\sqrt{1+\lambda\epsilon}$, $z=r_c/c$ and $\rho=r/r_d$:

$$\delta\tilde{\eta} = \begin{cases} L^{-2}\left(\epsilon\delta\bar{\eta}b\left(1/\bar{\eta}^{*2}-1\right) - c^2\left\langle\Theta(r-r_c)\nabla^2\delta\tilde{\eta}\right\rangle\right) & r<r_c \\ \bar{\eta}^{*-2}L^{-2}[-\bar{\eta}^{*2}c^2\left\langle\Theta(r-r_c)\nabla^2\delta\tilde{\eta}\right\rangle & \\ \quad +b\delta\bar{\eta}\epsilon\bar{\eta}^{*2}((I_1(Lz)-LzI_0(Lz))K_0(Lz\bar{\eta}^*\rho) & r>rc \\ \qquad\qquad +(LzK_0(Lz)+K_1(Lz))I_0(Lz\bar{\eta}^*\rho))] & \end{cases} \tag{B.61}$$

The average $c^2\left\langle\Theta(r-r_c)\nabla^2\delta\tilde{\eta}\right\rangle$ can be calculated self-consistently. In the limit of $z\to 0$ it takes the following form:

$$c^2\left\langle\Theta(r-r_c)\nabla^2\delta\tilde{\eta}\right\rangle = -\frac{2b\delta\bar{\eta}\epsilon I_1(\bar{\eta}^*_{-1}L)}{\bar{\eta}^*_{-1}L} \tag{B.62}$$

Plugging this into the eigenvalue equation $\lambda\delta\bar{\eta}=\bar{\eta}^*\delta\gamma$ all of the zero order terms in z and ϵ are eliminated by the fixed point condition and the resulting eigenvalue problem to lowest

order in z and ϵ is as follows:

$$\lambda = \frac{2bz^2}{\bar{\eta}^*_{-1}}\left(1 - \bar{\eta}^*_{-1}(K_1(\bar{\eta}^*_{-1}) + I_1(\bar{\eta}^*_{-1})(\gamma + \log(z/2)))\right) - b\epsilon I_2(\bar{\eta}^*_{-1}) + \mathcal{O}(\epsilon^2, z^4, (\epsilon z)^2) \quad \text{(B.63)}$$

If the Laplacian feedback is not substantially weaker than the normal proportional feedback this is negative, indicating that the axisymmetric modes are stable. For the non-axisymmetric problem we define $\tilde{\rho} = r/r_d$.

For non-axisymmetric modes it is sufficient to analyze the stability of a single harmonic $\delta\eta_n = e^{in\theta}\delta\eta_{n,r}(\rho)$. As before $\delta\bar{\eta} = 0$ so $\delta\eta_n = \delta\tilde{\eta}_n$. We substitute $L = \sqrt{1+\epsilon\lambda}$, $\rho = r/r_d$, and $z = r_c/c$. The eigenvalue problem is then:

$$z^2L^2\bar{\eta}^{*2}\delta\eta_n - \Theta(r - r_c)\nabla^2\delta\eta_n = 2(n+1)\tilde{I}\rho^n z^2\bar{\eta}^{*2}e^{in\theta} \quad \text{(B.64)}$$

Again, for $r < r_c$, modes where $\tilde{I}$ vanishes have $\tilde{\lambda} = 0$ or $\lambda = -1/\epsilon$. For modes with $\tilde{I} \neq 0$ the situation is also fairly straightforward. For $r < r_c$ these modes have the form:

$$\delta\eta_n = \frac{2(n+1)}{L^2}\tilde{I}\rho^n \quad \text{(B.65)}$$

for $r > r_c$ the eigenvalue problem is expressed as:

$$(\nabla^2 - \bar{\eta}^{*2}z^2)\delta\eta = \bar{\eta}^{*2}z^2\tilde{I}2(n+1)\rho^n \quad \text{(B.66)}$$

If we choose a trial function of the form:

$$\delta\eta_n = \alpha_1 I_n(\rho) + \alpha_2 K_n(\rho) + \alpha_3\rho^n \quad \text{(B.67)}$$

This solves the eigenvalue problem, with the three α_i matching the ρ^n term for $r > r_c$ and matching the two boundary conditions. The integral factor $\tilde{I}$ then simply sets the scale of $\delta\eta_n$. The eigenvalue is determined by:

$$\begin{aligned} L^2\bar{\eta}^{*2}z^2 &= 1 \\ \lambda\epsilon &= \frac{1}{\bar{\eta}^{*2}_{-1}} - 1 + \mathcal{O}(z^2) \end{aligned} \quad \text{(B.68)}$$

Since we have $\bar{\eta}^*_{-1} > 1$, we have $\lambda < 0$ and thus the rest of the spectrum is stable, aside from the $\lambda = 0$ modes of the form $\delta\eta_n \propto r^n$, leading to $\delta p = 0$ arising from "compatible growth" as discussed earlier.

B.3 AND model predicts disk size depends on feedback strength

For the ODEs describing the dynamics of the AND model it is possible to see that since the strong feedback limit does not decouple the dynamics $\bar{\eta}$ and $\tilde{\eta}$, the dynamics of $\bar{\eta}$ will depend strongly on ϵ. We proceed by deriving a relation describing the integral curves for the ODE model. From equations 3.24 & 3.25 we find the integral curve condition:

$$\frac{\partial \dot{\bar{\eta}}}{\partial \dot{\tilde{\eta}}} = \frac{1}{\bar{\eta}^2 - 1} \tag{B.69}$$

Integrating, we find:

$$\tilde{\eta} = \bar{\eta}\left(\frac{\bar{\eta}^2}{3} - 1\right) + C \tag{B.70}$$

where C is a constant of integration. With the initial conditions $\bar{\eta}(0) = 1$ and $\tilde{\eta}(0) = 0$ this gives:

$$\tilde{\eta} = \frac{\bar{\eta}}{3}\left(\bar{\eta}^2 - 3 + \frac{2}{\bar{\eta}}\right) \tag{B.71}$$

Combining this with 3.24 gives

$$\dot{\bar{\eta}} = \frac{1}{\epsilon\bar{\eta}}\left(1 - \frac{\bar{\eta}^2}{3} - \frac{2}{3\bar{\eta}}\right) + \frac{1}{\bar{\eta}} \tag{B.72}$$

It is also possible to estimate the final size reached by following this integral curve. Comparing B.71 with the fixed point condition 3.26 gives a cubic equation for $\bar{\eta}^*(\epsilon)$, which only has one solution satisfying $\bar{\eta}^* > 1$. For $\epsilon \ll 1$ this is:

$$\bar{\eta}^* = 1 + \sqrt{\epsilon} + \frac{\epsilon}{3} \tag{B.73}$$

So we can see that in the AND model the final size of the disk depends strongly on the strength of the pressure feedback.

B.4 Exact calculations for the AND model

In the AND model it is possible to carry out the reduction to and ODE as well as derive the primary results from the linear stability without truncating powers of ϵ. In reducing to the ODE model the only point at which low order in ϵ came in was in the average $\langle\gamma\eta\rangle$. This

can be carried out exactly as follows:

$$\begin{aligned}
\langle\gamma\eta\rangle &= \left\langle \Theta(r_c - r)\left(1 - \frac{1}{\epsilon}\frac{\tilde{\eta}_{in}}{\bar{\eta}}\right)(\bar{\eta} + \tilde{\eta})\right\rangle \\
&= \left(1 - \frac{1}{\epsilon}\frac{\tilde{\eta}_{\text{in}}}{\bar{\eta}}\right)\frac{2}{R_D^2}\int_0^{R_c} R' dR' \\
&= \left(1 - \frac{1}{\epsilon}\frac{\tilde{\eta}_{\text{in}}}{\bar{\eta}}\right)\frac{R_c^2}{R_D^2} \\
&= \left(1 - \frac{1}{\epsilon}\frac{\tilde{\eta}_{\text{in}}}{\bar{\eta}}\right)\frac{r_c^2}{R_D^2(\bar{\eta} + \tilde{\eta}\frac{\lambda+\mu}{\lambda+2\mu})} \\
&= \left(1 - \frac{1}{\epsilon}\frac{\tilde{\eta}_{\text{in}}}{\bar{\eta}}\right)\frac{1}{\bar{\eta} + \tilde{\eta}_{\text{in}}\frac{\lambda+\mu}{\lambda+2\mu}}
\end{aligned} \tag{B.74}$$

This simply modifies the prefactor of $\langle\gamma\eta\rangle$, and the full dynamical equations are otherwise identical to equations 3.24 and 3.25. Because of this, taking the limit of small ϵ has no effect on the fixed point structure, which is still determined by $\gamma = 0$. This has no effect on the linear stability problem for the same reason.

B.5 Soft modes for non-axisymmetric morphogen distribution

It is clear that there are growth modes that generate zero stress. These manifest themselves in the linear stability of the non-axisymmetric problem, leading to $\lambda = 0$ modes which could be driven by noise to eventually generate large displacements inconsistent with the linear elastic approximation. This does not occur in the axisymmetric model due to contributions from the morphogen. In particular, for the axisymmetric problem, the zero mode is given by uniform growth. In the linear stability problem this is described by $\delta\tilde{\eta} = 0$. Since $\delta\gamma$ has contribtions from the morphogen as well as from $\delta\eta$ this does not produce a valid zero mode, or even a valid solution of the eigenvalue problem. Such a phenomenon also operates in the non-axisymmetric problem.

Considering a general OR model, with

$$\delta\gamma = f[\delta p(r,\theta)] + \delta M(r,\theta) \tag{B.75}$$

where f is a general functional of δp potentially including gradient or Laplacian feedback.

We require $f[0] = 0$, as in all the examples we have treated. The problem of looking for soft $\lambda = 0$ modes is, as before, the problem of finding $\delta\gamma = 0$. If $\delta\eta$ takes the form of compatible growth ($\nabla^2\delta\eta = 0$ for the isotropic case), then we have $\delta p = 0$ this gives

$$0 = \delta\gamma = 0 + \delta M(r, \theta) \tag{B.76}$$

This shows that the $\nabla^2\delta\eta = 0$ modes are no longer solutions to the eigenvalue problem. While this does not itself prohibit $\lambda = 0$ modes it does imply that the $\nabla^2\delta\eta = 0$ modes are not valid solutions to the eigenvalue problem. In particular, this emphasizes that the distribution of the morphogen plays an important role in controlling $\lambda = 0$ modes and suggests that for a non-axisymmetric $M(r, \theta)$ the non-axisymmetric zero modes are forbidden in the same way as they are for the axisymmetric problem.

B.6 Feedback on the full stress tensor

Posing the problem of growth control by mechanical feedback on the full stress tensor poses difficulties that do not arise in the isotropic case. Consider a simple OR type model, but with $\gamma \to \gamma_{ij}$, a symmetric tensor, as follows:

$$\gamma_{ij} = -\frac{1}{\epsilon}\sigma_{ij} + M_{ij} \tag{B.77}$$

where M_{ij} is a tensor formed from morphogen distributions, perhaps as $M(x_k)\delta_{ij}$ or $\partial_i\partial_j M(x_k)$. Defining a fixed point for the dynamics with no net tissue flux then requires $\gamma_{ij} = 0$. This gives a steady state stress:

$$\sigma^*_{ij} = \epsilon M_{ij} \tag{B.78}$$

But the elastic equilibrium also places constraints on $\partial_i\sigma_{ij}$, specifically that $\partial_i\sigma_{ij} = 0$. This implies that at steady state we must have

$$\partial_i M_{ij} = 0 \tag{B.79}$$

The condition $\partial_i\sigma_{ij} = 0$ places constraints on any chosen form for γ_{ij} at steady state. This could still be managed if the morphogen distributions underlying M_{ij} had dynamics that reproduced the relevant condition at their own steady state, placing tight constraints on the coupling between the stress, growth, and morphogen dynamics. The other alternative is that feedback on the traceless component of the stress is minimal.

Bibliography

[1] T. Aegerter-Wilmsen, C. M. Aegerter, E. Hafen, and K. Basler. Model for the regulation of size in the wing imaginal disc of drosophila. *Mech Dev*, 124(4):318–26, 2007.

[2] T. Aegerter-Wilmsen, M. B. Heimlicher, A. C. Smith, P. B. de Reuille, R. S. Smith, C. M. Aegerter, and K. Basler. Integrating force-sensing and signaling pathways in a model for the regulation of wing imaginal disc size. *Development*, 139(17):3221–31, 2012.

[3] S. Akiyama. Structural and dynamic aspects of protein clocks: how can they be so slow and stable? *Cell Mol Life Sci*, 69(13):2147–60, 2012.

[4] T. Akiyama and M. C. Gibson. Decapentaplegic and growth control in the developing drosophila wing. *Nature*, 527(7578):375–8, 2015.

[5] C. Alexandre, A. Baena-Lopez, and J. P. Vincent. Patterning and growth control by membrane-tethered wingless. *Nature*, 505(7482):180–5, 2014.

[6] M. Aliee, J. C. Roper, K. P. Landsberg, C. Pentzold, T. J. Widmann, F. Julicher, and C. Dahmann. Physical mechanisms shaping the drosophila dorsoventral compartment boundary. *Curr Biol*, 22(11):967–76, 2012.

[7] K. Alim, S. Armon, B. I. Shraiman, and A. Boudaoud. Leaf growth is conformal. *Phys Biol*, 13(5):05LT01, 2016.

[8] K. Alim, O. Hamant, and A. Boudaoud. Regulatory role of cell division rules on tissue growth heterogeneity. *Front Plant Sci*, 3:174, 2012.

[9] U. Alon, M. G. Surette, N. Barkai, and S. Leibler. Robustness in bacterial chemotaxis. *Nature*, 397(6715):168–71, 1999.

[10] D. Ambrosi, G. A. Ateshian, E. M. Arruda, S. C. Cowin, J. Dumais, A. Goriely, G. A. Holzapfel, J. D. Humphrey, R. Kemkemer, E. Kuhl, J. E. Olberding, L. A. Taber, and K. Garikipati. Perspectives on biological growth and remodeling. *J Mech Phys Solids*, 59(4):863–883, 2011.

[11] M. Amdaoud, M. Vallade, C. Weiss-Schaber, and I. Mihalcescu. Cyanobacterial clock, a stable phase oscillator with negligible intercellular coupling. *Proc Natl Acad Sci U S A*, 104(17):7051–6, 2007.

[12] D. S. Andersen, J. Colombani, and P. Leopold. Coordination of organ growth: principles and outstanding questions from the world of insects. *Trends Cell Biol*, 23(7):336–44, 2013.

[13] G. A. Babbitt. Inbreeding reduces power-law scaling in the distribution of fluctuating asymmetry: an explanation of the basis of developmental instability. *Heredity (Edinb)*, 97(4):258–68, 2006.

[14] J. R. Barber. *Elasticity*. Solid mechanics and its applications. Springer, Dordrecht ; New York, 3rd rev. edition, 2010.

[15] J. Bass and J. S. Takahashi. Circadian integration of metabolism and energetics. *Science*, 330(6009):1349–1354, 2010.

[16] D. Bell-Pedersen, V. M. Cassone, D. J. Earnest, S. S. Golden, P. E. Hardin, T. L. Thomas, and M. J. Zoran. Circadian rhythms from multiple oscillators: lessons from diverse organisms. *Nat Rev Genet*, 6(7):544–56, 2005.

[17] Martine Ben Amar and Alain Goriely. Growth and instability in elastic tissues. *Journal of the Mechanics and Physics of Solids*, 53(10):2284–2319, 2005.

[18] C. Bertet and T. Lecuit. Planar polarity and short-range polarization in drosophila embryos. *Semin Cell Dev Biol*, 20(8):1006–13, 2009.

[19] E. Boone, J. Colombani, D. S. Andersen, and P. Leopold. The hippo signalling pathway coordinates organ growth and limits developmental variability by controlling dilp8 expression. *Nat Commun*, 7:13505, 2016.

[20] F. Boudon, J. Chopard, O. Ali, B. Gilles, O. Hamant, A. Boudaoud, J. Traas, and C. Godin. A computational framework for 3d mechanical modeling of plant morphogenesis with cellular resolution. *PLoS Comput Biol*, 11(1):e1003950, 2015.

[21] C. Brettschneider, R. J. Rose, S. Hertel, I. M. Axmann, A. J. Heck, and M. Kollmann. A sequestration feedback determines dynamics and temperature entrainment of the kaiabc circadian clock. *Mol Syst Biol*, 6:389, 2010.

[22] C. J. Breuker, J. S. Patterson, and C. P. Klingenberg. A single basis for developmental buffering of drosophila wing shape. *PLoS One*, 1:e7, 2006.

[23] P. J. Bryant and P. Levinson. Intrinsic growth control in the imaginal primordia of drosophila, and the autonomous action of a lethal mutation causing overgrowth. *Dev Biol*, 107(2):355–63, 1985.

[24] Peter J. Bryant and Pat Simpson. Intrinsic and extrinsic control of growth in developing organs. *The Quarterly Review of Biology*, 59(4):387–415, 1984.

[25] D. E. Chang, S. Leung, M. R. Atkinson, A. Reifler, D. Forger, and A. J. Ninfa. Building biological memory by linking positive feedback loops. *Proc Natl Acad Sci U S A*, 107(1):175–80, 2010.

[26] Y. G. Chang, S. E. Cohen, C. Phong, W. K. Myers, Y. I. Kim, R. Tseng, J. Lin, L. Zhang, J. S. Boyd, Y. Lee, S. Kang, D. Lee, S. Li, R. D. Britt, M. J. Rust, S. S. Golden, and A. LiWang. Circadian rhythms. a protein fold switch joins the circadian oscillator to clock output in cyanobacteria. *Science*, 349(6245):324–8, 2015.

[27] Y. G. Chang, N. W. Kuo, R. Tseng, and A. LiWang. Flexibility of the c-terminal, or cii, ring of kaic governs the rhythm of the circadian clock of cyanobacteria. *Proc Natl Acad Sci U S A*, 108(35):14431–6, 2011.

[28] Y. G. Chang, R. Tseng, N. W. Kuo, and A. LiWang. Rhythmic ring-ring stacking drives the circadian oscillator clockwise. *Proc Natl Acad Sci U S A*, 109(42):16847–51, 2012.

[29] Y. G. Chang, R. Tseng, N. W. Kuo, and A. LiWang. Nuclear magnetic resonance spectroscopy of the circadian clock of cyanobacteria. *Integr Comp Biol*, 53(1):93–102, 2013.

[30] O. Chara, E. M. Tanaka, and L. Brusch. Mathematical modeling of regenerative processes. *Curr Top Dev Biol*, 108:283–317, 2014.

[31] Philippe G. Ciarlet. *Mathematical elasticity*. Studies in mathematics and its applications. North-Holland ; Sole distributors for the U.S.A. and Canada, Elsevier Science Pub. Co., Amsterdam ; New York New York, N.Y., U.S.A., 1988.

[32] S. Clodong, U. Duhring, L. Kronk, A. Wilde, I. Axmann, H. Herzel, and M. Kollmann. Functioning and robustness of a bacterial circadian clock. *Mol Syst Biol*, 3:90, 2007.

[33] E. Conrad, A. E. Mayo, A. J. Ninfa, and D. B. Forger. Rate constants rather than biochemical mechanism determine behaviour of genetic clocks. *J R Soc Interface*, 5 Suppl 1:S9–15, 2008.

[34] M. E. Csete and J. C. Doyle. Reverse engineering of biological complexity. *Science*, 295(5560):1664–9, 2002.

[35] M. Delarue, J. F. Joanny, F. Julicher, and J. Prost. Stress distributions and cell flows in a growing cell aggregate. *Interface Focus*, 4(6):20140033, 2014.

[36] C. Dibner, D. Sage, M. Unser, C. Bauer, T. d'Eysmond, F. Naef, and U. Schibler. Circadian gene expression is resilient to large fluctuations in overall transcription rates. *EMBO J*, 28(2):123–34, 2009.

[37] J. E. Dittmer, R. J. Goss, and C. E. Dinsmore. The growth of infant hearts grafted to young and adult rats. *Am J Anat*, 141(1):155–60, 1974.

[38] G. Dong and S. S. Golden. How a cyanobacterium tells time. *Curr Opin Microbiol*, 11(6):541–6, 2008.

[39] G. Dong, Y. I. Kim, and S. S. Golden. Simplicity and complexity in the cyanobacterial circadian clock mechanism. *Curr Opin Genet Dev*, 20(6):619–25, 2010.

[40] G. Dong, Q. Yang, Q. Wang, Y. I. Kim, T. L. Wood, K. W. Osteryoung, A. van Oudenaarden, and S. S. Golden. Elevated atpase activity of kaic applies a circadian checkpoint on cell division in synechococcus elongatus. *Cell*, 140(4):529–39, 2010.

[41] S. Donoughe and S. DiNardo. dachsous and frizzled contribute separately to planar polarity in the drosophila ventral epidermis. *Development*, 138(13):2751–9, 2011.

[42] W. Driever and C. Nusslein-Volhard. The bicoid protein determines position in the drosophila embryo in a concentration-dependent manner. *Cell*, 54(1):95–104, 1988.

[43] V. Dvornyk, H. W. Deng, and E. Nevo. Structure and molecular phylogeny of sasa genes in cyanobacteria: insights into evolution of the prokaryotic circadian system. *Mol Biol Evol*, 21(8):1468–76, 2004.

[44] S. Eaton and F. Julicher. Cell flow and tissue polarity patterns. *Curr Opin Genet Dev*, 21(6):747–52, 2011.

[45] E. Efrati, E. Sharon, and R. Kupferman. Elastic theory of unconstrained non-euclidean plates. *Journal of the Mechanics and Physics of Solids*, 57(4):762–775, 2009.

[46] Efi Efrati, Eran Sharon, and Raz Kupferman. The metric description of elasticity in residually stressed soft materials. *Soft Matter*, 9(34):8187, 2013.

[47] E. Emberly and N. S. Wingreen. Hourglass model for a protein-based circadian oscillator. *Phys Rev Lett*, 96(3):038303, 2006.

[48] C. Escudero. Stochastic resonance due to internal noise in reaction kinetics. *Phys Rev E Stat Nonlin Soft Matter Phys*, 74(1 Pt 1):010103, 2006.

[49] S. Etienne-Manneville. Neighborly relations during collective migration. *Curr Opin Cell Biol*, 30:51–9, 2014.

[50] R. Farhadifar, J. C. Roper, B. Aigouy, S. Eaton, and F. Julicher. The influence of cell mechanics, cell-cell interactions, and proliferation on epithelial packing. *Curr Biol*, 17(24):2095–104, 2007.

[51] Jr. Ferrell, J. E., T. Y. Tsai, and Q. Yang. Modeling the cell cycle: why do certain circuits oscillate? *Cell*, 144(6):874–85, 2011.

[52] Alfred Fessard. *Proprietes rythmiques de la matiere vivante*. Hermann & cie, Paris,, 1936.

[53] D. B. Forger. Signal processing in cellular clocks. *Proc Natl Acad Sci U S A*, 108(11):4281–5, 2011.

[54] P. Francois, V. Hakim, and E. D. Siggia. Deriving structure from evolution: metazoan segmentation. *Mol Syst Biol*, 3:154, 2007.

[55] T. Gao, X. Zhang, N. B. Ivleva, S. S. Golden, and A. LiWang. Nmr structure of the pseudo-receiver domain of cika. *Protein Sci*, 16(3):465–75, 2007.

[56] K. Garikipati. The kinematics of biological growth. *Applied Mechanics Reviews*, 62(3):030801, 2009.

[57] G. Gerisch, H. Fromm, A. Huesgen, and U. Wick. Control of cell-contact sites by cyclic-amp pulses in differentiating dictyostelium cells. *Nature*, 255(5509):547–549, 1975.

[58] A. Goldbeter. *Biochemical oscillations and cellular rhythms : the molecular bases of periodic and chaotic behaviour*. Cambridge University Press, Cambridge ; New York, 1996.

[59] A. Goldbeter. Computational approaches to cellular rhythms. *Nature*, 420(6912):238–45, 2002.

[60] B. C. Goodwin. Oscillatory behavior in enzymatic control processes. *Adv Enzyme Regul*, 3:425–38, 1965.

[61] A. Goriely and M. Ben Amar. On the definition and modeling of incremental, cumulative, and continuous growth laws in morphoelasticity. *Biomech Model Mechanobiol*, 6(5):289–96, 2007.

[62] Alain Goriely. *The mathematics and mechanics of biological growth*. Interdisciplinary applied mathematics,. Springer, New York, NY, 2017.

[63] A. E. Green and P. M. Naghdi. A general theory of an elastic-plastic continuum. *Archive for Rational Mechanics and Analysis*, 18(4), 1965.

[64] A. Gutu and E. K. O'Shea. Two antagonistic clock-regulated histidine kinases time the activation of circadian gene expression. *Mol Cell*, 50(2):288–94, 2013.

[65] B. Handke, J. Szabad, P. V. Lidsky, E. Hafen, and C. F. Lehner. Towards long term cultivation of drosophila wing imaginal discs in vitro. *PLoS One*, 9(9):e107333, 2014.

[66] E. Hannezo, J. Prost, and J. F. Joanny. Growth, homeostatic regulation and stem cell dynamics in tissues. *J R Soc Interface*, 11(93):20130895, 2014.

[67] I. K. Hariharan. Organ size control: Lessons from drosophila. *Dev Cell*, 34(3):255–65, 2015.

[68] S. Harmansa, F. Hamaratoglu, M. Affolter, and E. Caussinus. Dpp spreading is required for medial but not for lateral wing disc growth. *Nature*, 527(7578):317–22, 2015.

[69] R. G. Harrison. Some unexpected results of the heteroplastic transplantation of limbs. *Proceedings of the National Academy of Sciences*, 10(2):69–74, 1924.

[70] J. Hasty, A. Hoffmann, and S. Golden. Systems biology of cellular rhythms: from cacophony to symphony. *Curr Opin Genet Dev*, 20(6):571–3, 2010.

[71] I. Heemskerk, T. Lecuit, and L. LeGoff. Dynamic clonal analysis based on chronic in vivo imaging allows multiscale quantification of growth in the drosophila wing disc. *Development*, 141(11):2339–48, 2014.

[72] A. Herpin, C. Lelong, and P. Favrel. Transforming growth factor-beta-related proteins: an ancestral and widespread superfamily of cytokines in metazoans. *Dev Comp Immunol*, 28(5):461–85, 2004.

[73] B. Hess and A. Boiteux. Oscillatory phenomena in biochemistry. *Annu Rev Biochem*, 40:237–58, 1971.

[74] B. Hess and A. Boitewx. Oscillatory phenomena in biochemistry. *Annual Review of Biochemistry*, 40:237–, 1971.

[75] A. L. Hodgkin and A. F. Huxley. A quantitative description of membrane current and its application to conduction and excitation in nerve. *Journal of Physiology-London*, 117(4):500–544, 1952.

[76] L. Hufnagel, A. A. Teleman, H. Rouault, S. M. Cohen, and B. I. Shraiman. On the mechanism of wing size determination in fly development. *Proc Natl Acad Sci U S A*, 104(10):3835–40, 2007.

[77] R. A. Hut and D. G. Beersma. Evolution of time-keeping mechanisms: early emergence and adaptation to photoperiod. *Philos Trans R Soc Lond B Biol Sci*, 366(1574):2141–54, 2011.

[78] P. W. Ingham, Y. Nakano, and C. Seger. Mechanisms and functions of hedgehog signalling across the metazoa. *Nat Rev Genet*, 12(6):393–406, 2011.

[79] M. K. Iovine. Conserved mechanisms regulate outgrowth in zebrafish fins. *Nat Chem Biol*, 3(10):613–8, 2007.

[80] K. D. Irvine and B. I. Shraiman. Mechanical control of growth: ideas, facts and challenges. *Development*, 144(23):4238–4248, 2017.

[81] H. Ito, M. Mutsuda, Y. Murayama, J. Tomita, N. Hosokawa, K. Terauchi, C. Sugita, M. Sugita, T. Kondo, and H. Iwasaki. Cyanobacterial daily life with kai-based circadian and diurnal genome-wide transcriptional control in synechococcus elongatus. *Proc Natl Acad Sci U S A*, 106(33):14168–73, 2009.

[82] H. Iwasaki and T. Kondo. Circadian timing mechanism in the prokaryotic clock system of cyanobacteria. *J Biol Rhythms*, 19(5):436–44, 2004.

[83] H. Iwasaki, T. Nishiwaki, Y. Kitayama, M. Nakajima, and T. Kondo. Kaia-stimulated kaic phosphorylation in circadian timing loops in cyanobacteria. *Proc Natl Acad Sci U S A*, 99(24):15788–93, 2002.

[84] I. H. Jain, V. Vijayan, and E. K. O'Shea. Spatial ordering of chromosomes enhances the fidelity of chromosome partitioning in cyanobacteria. *Proc Natl Acad Sci U S A*, 109(34):13638–43, 2012.

[85] C. H. Johnson, T. Mori, and Y. Xu. A cyanobacterial circadian clockwork. *Curr Biol*, 18(17):R816–R825, 2008.

[86] C. C. Jolley, K. L. Ode, and H. R. Ueda. A design principle for a posttranslational biochemical oscillator. *Cell Rep*, 2(4):938–50, 2012.

[87] H. Kageyama, T. Nishiwaki, M. Nakajima, H. Iwasaki, T. Oyama, and T. Kondo. Cyanobacterial circadian pacemaker: Kai protein complex dynamics in the kaic phosphorylation cycle in vitro. *Mol Cell*, 23(2):161–71, 2006.

[88] N. A. Kaplan, P. F. Colosimo, X. Liu, and N. S. Tolwinski. Complex interactions between gsk3 and apkc in drosophila embryonic epithelial morphogenesis. *PLoS One*, 6(4):e18616, 2011.

[89] J. Keily, D. R. MacGregor, R. W. Smith, A. J. Millar, K. J. Halliday, and S. Penfield. Model selection reveals control of cold signalling by evening-phased components of the plant circadian clock. *Plant J*, 76(2):247–57, 2013.

[90] J. K. Kim and D. B. Forger. A mechanism for robust circadian timekeeping via stoichiometric balance. *Mol Syst Biol*, 8:630, 2012.

[91] Y. I. Kim, G. Dong, Jr. Carruthers, C. W., S. S. Golden, and A. LiWang. The day/night switch in kaic, a central oscillator component of the circadian clock of cyanobacteria. *Proc Natl Acad Sci U S A*, 105(35):12825–30, 2008.

[92] Y. Kitayama, H. Iwasaki, T. Nishiwaki, and T. Kondo. Kaib functions as an attenuator of kaic phosphorylation in the cyanobacterial circadian clock system. *Embo Journal*, 22(9):2127–2134, 2003.

[93] L. D. Landau, E. M. Lifshitz, Arnold Markovich Kosevich, and L. P. Pitaevskii. *Theory of elasticity*. Course of theoretical physics. Pergamon Press, Oxford Oxfordshire ; New York, 3rd english edition, 1986.

[94] K. P. Landsberg, R. Farhadifar, J. Ranft, D. Umetsu, T. J. Widmann, T. Bittig, A. Said, F. Julicher, and C. Dahmann. Increased cell bond tension governs cell sorting at the drosophila anteroposterior compartment boundary. *Curr Biol*, 19(22):1950–5, 2009.

[95] T. Lecuit, W. J. Brook, M. Ng, M. Calleja, H. Sun, and S. M. Cohen. Two distinct mechanisms for long-range patterning by decapentaplegic in the drosophila wing. *Nature*, 381(6581):387–93, 1996.

[96] T. Lecuit and L. Le Goff. Orchestrating size and shape during morphogenesis. *Nature*, 450(7167):189–92, 2007.

[97] E. H. Lee. Elastic-plastic deformation at finite strains. *Journal of Applied Mechanics*, 36(1), 1969.

[98] J. Lewis. Autoinhibition with transcriptional delay: a simple mechanism for the zebrafish somitogenesis oscillator. *Curr Biol*, 13(16):1398–408, 2003.

[99] Z. Li, S. Liu, and Q. Yang. Incoherent inputs enhance the robustness of biological oscillators. *Cell Syst*, 5(1):72–81 e4, 2017.

[100] J. Lin, J. Chew, U. Chockanathan, and M. J. Rust. Mixtures of opposing phosphorylations within hexamers precisely time feedback in the cyanobacterial circadian clock. *Proc Natl Acad Sci U S A*, 111(37):E3937–45, 2014.

[101] J. C. Locke, L. Kozma-Bognar, P. D. Gould, B. Feher, E. Kevei, F. Nagy, M. S. Turner, A. Hall, and A. J. Millar. Experimental validation of a predicted feedback loop in the multi-oscillator clock of arabidopsis thaliana. *Mol Syst Biol*, 2:59, 2006.

[102] J. C. Locke, A. J. Millar, and M. S. Turner. Modelling genetic networks with noisy and varied experimental data: the circadian clock in arabidopsis thaliana. *J Theor Biol*, 234(3):383–93, 2005.

[103] J. C. Locke, M. M. Southern, L. Kozma-Bognar, V. Hibberd, P. E. Brown, M. S. Turner, and A. J. Millar. Extension of a genetic network model by iterative experimentation and mathematical analysis. *Mol Syst Biol*, 1:2005 0013, 2005.

[104] M. Lu, M. K. Jolly, H. Levine, J. N. Onuchic, and E. Ben-Jacob. Microrna-based regulation of epithelial-hybrid-mesenchymal fate determination. *Proc Natl Acad Sci U S A*, 110(45):18144–9, 2013.

[105] S. R. Mackey and S. S. Golden. Winding up the cyanobacterial circadian clock. *Trends Microbiol*, 15(9):381–8, 2007.

[106] Shannon R. Mackey, Jayna L. Ditty, Gil Zeidner, You Chen, and Susan S. Golden. *Mechanisms for Entraining the Cyanobacterial Circadian Clock System with the Environment*, pages 141–156. Springer Berlin Heidelberg, Berlin, Heidelberg, 2009.

[107] Y. Mao, A. L. Tournier, A. Hoppe, L. Kester, B. J. Thompson, and N. Tapon. Differential proliferation rates generate patterns of mechanical tension that orient tissue growth. *EMBO J*, 32(21):2790–803, 2013.

[108] E. Marcinkevicius and J. A. Zallen. Regulation of cytoskeletal organization and junctional remodeling by the atypical cadherin fat. *Development*, 140(2):433–43, 2013.

[109] M. Marder and N. Papanicolaou. Geometry and elasticity of strips and flowers. *Journal of Statistical Physics*, 125(5-6):1065–1092, 2006.

[110] J. S. Markson and E. K. O'Shea. The molecular clockwork of a protein-based circadian oscillator. *FEBS Lett*, 583(24):3938–47, 2009.

[111] W. Mather, M. R. Bennett, J. Hasty, and L. S. Tsimring. Delay-induced degrade-and-fire oscillations in small genetic circuits. *Phys Rev Lett*, 102(6):068105, 2009.

[112] A. Menzel and E. Kuhl. Frontiers in growth and remodeling. *Mech Res Commun*, 42:1–14, 2012.

[113] L. Michaelis and M. L. Menten. The kenetics of the inversion effect. *Biochemische Zeitschrift*, 49:333–369, 1913.

[114] J. H. Michell. On the direct determination of stress in an elastic solid, with application to the theory of plates. *Proceedings of the London Mathematical Society*, s1-31(1):100–124, 1899.

[115] M. Milan, S. Campuzano, and A. Garcia-Bellido. Cell cycling and patterned cell proliferation in the wing primordium of drosophila. *Proc Natl Acad Sci U S A*, 93(2):640–5, 1996.

[116] M. Milan, S. Campuzano, and A. Garcia-Bellido. Developmental parameters of cell death in the wing disc of drosophila. *Proc Natl Acad Sci U S A*, 94(11):5691–6, 1997.

[117] A. J. Millar. Input signals to the plant circadian clock. *J Exp Bot*, 55(395):277–83, 2004.

[118] C. J. Miller and L. A. Davidson. The interplay between cell signalling and mechanics in developmental processes. *Nat Rev Genet*, 14(10):733–44, 2013.

[119] H. Min, Y. Liu, C. H. Johnson, and S. S. Golden. Phase determination of circadian gene expression in synechococcus elongatus pcc 7942. *J Biol Rhythms*, 19(2):103–12, 2004.

[120] V. Mirabet, P. Das, A. Boudaoud, and O. Hamant. The role of mechanical forces in plant morphogenesis. *Annu Rev Plant Biol*, 62:365–85, 2011.

[121] N. A. M. Monk. Oscillatory expression of hes1, p53, and nf-kappa b driven by transcriptional time delays. *Current Biology*, 13(16):1409–1413, 2003.

[122] T. Mori and C. H. Johnson. Circadian programming in cyanobacteria. *Semin Cell Dev Biol*, 12(4):271–8, 2001.

[123] T. Mori, H. McHaourab, and C. H. Johnson. Circadian clocks: Unexpected biochemical cogs. *Curr Biol*, 25(19):R842–4, 2015.

[124] T. Mori, D. R. Williams, M. O. Byrne, X. Qin, M. Egli, H. S. McHaourab, P. L. Stewart, and C. H. Johnson. Elucidating the ticking of an in vitro circadian clockwork. *PLoS Biol*, 5(4):e93, 2007.

[125] Peer Mumcu. *Self-organized Growth in Developing Epithelia*. Thesis, 2011.

[126] R. Murakami, R. Mutoh, R. Iwase, Y. Furukawa, K. Imada, K. Onai, M. Morishita, S. Yasui, K. Ishii, J. O. Valencia Swain, T. Uzumaki, K. Namba, and M. Ishiura. The roles of the dimeric and tetrameric structures of the clock protein kaib in the generation of circadian oscillations in cyanobacteria. *J Biol Chem*, 287(35):29506–15, 2012.

[127] T. Nagai, T. P. Terada, and M. Sasai. Synchronization of circadian oscillation of phosphorylation level of kaic in vitro. *Biophys J*, 98(11):2469–77, 2010.

[128] Y. Nakahira, M. Katayama, H. Miyashita, S. Kutsuna, H. Iwasaki, T. Oyama, and T. Kondo. Global gene repression by kaic as a master process of prokaryotic circadian system. *Proc Natl Acad Sci U S A*, 101(3):881–5, 2004.

[129] M. Nakajima, K. Imai, H. Ito, T. Nishiwaki, Y. Murayama, H. Iwasaki, T. Oyama, and T. Kondo. Reconstitution of circadian oscillation of cyanobacterial kaic phosphorylation in vitro. *Science*, 308(5720):414–5, 2005.

[130] Denise Nellen, Richard Burke, Gary Struhl, and Konrad Basler. Direct and long-range action of a dpp morphogen gradient. *Cell*, 85(3):357–368, 1996.

[131] U. Nienhaus, T. Aegerter-Wilmsen, and C. M. Aegerter. In-vivo imaging of the drosophila wing imaginal disc over time: novel insights on growth and boundary formation. *PLoS One*, 7(10):e47594, 2012.

[132] T. Nishiwaki, Y. Satomi, Y. Kitayama, K. Terauchi, R. Kiyohara, T. Takao, and T. Kondo. A sequential program of dual phosphorylation of kaic as a basis for circadian rhythm in cyanobacteria. *EMBO J*, 26(17):4029–37, 2007.

[133] T. Nishiwaki, Y. Satomi, M. Nakajima, C. Lee, R. Kiyohara, H. Kageyama, Y. Kitayama, M. Temamoto, A. Yamaguchi, A. Hijikata, M. Go, H. Iwasaki, T. Takao, and T. Kondo. Role of kaic phosphorylation in the circadian clock system of synechococcus elongatus pcc 7942. *Proc Natl Acad Sci U S A*, 101(38):13927–32, 2004.

[134] B. Novak and J. J. Tyson. Numerical-analysis of a comprehensive model of m-phase control in xenopus-oocyte extracts and intact embryos. *Journal of Cell Science*, 106:1153–1168, 1993.

[135] B. Novak and J. J. Tyson. Design principles of biochemical oscillators. *Nat Rev Mol Cell Biol*, 9(12):981–91, 2008.

[136] Y. Ouyang, C. R. Andersson, T. Kondo, S. S. Golden, and C. H. Johnson. Resonating circadian clocks enhance fitness in cyanobacteria. *Proc Natl Acad Sci U S A*, 95(15):8660–4, 1998.

[137] J. Paijmans, D. K. Lubensky, and P. R. Ten Wolde. Period robustness and entrainability of the kai system to changing nucleotide concentrations. *Biophys J*, 113(1):157–173, 2017.

[138] J. Paijmans, D. K. Lubensky, and P. R. Ten Wolde. A thermodynamically consistent model of the post-translational kai circadian clock. *PLoS Comput Biol*, 13(3):e1005415, 2017.

[139] Y. Pan, I. Heemskerk, C. Ibar, B. I. Shraiman, and K. D. Irvine. Differential growth triggers mechanical feedback that elevates hippo signaling. *Proc Natl Acad Sci U S A*, 2016.

[140] B. F. Pando and A. van Oudenaarden. Coupling cellular oscillators–circadian and cell division cycles in cyanobacteria. *Curr Opin Genet Dev*, 20(6):613–8, 2010.

[141] N. F. Parker and A. W. Shingleton. The coordination of growth among drosophila organs in response to localized growth-perturbation. *Dev Biol*, 357(2):318–25, 2011.

[142] R. Pattanayek, J. Wang, T. Mori, Y. Xu, C. H. Johnson, and M. Egli. Visualizing a circadian clock protein: crystal structure of kaic and functional insights. *Mol Cell*, 15(3):375–88, 2004.

[143] R. Pattanayek, D. R. Williams, S. Pattanayek, T. Mori, C. H. Johnson, P. L. Stewart, and M. Egli. Structural model of the circadian clock kaib-kaic complex and mechanism for modulation of kaic phosphorylation. *EMBO J*, 27(12):1767–78, 2008.

[144] R. Pattanayek, D. R. Williams, S. Pattanayek, Y. Xu, T. Mori, C. H. Johnson, P. L. Stewart, and M. Egli. Analysis of kaia-kaic protein interactions in the cyano-bacterial circadian clock using hybrid structural methods. *EMBO J*, 25(9):2017–28, 2006.

[145] R. Pattanayek, D. R. Williams, G. Rossi, S. Weigand, T. Mori, C. H. Johnson, P. L. Stewart, and M. Egli. Combined saxs/em based models of the s. elongatus post-translational circadian oscillator and its interactions with the output his-kinase sasa. *PLoS One*, 6(8):e23697, 2011.

[146] C. Phong, J. S. Markson, C. M. Wilhoite, and M. J. Rust. Robust and tunable circadian rhythms from differentially sensitive catalytic domains. *Proc Natl Acad Sci U S A*, 110(3):1124–9, 2013.

[147] J. R. Pomerening, S. Y. Kim, and J. E. Ferrell. Systems-level dissection of the cell-cycle oscillator: Bypassing positive feedback produces damped oscillations. *Cell*, 122(4):565–578, 2005.

[148] A. Puliafito, L. Hufnagel, P. Neveu, S. Streichan, A. Sigal, D. K. Fygenson, and B. I. Shraiman. Collective and single cell behavior in epithelial contact inhibition. *Proc Natl Acad Sci U S A*, 109(3):739–44, 2012.

[149] X. Qin, M. Byrne, T. Mori, P. Zou, D. R. Williams, H. McHaourab, and C. H. Johnson. Intermolecular associations determine the dynamics of the circadian kaiabc oscillator. *Proc Natl Acad Sci U S A*, 107(33):14805–10, 2010.

[150] X. Qin, M. Byrne, Y. Xu, T. Mori, and C. H. Johnson. Coupling of a core post-translational pacemaker to a slave transcription/translation feedback loop in a circadian system. *PLoS Biol*, 8(6):e1000394, 2010.

[151] D. A. Rand, B. V. Shulgin, D. Salazar, and A. J. Millar. Design principles underlying circadian clocks. *J R Soc Interface*, 1(1):119–30, 2004.

[152] J. Ranft, M. Basan, J. Elgeti, J. F. Joanny, J. Prost, and F. Julicher. Fluidization of tissues by cell division and apoptosis. *Proc Natl Acad Sci U S A*, 107(49):20863–8, 2010.

[153] M. Rauzi, P. F. Lenne, and T. Lecuit. Planar polarized actomyosin contractile flows control epithelial junction remodelling. *Nature*, 468(7327):1110–4, 2010.

[154] M. Rauzi, P. Verant, T. Lecuit, and P. F. Lenne. Nature and anisotropy of cortical forces orienting drosophila tissue morphogenesis. *Nat Cell Biol*, 10(12):1401–10, 2008.

[155] Edward K. Rodriguez, Anne Hoger, and Andrew D. McCulloch. Stress-dependent finite growth in soft elastic tissues. *Journal of Biomechanics*, 27(4):455–467, 1994.

[156] D. Rogulja and K. D. Irvine. Regulation of cell proliferation by a morphogen gradient. *Cell*, 123(3):449–61, 2005.

[157] M. J. Rust, S. S. Golden, and E. K. O'Shea. Light-driven changes in energy metabolism directly entrain the cyanobacterial circadian oscillator. *Science*, 331(6014):220–3, 2011.

[158] M. J. Rust, J. S. Markson, W. S. Lane, D. S. Fisher, and E. K. O'Shea. Ordered phosphorylation governs oscillation of a three-protein circadian clock. *Science*, 318(5851):809–12, 2007.

[159] P. Saez, E. Pena, M. A. Martinez, and E. Kuhl. Computational modeling of hypertensive growth in the human carotid artery. *Comput Mech*, 53(6):1183–1196, 2014.

[160] G. Salbreux, L. K. Barthel, P. A. Raymond, and D. K. Lubensky. Coupling mechanical deformations and planar cell polarity to create regular patterns in the zebrafish retina. *PLoS Comput Biol*, 8(8):e1002618, 2012.

[161] L. J. Saucedo and B. A. Edgar. Filling out the hippo pathway. *Nat Rev Mol Cell Biol*, 8(8):613–21, 2007.

[162] T. Schluck, U. Nienhaus, T. Aegerter-Wilmsen, and C. M. Aegerter. Mechanical control of organ size in the development of the drosophila wing disc. *PLoS One*, 8(10):e76171, 2013.

[163] Erwin Schrdinger. *What is life? The physical aspect of the living cell*. The University press, Cambridge [Eng.], 1944.

[164] Ulrich S. Schwarz and Samuel A. Safran. Physics of adherent cells. *Reviews of Modern Physics*, 85(3):1327–1381, 2013.

[165] Eran Sharon and Efi Efrati. The mechanics of non-euclidean plates. *Soft Matter*, 6(22):5693, 2010.

[166] B. I. Shraiman. Mechanical feedback as a possible regulator of tissue growth. *Proc Natl Acad Sci U S A*, 102(9):3318–23, 2005.

[167] S. J. Silber. Growth of baby kidneys transplanted into adults. *Archives of Surgery*, 111(1):75–77, 1976.

[168] R. P. Simone and S. DiNardo. Actomyosin contractility and discs large contribute to junctional conversion in guiding cell alignment within the drosophila embryonic epithelium. *Development*, 137(8):1385–94, 2010.

[169] R. Skalak, G. Dasgupta, M. Moss, E. Otten, P. Dullumeijer, and H. Vilmann. Analytical description of growth. *J Theor Biol*, 94(3):555–77, 1982.

[170] Richard Skalak. Growth as a finite displacement field. Proceedings of the IUTAM Symposium on Finite Elasticity, pages 347–355. Springer Netherlands.

[171] R. M. Smith and S. B. Williams. Circadian rhythms in gene transcription imparted by chromosome compaction in the cyanobacterium synechococcus elongatus. *Proc Natl Acad Sci U S A*, 103(22):8564–9, 2006.

[172] D. B. Staple, R. Farhadifar, J. C. Roper, B. Aigouy, S. Eaton, and F. Julicher. Mechanics and remodelling of cell packings in epithelia. *Eur Phys J E Soft Matter*, 33(2):117–27, 2010.

[173] Steven H. Strogatz. *Nonlinear dynamics and chaos : with applications to physics, biology, chemistry, and engineering*. Westview Press, a member of the Perseus Books Group, Boulder, CO, second edition. edition, 2015.

[174] A. A. Teleman and S. M. Cohen. Dpp gradient formation in the drosophila wing imaginal disc. *Cell*, 103(6):971–80, 2000.

[175] K. Terauchi, Y. Kitayama, T. Nishiwaki, K. Miwa, Y. Murayama, T. Oyama, and T. Kondo. Atpase activity of kaic determines the basic timing for circadian clock of cyanobacteria. *Proc Natl Acad Sci U S A*, 104(41):16377–81, 2007.

[176] D'Arcy Wentworth Thompson and Lancelot Law Whyte. *On growth and form*. The University Press, Cambridge Eng., a new edition, 1942.

[177] R. Tseng, Y. G. Chang, I. Bravo, R. Latham, A. Chaudhary, N. W. Kuo, and A. Liwang. Cooperative kaia-kaib-kaic interactions affect kaib/sasa competition in the circadian clock of cyanobacteria. *J Mol Biol*, 426(2):389–402, 2014.

[178] R. Tseng, N. F. Goularte, A. Chavan, J. Luu, S. E. Cohen, Y. G. Chang, J. Heisler, S. Li, A. K. Michael, S. Tripathi, S. S. Golden, A. LiWang, and C. L. Partch. Structural basis of the day-night transition in a bacterial circadian clock. *Science*, 355(6330):1174–1180, 2017.

[179] A. M. Turing. The chemical basis of morphogenesis. *Philosophical Transactions of the Royal Society of London Series B-Biological Sciences*, 237(641):37–72, 1952.

[180] V. C. Twitty and J. L. Schwind. The growth of eyes and limbs transplanted heteroplastically between two species of amblystoma. *Journal of Experimental Zoology*, 59(1):61–86, 1931.

[181] J. J. Tyson, K. C. Chen, and B. Novak. Sniffers, buzzers, toggles and blinkers: dynamics of regulatory and signaling pathways in the cell. *Curr Opin Cell Biol*, 15(2):221–31, 2003.

[182] J. J. Tyson and B. Novak. Functional motifs in biochemical reaction networks. *Annu Rev Phys Chem*, 61:219–40, 2010.

[183] H. R. Ueda, M. Hagiwara, and H. Kitano. Robust oscillations within the interlocked feedback model of drosophila circadian rhythm. *J Theor Biol*, 210(4):401–6, 2001.

[184] M. Uyttewaal, A. Burian, K. Alim, B. Landrein, D. Borowska-Wykret, A. Dedieu, A. Peaucelle, M. Ludynia, J. Traas, A. Boudaoud, D. Kwiatkowska, and O. Hamant. Mechanical stress acts via katanin to amplify differences in growth rate between adjacent cells in arabidopsis. *Cell*, 149(2):439–51, 2012.

[185] Ioannis Vakonakis and Andy LiWang. *NMR Studies of a Timekeeping System*, pages 103–120. Springer Berlin Heidelberg, Berlin, Heidelberg, 2009.

[186] J. S. van Zon, D. K. Lubensky, P. R. Altena, and P. R. ten Wolde. An allosteric model of circadian kaic phosphorylation. *Proc Natl Acad Sci U S A*, 104(18):7420–5, 2007.

[187] A. Vichas and J. A. Zallen. Translating cell polarity into tissue elongation. *Semin Cell Dev Biol*, 22(8):858–64, 2011.

[188] J. Vollmer, P. Fried, D. Aguilar-Hidalgo, M. Sanchez-Aragon, A. Iannini, F. Casares, and D. Iber. Growth control in the drosophila eye disc by the cytokine unpaired. *Development*, 144(5):837–843, 2017.

[189] J. Vollmer and D. Iber. An unbiased analysis of candidate mechanisms for the regulation of drosophila wing disc growth. *Sci Rep*, 6:39228, 2016.

[190] V. Volterra. Fluctuations in the abundance of a species considered mathematically. *Nature*, 118:558–560, 1926.

[191] S. B. Williams, I. Vakonakis, S. S. Golden, and A. C. LiWang. Structure and function from the circadian clock protein kaia of synechococcus elongatus: a potential clock input mechanism. *Proc Natl Acad Sci U S A*, 99(24):15357–62, 2002.

[192] Arthur T. Winfree. *The geometry of biological time*. Interdisciplinary applied mathematics. Springer, New York, 2nd edition, 2001.

[193] L. Wolpert. Positional information and the spatial pattern of cellular differentiation. *J Theor Biol*, 25(1):1–47, 1969.

[194] Y. Xu, T. Mori, and C. H. Johnson. Cyanobacterial circadian clockwork: roles of kaia, kaib and the kaibc promoter in regulating kaic. *EMBO J*, 22(9):2117–26, 2003.

[195] C. C. Yang, H. K. Graves, I. M. Moya, C. Tao, F. Hamaratoglu, A. B. Gladden, and G. Halder. Differential regulation of the hippo pathway by adherens junctions and apical-basal cell polarity modules. *Proc Natl Acad Sci U S A*, 112(6):1785–90, 2015.

[196] Q. Yang, B. F. Pando, G. Dong, S. S. Golden, and A. van Oudenaarden. Circadian gating of the cell cycle revealed in single cyanobacterial cells. *Science*, 327(5972):1522–6, 2010.

[197] Arash Yavari, Jerrold E. Marsden, and Michael Ortiz. On spatial and material covariant balance laws in elasticity. *Journal of Mathematical Physics*, 47(4):042903, 2006.

[198] S. Ye, I. Vakonakis, T. R. Ioerger, A. C. LiWang, and J. C. Sacchettini. Crystal structure of circadian clock protein kaia from synechococcus elongatus. *J Biol Chem*, 279(19):20511–8, 2004.

[199] T. M. Yi, Y. Huang, M. I. Simon, and J. Doyle. Robust perfect adaptation in bacterial chemotaxis through integral feedback control. *Proc Natl Acad Sci U S A*, 97(9):4649–53, 2000.

[200] T. Yoshida, Y. Murayama, H. Ito, H. Kageyama, and T. Kondo. Nonparametric entrainment of the in vitro circadian phosphorylation rhythm of cyanobacterial kaic by temperature cycle. *Proc Natl Acad Sci U S A*, 106(5):1648–53, 2009.

[201] J. A. Zallen and J. T. Blankenship. Multicellular dynamics during epithelial elongation. *Semin Cell Dev Biol*, 19(3):263–70, 2008.

[202] M. Zordan, R. Costa, G. Macino, C. Fukuhara, and G. Tosini. Circadian clocks: What makes them tick? *Chronobiology International*, 17(4):433–451, 2000.

[203] D. Zwicker, D. K. Lubensky, and P. R. ten Wolde. Robust circadian clocks from coupled protein-modification and transcription-translation cycles. *Proc Natl Acad Sci U S A*, 107(52):22540–5, 2010.